Analysis of Blast Mitigation Strategies Exploiting Fluid-Structure Interaction

by

Nayden Kambouchev
S.B., Massachusetts Institute of Technology (2003)
S.M., Massachusetts Institute of Technology (2005)

Submitted to the Department of Aeronautics and Astronautics
in partial fulfillment of the requirements for the degree of
Doctor of Philosophy in Aeronautics and Astronautics
at the
MASSACHUSETTS INSTITUTE OF TECHNOLOGY
September 2007

Author .....
Department of Aeronautics and Astronautics
June 11, 2007

Certified by .....
Raúl Radovitzky
Associate Professor of Aeronautics and Astronautics
Thesis Supervisor

Certified by .....
Mary Boyce
Gail E. Kendall Professor of Mechanical Engineering

Certified by .....
John Hutchinson
Professor of Engineering & Applied Sciences
Harvard University

Certified by .....
Gareth McKinley
Professor of Mechanical Engineering

Accepted by .....
Jaime Peraire
Chairman, Department Committee on Graduate Students

Analysis of Blast Mitigation Strategies Exploiting Fluid-Structure Interaction

by

Nayden Kambouchev

Submitted to the Department of Aeronautics and Astronautics
on June 11, 2007, in partial fulfillment of the
requirements for the degree of
Doctor of Philosophy in Aeronautics and Astronautics

Abstract

Blast attacks have become the most pervasive threat in both civil and military contexts. However, there is currently a limited understanding of the mechanisms of loading, damage and failure of structures, and injury to humans produced by blast. This thesis seeks to advance our current understanding of the mechanisms of blast loading on structures. Towards this end, a comprehensive analytical and numerical study of basic problems in the interaction of blast waves with structures is conducted. The analysis is of interest in the conception of blast mitigation strategies and in the design and optimization of protection systems with improved performance against blast.

The approach builds on a classic solution by G. I. Taylor on the interaction of acoustic blast waves with free-standing plates (In G. K. Batchelor, editor, *The Scientific Papers of Sir Geoffrey Ingram Taylor*, vol. III, p.287-303, Cambridge University Press, 1963). Taylor's analysis demonstrates that the coupled fluid-structure interaction effect can be exploited for the purpose of reducing the impulse transmitted from the blast to the structure. This basic result is not applicable to the case of air blasts due to non-linear compressibility effects.

In this thesis, a number of extensions of Taylor's theory is proposed. The case of air blast waves interacting with free-standing plates of variable mass is given special attention. The limiting cases of extremely heavy and extremely light plates are explored analytically for arbitrary blast intensities, from where it is concluded that a modified non-dimensional parameter representing the mass of compressed fluid relative to the mass of the plate governs the fluid-structure interaction. The intermediate asymptotic regimes are studied using a numerical method based on a Lagrangian formulation of the Euler equations of compressible flow and conventional shock-capturing techniques. Based on the analytical and numerical results, approximate formulae for the transmitted impulse describing the entire range of relevant conditions are proposed. The main conclusion of the theory is that non-linear fluid compressibility further enhances the beneficial effects of fluid-structure interaction in reducing the impulse transmitted to the structure. More specifically, it is found that impulse re-

ductions due to fluid-structure interaction are more significant than in the acoustic limit when compared to those obtained ignoring fluid-structure interaction effects.

In addition, a number of acoustic results for uniform shocks, viscoelastic supports, two fluid media, impulsively deployed and pressure actuated plates are proposed which provide the basis for evaluation of the benefits of the fluid-structure interaction in a wide variety of settings. The governing non-dimensional parameters in each specific context are determined and exact solutions to the fluid-structure interaction problem are provided. The results for the actively deployed plates reveal that significant cancellation of the blast impulse can be achieved thus suggesting a plausible blast mitigation strategy.

Thesis Supervisor and Committee Chair: Raúl Radovitzky
Associate Professor of Aeronautics and Astronautics
Thesis Supervisor

Committee Member: Mary Boyce
Gail E. Kendall Professor of Mechanical Engineering

Committee Member: John Hutchinson
Professor of Engineering & Applied Sciences
Harvard University

Committee Member: Gareth McKinley
Professor of Mechanical Engineering

Acknowledgments

A number of people have contributed help, support and ideas to this work and the author wishes to gratefully acknowledge all of them. First, I wish to thank Prof. John Hutchinson for bringing an important and interesting problem from fluid-structure interaction to my adviser's and my attention. Second, I wish to thank my adviser, Prof. Raul Radovitzky, for the freedom which he gave me to explore different topics and directions before settling on the one covered in this thesis. Prof. Radovitzky's guidance with the research was invaluable, always helping me to find the path when I got lost. It is needless to say that his help with the writing, the presentations and the posters improved my communication skills significantly helping me get across the messages I wanted to deliver. Prof. Radovitzky also provided me with many precious opportunities to participate in a number of conferences, workshops and project reviews which revealed to me the full context of my work and improved my understanding of the research needs in the area of blast protection. Many thanks must go also to the members of my thesis committee, Prof. Mary Boyce and Prof. Gareth McKinley, for their insightful comments and questions which always pushed me a step further than I was prepared to take on my own. The almost endless discussions with Prof. Ludovic Noels helped me not only understand better what I was trying to accomplish, but also realize that sometimes the same result can be obtained through many different paths providing insights into the connections between the various problems considered.

A large number of people from the Department of Aeronautics and Astronautics and MIT in general have helped me during the years to overcome the difficulties and cope with the failures. Amongst those who have provided invaluable advice are Prof. Jaime Peraire, Prof. Karen Willcox, Prof. John Dugundji and Dr. Zisu Zhao. A number of students have also contributed to the success of this work through their friendship and support. The list is long, staring with the people in the "RR Group" – Antoine, Ganesh, Ram and Sudhir – going through the people I shared various offices with – Namiko, Matt, Jay and Corey – and finishing with the students I met through

various activities – Sian, Greg, Damien, Hiro, Suddha, Naresh, Suvrat, Eric, Julie and many many others, whose names will require many pages to be filled.

Last, but not least, I would like to thank the Advanced Scientific Computing Initiative of the Department of Energy and the Institute of Soldier Nanotechnology established by the research branch of the United States Army for the financial support during the years – without it this work would have not been possible.

Contents

List of Figures

List of Tables

Chapter 1

Introduction

This thesis is concerned with the development of models of blast effects on structures. This chapter describes the relevance of the research conducted to society, summarizes previous work in the understanding of the fundamentals of blast mechanics and blast mitigations strategies and outlines the scientific contributions of the thesis.

1.1 Effects of Explosions on Structures and Humans

The significant recent increase in terrorist activity and the military involvement in prolonged conflicts has revealed the vulnerability of humans and structures to explosions and blast waves. Buildings and public transportation systems have often offered terrorists the largest potential for human life losses and destruction. The examples of high profile terrorist attacks on buildings include the truck bomb in front of the Alfred E. Murrah Federal Building (Figure 1-1) in Oklahoma City and the fuel truck explosion next to the Khobar Tower (Figure 1-2) in Saudi Arabia. In both attacks many lives were lost and the buildings were damaged beyond repair. The examples of attacks on transportation infrastructure include the simultaneous explosions of four bombs on commuter trains in Madrid, Spain, on March 11, 2004 [103] and the series of small bomb attacks in London during the month of July, 2005 [26]. Several hundred

Figure 1-1: The Alfred E. Murrah Federal Building in Oklahoma City, Oklahoma after the terrorist attack of April 19, 1995 [18].

Figure 1-2: The Khobar Tower in Saudi Arabia after the terrorist attack of June 25, 1996 [74].

Figure 1-3: USS Cole after the terrorist attack of October 29, 2000 in the port of Aden, Yemen [78].

Figure 1-4: RG-31 vehicle after an attack with an improvised explosive device near Camp Taqaddum, Iraq [123].

lives were lost in this tragic events. Despite its better technology, the military has also lost a number of lives and vehicles due to insufficient blast protection capabilities. The examples of attacks on military targets include the small boat explosion against USS Cole (Figure 1-3) and the typical improvised explosion devices (IEDs) attacks from Iraq and Afghanistan (Figure 1-4).

The problem of blast wave caused damage and injury has become ubiquitous with the steep increase of traumatic brain injuries (TBI) observed in Iraq and Afghanistan [40]. TBI is a primary injury [20, 68] occurring on the sub-cellular level which cannot be treated by conventional medical techniques [40]. TBI is usually expressed in the form of concussions, hemorrhages and edemas [115] leading to immediate or gradual deterioration of the neural activity. In addition to the brain, the lung has also shown vulnerability to blast waves with lung contusions leading to contamination of the alveoli with blood [20, 113]. The need for improved personal protection against TBI and lung injuries makes blast injury mechanics an active research topic [21, 114, 115].

In spite of the significant governmental, military and civil resources directed towards reducing the vulnerability of humans and structures to blast waves, it is widely accepted that the effects of blast waves on humans and structures are poorly understood. It is therefore of critical importance to develop theories and models capable of describing these effects qualitatively and quantitatively.

1.2 Explosions and Blast Waves

The effects that are described in the previous section are caused by explosions generated by conventional or nuclear explosives [79, 80], high pressure gases [6] or dust mixtures [9] with their primary effect being the creation of blast waves. In this work we focus on those caused by chemical reactions. A common feature of all explosions is the release of large amounts of chemical, mechanical or nuclear energy in very short time periods on the order of 10^{-6} to 10^{-3} seconds [57]. The fast energy release causes instantaneous increase in the pressure and temperature within the explosive material [106] to values that can reach 100 MPa and 3000 K, respectively, or even higher in

Figure 1-5: Blast wave generated by a 4.8 kiloton explosion [31].

the case of nuclear explosions. The extremely high pressure within the explosion products generates a strong blast wave propagating in the surrounding medium away from the explosion center at supersonic speeds on the order of 2-3 km·s^{-1}. The blast wave contains as much as 95% of the available energy for conventional high-energy explosives. For nuclear explosions, the blast wave contains as little as 50% of the total energy, but the total yield is significantly higher [41]. The rest of the energy is dissipated through thermal radiation, light generation and, in the case of nuclear explosions, various forms of X-rays.

A blast wave generated by a conventional explosive with energy release equivalent to 4.8 kilotons of TNT is shown in Figure 1-5. The front of the blast wave is visible close to the center of the picture due to light diffraction caused by the large differences of the optical properties of the gas in front and behind the wave discontinuity. The diamond shaped patterns close to the ground are shock waves caused by supersonically flying fragments which have overtaken the blast wave [31].

The most important parameter characterizing the blast wave is the peak overpres-

sure p_s which scales with the energy E_0 released during the explosion [7, 11, 12]. The scaling laws for explosions were first derived by Taylor [117]

$$L = C_L(\gamma) \left(\frac{E_0 t^2}{\rho_0} \right)^{\frac{1}{5}} \tag{1.1}$$

$$p_s = C_p(\gamma) \left(\frac{E_0^2 \rho_0^3}{t^6} \right)^{\frac{1}{5}} = \tilde{C}_p(\gamma) \frac{E_0}{L^3}, \tag{1.2}$$

where L is the distance between the explosion center and the blast wave front, ρ_0 is the ambient atmospheric density, γ is the specific heat ratio for air, and C_L, C_p and $\tilde{C}_p$ are constants depending only on the properties of the medium. Von Neumann [126] found the exact similarity solution (available in Appendix A) to the point source explosion problem suggested by expressions (1.1) and (1.2). Since then, a series of exact solutions for strong explosions has been developed [4, 5, 14, 73, 104, 105], e.g. explosions in variable density atmospheres, homothermic (constant temperature) explosions, bursts in atmospheres with steady winds, etc. A general framework for similarity solutions independent of the exact equation of state has been developed by Oppenheim [82]. Similarity solutions have limited validity because they rely on the assumption that the pressure in the quiescent medium is zero, which is a good approximation only for large peak overpressures, $p_s \geq 1$ MPa [117]. Approximations for small peak overpressures have been proposed based on small parameter expansions [100] and the semi-similarity solutions [83]. Numerical investigations of the propagation of blast waves in two and three dimensions have also been performed [14, 15]. Numerical simulations are capable of handling complex equations of state which are not tractable analytically [84, 111, 112], and provide better agreement with experimental measurements than analytical models [39].

If a sensor is placed at a fixed location close to an explosion, an overpressure (the difference between the static pressure and the ambient atmospheric pressure) profile with the features shown in Figure 1-6 will be recorded. The profile is characterized by the peak positive overpressure p_s, the duration of the positive phase t^+, the peak negative overpressure p^- and the duration of the negative phase t^-. Various empir-

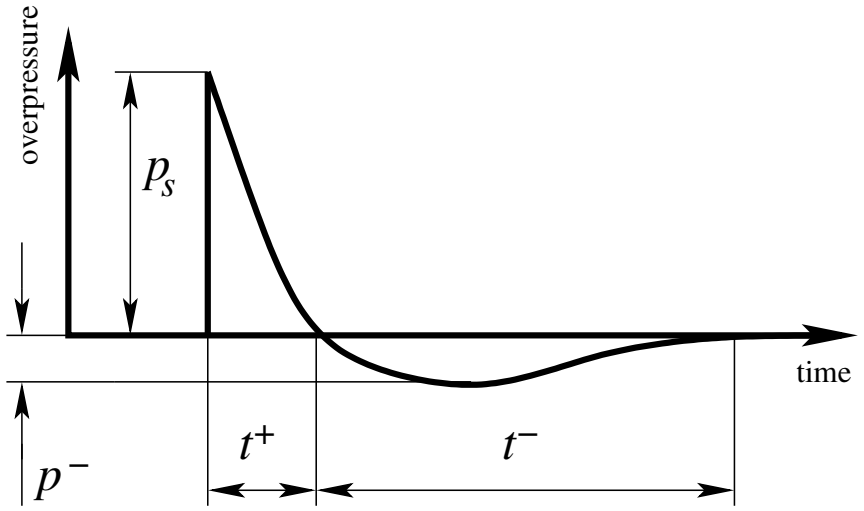

Figure 1-6: A schematic overpressure profile measured by a pressure sensor at a fixed distance from the explosion center.

Table 1.1: TNT equivalent of various explosives [10].

Name	Explosion Energy [MJ·kg^{-1}]	TNT equivalent fraction
TNT	4.187	1.000
PETN	5.904	1.410
Nitroglycerine	6.155	1.470
Compound B	6.239	1.490
Compound C-4	6.699	1.600

ical formulae for the parameters characterizing the blast wave based on analytical, numerical and experimental results have been proposed [15, 32, 43, 106]. Brode [15] has proposed a commonly used formula giving the peak overpressure p_s in terms of the scaled distance $z = r/W^{1/3}$ where r is the distance from the explosion to the point of measurement and W is the TNT equivalent of the explosion:

$$p_s = \begin{cases} \frac{6.7}{z^3} + 1, & 10 \text{ bar} < p_s \\ \frac{0.975}{z} + \frac{1.455}{z^2} + \frac{5.85}{z^3} - 0.019, & 0.1 \text{ bar} \leq p_s \leq 10 \text{ bar} \end{cases} . \tag{1.3}$$

This formula can be used later on to characterize the effects of the blast in terms of native characteristics of the explosive charge. Conversion tables for obtaining the TNT mass equivalent for common explosives are available, e.g. [10]. Table 1.1 shows a few illustrative examples.

Various analytical expressions approximating the pressure profile shown in Figure 1-6 have been proposed [8, 54]. One of the simplest approximations is given by the exponential profile

$$p(t) = p_s e^{-\frac{t}{t_i}}, 0 \leq t \leq \infty \tag{1.4}$$

where the decay time t_i is usually chosen so that the peak overpressure p_s and the impulse of the positive phase

$$I = \int_0^{t_+} p(t)dt \tag{1.5}$$

are the same as the experimental values. Expression (1.4) is convenient basis for theoretical developments, but it neglects the negative phase of the blast. More complex expressions have also been proposed, including the following one due to Brode [8]

$$p(t) = p_s \left(1 - \frac{t}{t^+}\right) \left(ae^{-\alpha\frac{t}{t^+}} + (1-a)e^{-\beta\frac{t}{t^+}}\right), \tag{1.6}$$

which can give excellent fits to experimental data.

Once generated, blast waves propagate undisturbed in a spherically symmetric fashion until they encounter natural or man-made objects setting up complex interactions and reflection patterns. During the World War II G. I. Taylor provided the first comprehensive analysis of fluid-structure interaction [119]. He recognized the beneficial effects of fluid-structure interaction in reducing the impulsive loads produced on structures by blast waves. The basic concept is that the motion of the structure relieves the pressure acting on it, thus reducing the transmitted impulse and, as a consequence, the effects of the blast on the structure. The amount of momentum acquired by the structure will, as a result, depend on its inertia. More precisely, Taylor [119] showed that the interaction between a unidimensional blast wave and a plate is governed, at least in the case of negligible compressibility effects, by a single non-dimensional parameter representing the relative time-scales of the duration of the blast overpressure and of the fluid-structure interaction. Assuming the acoustic limit, Taylor's analysis furnishes the solution of the problem in closed-form including an expression of the relative transmitted impulse in terms of

the fluid-structure interaction parameter, independently of the intensity of the blast. Closed form solutions for blast waves interacting with spherical and cylindrical objects are also available [44, 45]. More complex geometries can be handled numerically [63, 66, 67, 97, 98, 108, 134].

1.3 Blast Mitigation Strategies

The use of explosive devices by terrorists as means for destruction has renewed the interest in improvement of the blast resistance of civil and military structures and vehicles. Significant governmental, military and civil resources have been directed towards reducing the vulnerability of the society to bomb attacks. In addition to operational changes, such as provision of sufficient distance between possible targets and public spaces [24], a variety of technical recommendations for blast hardening have been made [81, 25]. The main technical recommendations are continuity of the structures, redundancy in the load bearing paths, reserve strength in excess of live loads, increased energy absorbing capabilities and increased building component mass [81, 109]. Increased energy absorption is usually accomplished through plastic deformation and design guidelines for buildings relying on concepts such as ductility ratio and maximum support rotation are available [69]. Fragmentation and structural collapse can be prevented by bonding of fiber-reinforced polymers to masonry walls [13], placing layers of aluminum foams on walls [102], steel stud reinforcements [101], profiling of the metal plates used in movable constructions [65] and laminated architectural glazing [131]. The majority of these concepts is based on increasing the energy dissipation capabilities of the structure and its components with most of the attention focused on metal foams [72, 99], foam-like materials such as honeycombs [3], and polymers [13, 125]. Due to dramatic advances in ballistic protection, such as the use of Kevlar fibers, modern personal armor offers an efficient protection against missiles and debris [42], however, it has remained inefficient against the direct effects of blast waves on the human body [22, 68, 113].

Significant contributions to the conception and design of structures with increased

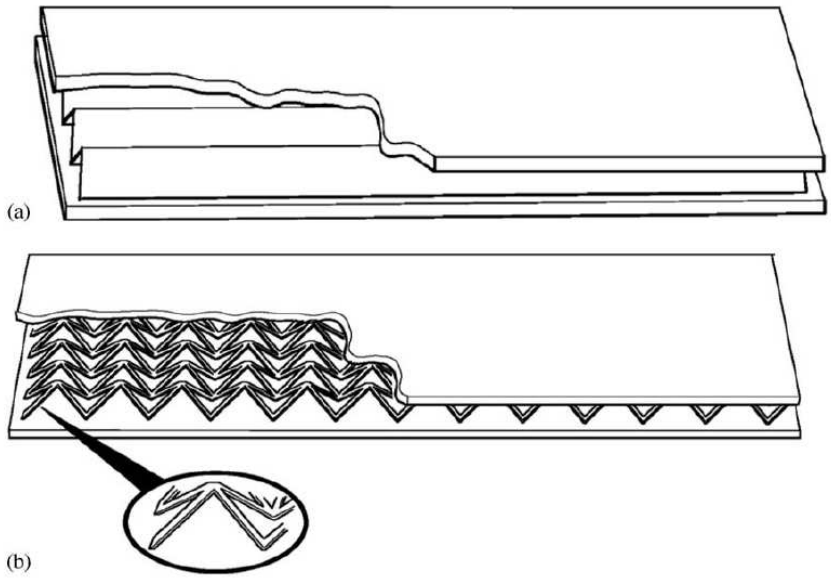

Figure 1-7: Sandwich plates with (a) corrugated and (b) pyramidal cores [94]

blast mitigation performance have recently arisen from the academic environment [37, 46, 49, 50, 64, 71, 96].

Xue and Hutchinson [135] recently proposed a new protection concept utilizing light sandwich constructions. This concept is based on the fluid-structure interaction effect discovered by G. I. Taylor [119]. In an oversimplified form, Taylor's result states that lighter structures acquire less momentum than heavier structures when exposed to the same blast. The reduction in transmitted impulse can be utilized advantageously by the light face sheets of sandwich panels. Examples of two different core topologies are shown in Figure 1-7. The original study by Xue and Hutchinson [135] ignored the fluid-structure interaction effects and concentrated on the structural response of the panels. A subsequent study [136] considered fluid-structure interaction by obtaining the impulse imposed on the plate from Taylor's theory [119] which is valid for unsupported plates in acoustic media.

Xue and Hutchinson [136] propose what in effect decouples the analysis of the problem in two phases: fluid-structure interaction phase and structural response phase. Fleck and Deshpande further split the structural response phase into two stages: core crashing stage and plastic bending and stretching stage:

- **Phase I: Fluid-structure interaction phase.** The main result of the analysis in this phase is a single number: the momentum per unit area transmitted to the structure. The assumption under which the effects of the interaction can be captured by a single number have been discussed at large in [37, 38, 116].

- **Phase II: Core compression stage.** In this phase the total momentum is conserved, but the total energy is reduced due to dissipation in the sandwich core. Typically the densification of the core is not studied in detail, however the plastic shock wave propagation can be modeled [29] and the shock arrest location and time can be identified.

- **Phase III: Bending and stretching phase.** If there is any remaining energy after the sandwich core has completely densified, this energy is dissipated by bending and stretching processes similar to those observed for monolithic plates [37, 48].

The three stage analysis relies on separation of the time scales between the phases. The separation of time scales between the phases has been argued based on results from on finite element simulations [88, 89]. However, experiments have shown that separation of the timescales cannot be always assumed [71, 96]. Indeed four different types of response coupling phases II and III have been identified [70, 122]. The specific response mechanism depends on the loading and the sandwich core thickness and strength which determine the time at which the core densification is completed, the time at which back face deceleration commences and the time at which both faces attain the same velocity. Additionally Tilbrook et al. [122] have shown that sometimes phase coupling enhances the beneficial effects of sandwich plates and sometimes it makes the sandwich panels inferior to monolithic plates. The majority of the analyses mentioned above consider full span blast wave loading of the beams and plates, but the case of localized loadings over central patches has also been considered [90].

Detailed finite element analyses have been conducted providing further insights into the response of sandwich panels to impulsive loading. Deshpande et al. [29] and Rabczuk et al. [91] have shown that the assumption of impulsive load leads to

an underestimation of the impulse transmitted from the blast wave to the structure and an overestimation of the benefits offered by sandwich panels. In [29, 46, 64] the sandwich core resistance during the fluid-structure interaction phase is taken into account by assuming a constant core resistance. Water cavitation is shown to occur in the fluid domain (see Chapter 3) which is accounted for in the models by adding the impulse of the cavitated water layer to the loading of the structure [46]. Rabzcuk et al. [92] considered the case of a sandwich plate core with rheological response.

The modeling effort aimed at improving the understanding of blast effects on monolithic and sandwich structures has been accompanied by experimental studies including fabrication and testing. A variety of core topologies has been considered and tested in laboratory setting under static and dynamic loads [55, 86, 87, 129, 130]. The growing body of monolithic and sandwich plate test results has provided physical evidence of the response mechanisms as well as valuable opportunities for model validation [17, 47, 62, 75, 76, 77, 137]. Due to the difficulties associated with explosion experiments, creative testing approaches have been proposed as surrogates. One such approach involves shooting low density projectiles directly or indirectly onto plates [94]. Typically the projectiles are cut out of metal foam and shot directly at sandwich beams or circular plates with foam, pyramidal, corrugated and honeycomb cores [71, 93, 95, 96]. However the loading produced in this manner differs substantially from characteristic blast load profiles, causing the damage to localize around the impact area [94]. The underwater shock simulator of Deshpande et al. [30] is an example of indirect loading in which the foam projectiles are fired against the piston of a shock tube filled with water.

Most of the experimental studies are accompanied by finite element simulations using the commercial software package ABAQUS, in reasonable agreement with the experimental results. Two modeling approaches for the sandwich cores have been used: a detailed approach which explicitly considers the topology of the core [136] and a homogenized approach which models the core as a continuous solid whose response is equivalent to that of the core [91]. The advantage of the latter technique is that it simplifies the creation of the computational model and reduces the computational

time. However it necessitates the development and calibration of the homogenized model for each core type and may miss important details of the response.

The role played by the structural supports has been discussed by Langdon and Schleyer [58, 59, 60, 61] who have found significant dependence of the blast performance of the plates on the type of boundary conditions. Hutchinson and Xue [46] investigated the failure modes arising in clamped sandwich plates and observed that clamping promotes large strains and shear-off of the face sheets at the supports.

Novel concepts such as filling the core space with polymeric foams [125] or using packaging bubble wraps in water [30] have also been explored. The polymeric foam has been shown to neither enhance nor reduce the structural advantages of the sandwich plates, but it may be of interest for other applications such as acoustic insulation. The bubble wrap led to an extremely large reduction in the deflection of the structure. Another concept that has been proposed exploits the large energy dissipation capabilities of thin wall tubes [120].

To a large extent, blast mitigation strategies exploiting fluid-structure interaction have thus far been conceived based on Taylor's acoustic theory. This is relevant for underwater explosions (see Chapter 3), but not for air blast where non-linear compressibility effects become important. It is therefore of critical importance to develop theories, descriptions and models addressing the additional complexities brought about by blast waves in air.

1.4 Objective

The objective of this thesis is to develop an improved understanding of fluid-structure interaction effects in the air blast loading of structures. The expectation is that the resulting descriptions will provide a rational basis for the conception of improved blast mitigation strategies and the design of material systems with improved blast protection performance.

1.5 Contributions

Towards the end of achieving the objective of this thesis a comprehensive study leading to extensions of Taylor's acoustic theory to the non-linear compressible regime has been conducted. The research consisted of developing a number of semi-analytical and numerical solutions of basic one-dimensional problems in the interaction of blast waves with structures subjected to a variety of supports. As part of the outcome of the research the sought solutions are provided, the governing parameters in the presence of compressibility are elucidated and practical formulae for the impulse transmitted to the structures depending on the characteristics of the blast and the structure are derived. One of the formulae has already been used in the design and optimization of blast resistant sandwich panels [124]. Additionally a number of acoustic problems have been solved.

The specific contributions of this work are:

- Acoustic solutions for the following fluid-structure interaction problems:
  - Alternative derivation of the interaction of an exponential wave with a monolithic plate (Taylor's problem)
  - Interaction of uniform shock waves with monolithic plates
  - Interaction of exponential waves with monolithic plates supported by an acoustic medium
  - Interaction of exponential waves with monolithic plates on viscoelastic supports
  - Interaction of exponential waves with actively deployed monolithic plates for two different deployment mechanisms: one in which the impulse is imparted instantaneously and another one in which the plate is actuated upon by a constant pressure
- A compressible fluid-structure interaction parameter has been identified

- Light and heavy plate asymptotic solutions for blast waves in compressible media interacting with free-standing plates
- Extended (compressible) fluid-structure interaction formulas for the impulse transmitted from a blast wave to a structure in the following cases:
  - Uniform waves impinging on free-standing plates
  - Exponential waves impinging on free-standing plates
  - Exponential waves impinging on actively deployed plates for which the impulse is imparted instantaneously
- Additional contributions
  - A one dimensional numerical code for general analysis of blast-plate interaction
  - A generalized derivation of the von Neumann/Sedov solution for all spatial dimensions
  - A blast code to compute blast wave characteristics

1.6 Structure

This thesis is organized as follows. Chapter 2 presents the general equations of motion of Newtonian fluids: mass, momentum and energy conservation. A closed system of equations can be obtained by adding an equation of state [2]. Two equations of state are considered: air is modeled as an ideal calorically perfect gas with constant specific heats [1] and water is assumed to follow the Tait equation of state [121]. When complemented with appropriate initial and boundary conditions these equations can be solved for the time histories of the density, pressure, velocity and internal energy. Formulas for the discontinuous jumps characterizing shock waves (the Rankine-Hugoniot relationships) are provided. The theoretical jump values are compared to experimental data from the open literature. Section 2.1 ends with a review of the acoustic

approximations of the equations of motion. Section 2.2 describes the reflection of waves from rigid walls and free surfaces.

Chapter 3 contains the exact analytic solutions to a series of acoustic linear wave reflection problems together with the general technique for solving such problems. The solution of each problem is analyzed and conclusions about the effectiveness of the various protection concepts are drawn based on the transmitted momentum, energy and force. The following problems are described in this chapter:

1. Infinitely-long uniform wave impinging on an initially stationary plate
2. Exponential wave impinging on an initially stationary plate
3. Exponential wave impinging on a plate with perfectly-plastic support
4. Exponential wave impinging on a plate with visco-elastic support
5. Exponential wave impinging on a plate supported by another acoustic medium
6. Exponential wave impinging on a plate moving in the opposite direction with the opposite impulse imparted instantaneously
7. Exponential wave impinging on a plate moving in the opposite direction under the action of a constant pressure actuator

The acoustic results are extended into the compressible range in Chapter 4. In the first section, the general approach to the wave reflection problem in compressible media is outlined and the detailed derivation of the light plate asymptotic limit is presented. The second section begins with the uniform wave analysis and continues with the compressible extension of Taylor's fluid-structure interaction formula. Numerical results verifying each extension are given. The relationship between the wave momentum carried by the pressure and the "total" momentum carried by the wave is discussed in Section 4.2.3. The active protection concept is extended to compressible media by building onto the acoustic results from Section 3.4.1. The chapter ends with an analysis of the fluid-structure interaction effects for point source explosions. The scaling approach is similar to the technique of Taylor [117] and Von Neumann [126],

but an exact similarity solution could not be found. Von Neumann's solution with a generalized derivation applicable to planar, cylindrical and spherical explosions is given in Appendix A.

The details of the finite difference numerical scheme [34] are given in Appendix B together with some further information about the numerical calculations.

Chapter 2

Fundamentals of Blast Wave Propagation

The propagation of blast waves is governed by the fundamental physics principles of conservation of mass, momentum and energy. As the viscous stresses in air and water are negligible compared to the pressures developed within the blast waves, viscosity is typically ignored and the inviscid form of the Navier-Stokes equations, the Euler's equations, is used.

2.1 The General Equations of Wave Motion in Fluids

This section presents the conservation of mass, momentum and energy equations followed by the equations of state for air and water, the Rankine-Hoguniot relationships describing the jump conditions across shock waves and the acoustic approximation of blast wave motion.

2.1.1 Conservation Equations

Euler's equations governing fluid motion can be written in various forms, three of which will be used in this work: differential form in Eulerian coordinates, differential

form in Lagrangian coordinates and integral form for a fixed volume.

The Eulerian formulation of the mass, momentum and energy conservation differential equations for an inviscid fluid in a Cartesian coordinate system with coordinates x, y, z and time t is [2]:

$$\left(\frac{\partial}{\partial t} + \mathbf{u}\cdot\nabla\right)\rho = -\rho\nabla\cdot\mathbf{u}, \tag{2.1}$$

$$\left(\frac{\partial}{\partial t} + \mathbf{u}\cdot\nabla\right)\mathbf{u} = -\frac{1}{\rho}\nabla p, \tag{2.2}$$

$$\left(\frac{\partial}{\partial t} + \mathbf{u}\cdot\nabla\right)\left(e + \frac{\mathbf{u}^2}{2}\right) = -\frac{1}{\rho}\nabla\cdot(p\mathbf{u}), \tag{2.3}$$

where ρ is the fluid density, $\mathbf{u}$ is the fluid velocity, p is the fluid pressure, e is the internal energy and the gradient ∇ is defined as

$$\nabla = \left(\frac{\partial}{\partial x}, \frac{\partial}{\partial y}, \frac{\partial}{\partial z}\right). \tag{2.4}$$

An additional equation, an equation of state, is required to solve the system of equations (2.1-2.3). The two most commonly used equations of state for air and water are given in Section 2.1.2.

In Lagrangian coordinates the conservation equations take the form [34]

$$\hat{\rho} = const. \tag{2.5}$$

$$\frac{d}{dt}\hat{\mathbf{u}} = -\frac{1}{\hat{\rho}}\hat{\nabla}\hat{p} \tag{2.6}$$

$$\frac{d}{dt}\left(\hat{e} + \frac{\hat{\mathbf{u}}^2}{2}\right) = -\hat{\nabla}\cdot(\hat{p}\hat{\mathbf{u}}) \tag{2.7}$$

where the flow quantities with hats $\hat{}$ are measured relative to the X, Y and Z axes of an orthogonal Lagrangian coordinate system and the gradient $\hat{\nabla}$ is defined as

$$\hat{\nabla} = \left(\frac{\partial}{\partial X}, \frac{\partial}{\partial Y}, \frac{\partial}{\partial Z}\right). \tag{2.8}$$

The system of equations (2.5-2.7) is rarely used in fluid dynamic simulations because

Lagrangian coordinates do not provide a natural basis for the description of most systems of engineering interest and the large deformations typical for fluids cause severe numerical problems. Nevertheless, in this work we make use of Lagrangian coordinates for the numerical formulation (see Appendix B) because of the ease with which the motion of rigid bodies is modeled in Lagrangian coordinates.

Both sets of differential equations (2.1-2.3) and (2.5-2.7) do not hold across discontinuities which are more conveniently handled through the integral form of the conservation equations [36]

$$\frac{d}{dt}\int_{\mathcal{V}} \rho d\mathcal{V} + \int_{\mathcal{S}} \rho \mathbf{u}\cdot\mathbf{n} d\mathcal{S} = 0, \tag{2.9}$$

$$\frac{d}{dt}\int_{\mathcal{V}} \rho \mathbf{u} d\mathcal{V} + \int_{\mathcal{S}} \rho \mathbf{u}(\mathbf{u}\cdot\mathbf{n}) d\mathcal{S} = -\int_{\mathcal{S}} p\mathbf{n} d\mathcal{S}, \tag{2.10}$$

$$\frac{d}{dt}\int_{\mathcal{V}} \rho\left(e+\frac{\mathbf{u}^2}{2}\right) d\mathcal{V} + \int_{\mathcal{S}} \rho\left(e+\frac{\mathbf{u}^2}{2}\right)\mathbf{u}\cdot\mathbf{n} d\mathcal{S} = -\int_{\mathcal{S}} p\mathbf{u}\cdot\mathbf{n} d\mathcal{S}, \tag{2.11}$$

where the volume $\mathcal{V}$ with surface $\mathcal{S}$ is assumed to be fixed in space and $\mathbf{n}$ is the surface normal.

All governing equations presented above assume that there are no body forces acting on the fluid particles, no heat is generated within the fluid and no heat transfer or radiation is taking place as these are known to be unimportant for the propagation of blast waves [34].

2.1.2 Equations of State

Fluids (and some solids) can be modeled by the Tait equation of state [28, 53]

$$e = e_0 - \frac{p_0 + p_c}{\Gamma_0 \rho_0} + \frac{p + p_c}{\Gamma_0 \rho}, \tag{2.12}$$

where e_0, p_0 and ρ_0 are the energy, pressure and density at a reference state, Γ_0 is a constant and the reference pressure p_c is given by

$$p_c = \rho_0 a_0^2 - (\Gamma_0 + 1)p_0 \tag{2.13}$$

with a_0 being the speed of sound at the reference state. If the internal energy e is taken to depend on the entropy s and the specific volume $v = 1/\rho$ then its partial derivative gives the negative of the pressure,

$$\left.\frac{\partial e}{\partial v}\right|_s = -p. \tag{2.14}$$

This equation defines the isentrope which after substitution from (2.12) can be rewritten as

$$-\frac{\rho}{\Gamma_0}\frac{\partial p}{\partial \rho} + \frac{p + p_c}{\Gamma_0} = -p. \tag{2.15}$$

Upon integration one obtains

$$p = \frac{p_c}{\Gamma_0 + 1}\left[\left(\frac{\rho}{\rho_0}\right)^{\Gamma_0+1} - 1\right] + p_0\left(\frac{\rho}{\rho_0}\right)^{\Gamma_0+1}. \tag{2.16}$$

Sometimes a different version of this equation is referred to as the Tait equation of state [121]

$$p = B\left[\left(\frac{\rho}{\rho_0}\right)^{\Gamma_0+1} - 1\right], \tag{2.17}$$

where B is a constant. The latter version tends to be preferred by most researchers as it is simpler and the correction due to the second factor in (2.16) is small. The equation of state for water used in the numerical simulations is a hybrid between (2.16) and (2.17):

$$p = B\left[\left(\frac{\rho}{\rho_0}\right)^{\Gamma_0+1} - 1\right] + p_0, \tag{2.18}$$

with $B = 3.042 \times 10^8$ Pa, $\Gamma_0 = 6.15$, $\rho_0 = 1.0 \times 10^3$ kg·m^{-3} and $p_0 = 1.014 \times 10^5$ Pa. The corresponding speed of sound at the reference state is $a_0 = 1474.6$ m·s^{-1}.

The equation of state of a polytropic gas is a specific case of Tait's equation when $p_c = 0$ Pa. For a polytropic gas the isentrope (2.16) takes the familiar form

$$\frac{p}{\rho^{\Gamma_0+1}} = \frac{p_0}{\rho_0^{\Gamma_0+1}} \tag{2.19}$$

with the polytropic constant being equal to $\Gamma_0 + 1$.

The most familiar form of the equation of ideal gas is

$$p = \rho R T \tag{2.20}$$

where R is the gas constant and T is the absolute temperature. This equation introduces the temperature and does not provide a connection to the energy, so commonly it is complemented with the assumption that the internal energy is proportional to the temperature

$$e = C_v T \tag{2.21}$$

where the specific heat at constant volume $C_v = \frac{\partial e}{\partial T}\big|_v$ is assumed to be constant. A gas that satisfies equation (2.20) is referred to as thermally perfect, while a gas that satisfies (2.21) is referred to as calorically perfect [35]. After elimination of the temperature the relationship between the pressure, density and energy becomes

$$e - \frac{1}{R/C_v}\frac{p}{\rho} = 0 \tag{2.22}$$

which is clearly equivalent to (2.12) for $p_c = 0$ Pa, as the energy can be measured from an arbitrary reference level

$$e - \frac{1}{\Gamma_0}\frac{p}{\rho} = e_0 - \frac{1}{\Gamma_0}\frac{p_0}{\rho_0}, \tag{2.23}$$

with $\Gamma_0 = R/C_v = \gamma - 1$. The constants for air are $\gamma = 1.4$ and $R = 287$ J·kg^{-1}·K^{-1}.

Even though real gases follow very closely the thermal equation of state (2.20) at moderate temperatures and pressures, significant deviations can occur at elevated temperatures or at low pressures. For air, these deviations are due to dissociation of the nitrogen N_2 and oxygen O_2 molecules and ionization of the resulting atoms. One way to characterize the deviation form the thermal equation of state is through the compressibility parameter z [27, 54],

$$z = \frac{p}{\rho R T}. \tag{2.24}$$

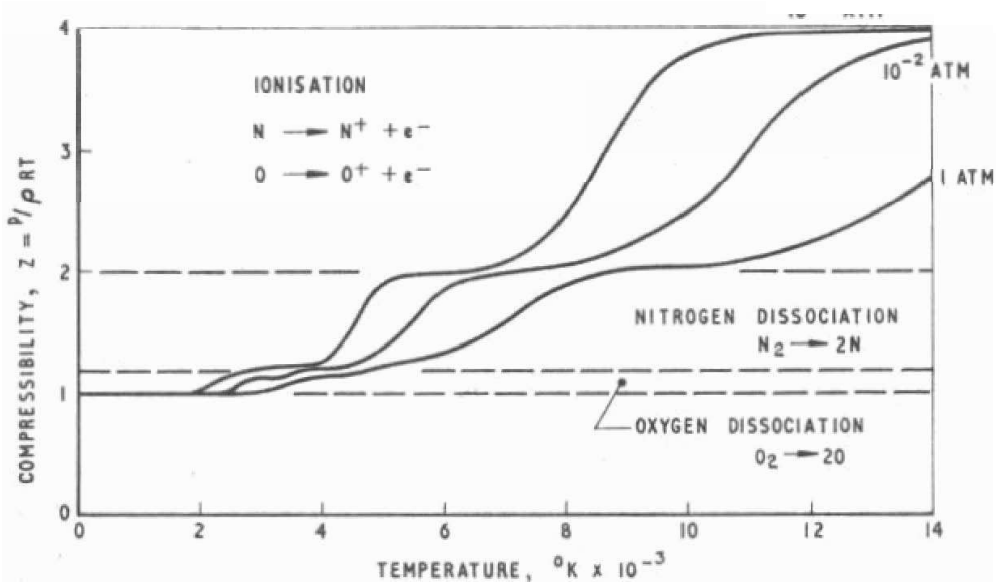

Figure 2-1: Variation of the compressibility factor z, characterizing the deviation from the thermal equation of state (2.20), with the temperature T for various pressures p [27].

A plot of the variation of z with temperature for different values of the pressure p is given in Figure 2-1. Most of the variation in z is due to the variation of the ideal gas constant R in equation (2.24) caused by mole fraction changes due to dissociation and ionization processes.

A calorically perfect gas has a constant specific heats ratio $\gamma = C_p/C_v$ where $C_p = \frac{\partial h}{\partial T}\big|_p$ and $C_v = \frac{\partial e}{\partial T}\big|_v$ with h being the enthalpy per unit mass defined as $h = e + pv$. The variation of γ with temperature is shown in Figure 2-2 indicating that air is not a calorically perfect gas. Most of the variation in the figure is due to excitation of vibrational modes which modifies the values of the specific heats even before the temperature has raised enough for dissociation and ionization to occur [27].

The deviations of air from the ideal gas equation of state are of relatively little interest in blasts due to large differences in the timescales of the blast wave and the dissociation, ionization and vibrational excitation mechanisms. Anderson [1] estimates the dissociation time of oxygen O_2 and nitrogen N_2 molecules to be on the order of hundreds of milliseconds while the total duration of the blast waves is in the

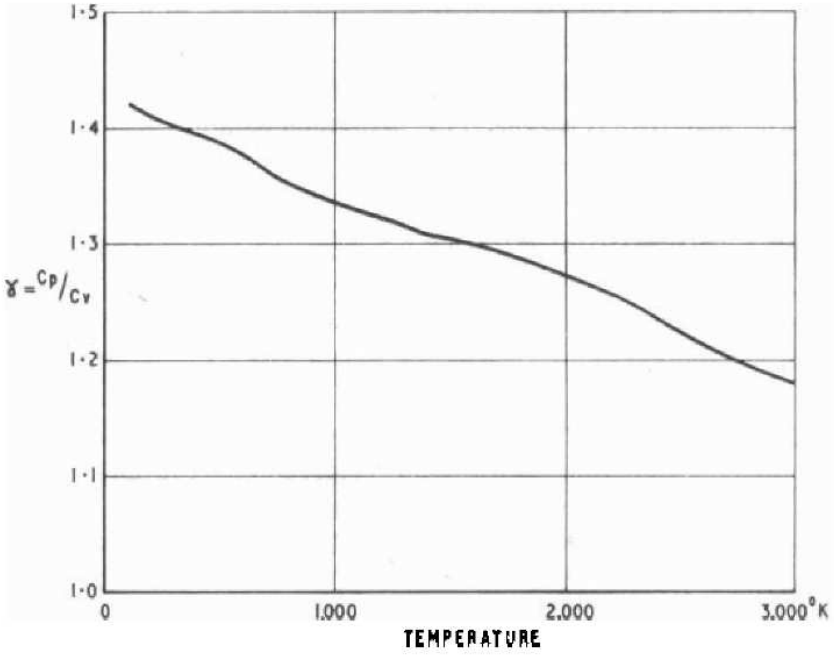

Figure 2-2: Variation of the ratio of specific heats γ of air as a function of the temperature T [27].

order of a few milliseconds. Excitation of vibrational modes takes about a tenth of the time required for molecule dissociation [1], but still remains relatively large compared to the blast decay time. In his assessment of the effects of the first atomic bomb [118], G. I. Taylor argued that even under those extreme conditions the changes in the specific heats are approximately compensated by the radiative heat loss making the value of $\gamma = 1.4$ a very good assumption for blast wave problems.

2.1.3 Shock Jump Relationships

The word "shock" is typically used to describe a traveling wave discontinuity [23] which is the result of inherently non-linear effects causing higher pressure regions of the wave to catch up with the lower pressure regions. Shocks are useful macro-scale abstractions of the very fast atomic scale heat transfer and viscous processes occurring over very thin regions in space which can be ignored for most engineering applications including blast wave propagation. As shown in Figure 1-6 blast waves consist of discontinuous jumps (shocks) in the pressure followed by relatively slow

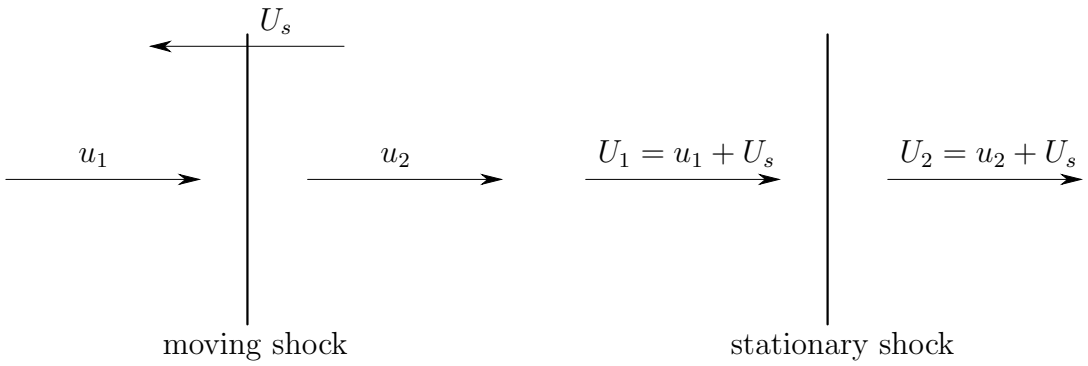

Figure 2-3: Moving and stationary shock waves

decays to ambient conditions and therefore thorough understanding of blast waves propagation requires thorough understanding of the shock front discontinuities which will be characterized in this section.

Consider a shock wave moving with velocity U_s into a uniform stream with particle velocity u_1 as shown in the left part of Figure 2-3 and let the particle velocity behind the shock be u_2. The analysis is simplified greatly if a reference frame moving with U_s is utilized, so that the flow appears steady, as shown in the right part of Figure 2-3. The velocities in front of and behind the shock are $U_1 = u_1 + U_s$ and $U_2 = u_2 + U_s$.

Application of the integral forms of the mass, momentum and energy conservation equations (2.9-2.11) to a control volume which includes the shock wave gives:

$$U_1 \rho_1 = U_2 \rho_2 \tag{2.25}$$

$$p_1 + \rho_1 U_1^2 = p_2 + \rho_2 U_2^2 \tag{2.26}$$

$$e_1 + \frac{p_1}{\rho_1} + \frac{U_1^2}{2} = e_2 + \frac{p_2}{\rho_2} + \frac{U_2^2}{2}, \tag{2.27}$$

where the subscript 1 refers to the flow quantities in front of the shock and subscript 2 refers to the flow quantities behind the shock. For an ideal gas, the equation of state applied to the regions on both sides of the shock (2.22):

$$e_1 = \frac{1}{\gamma - 1} \frac{p_1}{\rho_1} \tag{2.28}$$

$$e_2 = \frac{1}{\gamma - 1} \frac{p_2}{\rho_2}, \tag{2.29}$$

closes the system of equations. The simplest way to solve this system is to introduce the Mach number M,

$$M = \frac{U}{a}, \tag{2.30}$$

where a is the speed of sound in the ideal gas given by

$$a^2 = \left.\frac{\partial p}{\partial \rho}\right|_{s=const} = \gamma RT = \gamma(\gamma-1)e = \gamma\frac{p}{\rho}. \tag{2.31}$$

The energy equation can be rewritten in terms of the Mach number M as

$$a_1^2\left(1+\frac{\gamma-1}{2}M_1^2\right) = a_2^2\left(1+\frac{\gamma-1}{2}M_2^2\right). \tag{2.32}$$

The momentum equation can be divided by the mass conservation equation and rewritten as

$$a_1\frac{1+\gamma M_1^2}{M_1} = a_2\frac{1+\gamma M_2^2}{M_2}. \tag{2.33}$$

The square of equation (2.33), divided by equation (2.32) gives

$$M_2^2 = \frac{1+\frac{\gamma-1}{2}M_1^2}{\gamma M_1^2 - \frac{\gamma-1}{2}}. \tag{2.34}$$

The temperature ratio may be found by substituting the temperature in equation (2.32):

$$\frac{T_2}{T_1} = \frac{e_2}{e_1} = \left(1+\frac{2\gamma}{\gamma+1}(M_1^2-1)\right)\frac{2+(\gamma-1)M_1^2}{(\gamma+1)M_1^2}. \tag{2.35}$$

Conversion of the speed of sound a into the particle velocity U via the Mach number M in equation (2.32) leads to

$$\frac{\rho_2}{\rho_1} = \frac{U_1}{U_2} = \frac{(\gamma+1)M_1^2}{2+(\gamma-1)M_1^2}, \tag{2.36}$$

where mass conservation was used for the first equality. The pressure ratio may be found from equation (2.20)

$$\frac{p_2}{p_1} = 1+\frac{2\gamma}{\gamma+1}(M_1^2-1). \tag{2.37}$$

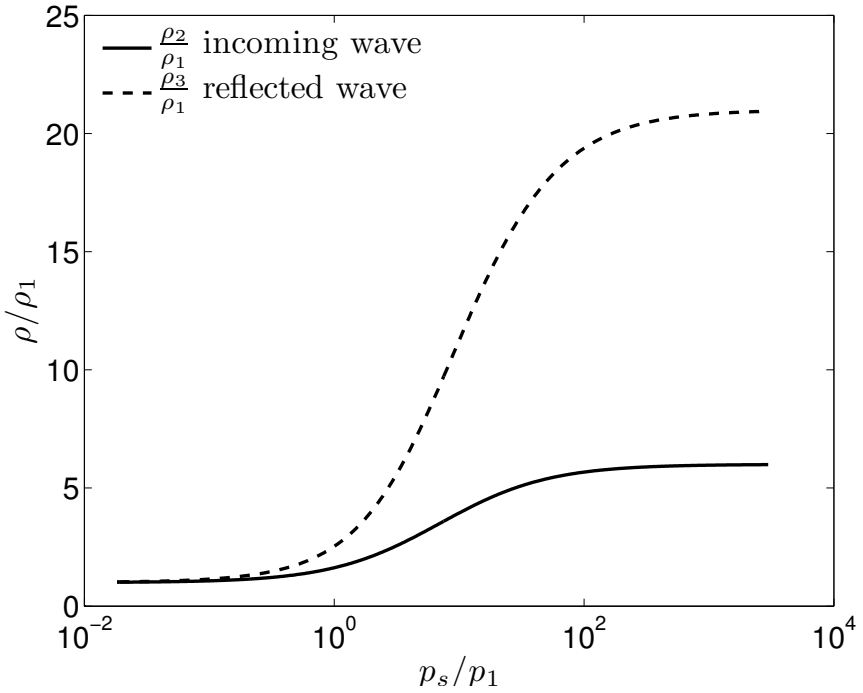

Figure 2-4: Behavior of the density ratios ρ_2/ρ_1 and ρ_3/ρ_1 as a function of the pressure ratio p_s/p_1 of the incoming wave for air ($\gamma = 1.4$).

Equations (2.35-2.37) are the shock jump (or Rankine-Hugoniot) relationships of the flow quantities across a normal shock wave. The derivation presented here loosely followed the derivation given in [2].

For blast waves, it is useful to express the particle velocity, the shock speed and the jump conditions in terms of the blast wave peak overpressure $p_s = p_2 - p_1$ eliminating the Mach number M_1. The speed U_s of the shock wave propagating in still atmosphere, $u_1 = 0$ m·s^{-1}, is

$$U_s = a_1 M_1 = \sqrt{\frac{p_1}{\rho_1}}\sqrt{\frac{p_2}{p_1}\frac{\gamma+1}{2} + \frac{\gamma-1}{2}} = \sqrt{\frac{p_1}{\rho_1}}\sqrt{\frac{\gamma+1}{2}\frac{p_s}{p_1} + \gamma}, \tag{2.38}$$

and the particle velocity u_s behind the shock is

$$u_s = -u_2 = \frac{p_s}{p_1}\sqrt{\frac{p_1}{\rho_1}}\sqrt{\frac{1}{\frac{\gamma+1}{2}\frac{p_s}{p_1} + \gamma}}. \tag{2.39}$$

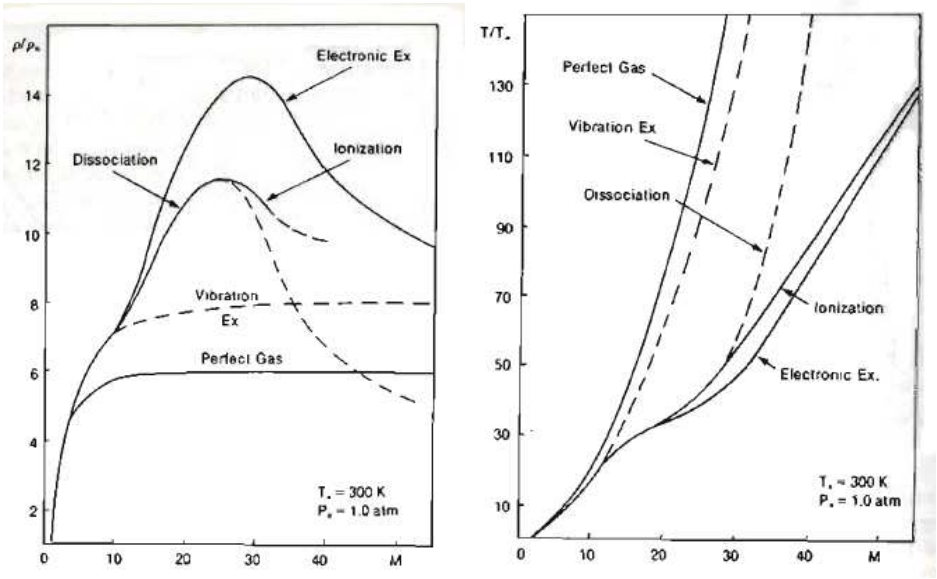

(a) Density (b) Temperature

Figure 2-5: Real gas effects on the density and temperature jump conditions across a shock wave in nitrogen N_2 at temperature $T_1 = 300$ K and pressure $p_1 = 1.014 \times 10^5$ Pa [52].

The jump relationship for the density is obtained from equations (2.36) and (2.37) as

$$\frac{\rho_2}{\rho_1} = \frac{2\gamma + (\gamma+1)\frac{p_s}{p_1}}{2\gamma + (\gamma-1)\frac{p_s}{p_1}}. \tag{2.40}$$

This equation implies that the density ratio across a shock wave traveling in an ideal gas is finite regardless of the shock strength. Figure 2-4 shows the variation of the density ratio ρ_2/ρ_1 for air ($\gamma = 1.4$) as a function of the overpressure p_s. In this case, the limiting density ratio is 6, i.e. $\sup(\rho_2/\rho_1) = 6$. This is another manifestation of the *hypersonic Mach number independence principle* [2] which states that at sufficiently high Mach numbers certain aspects of the flow become independent of the Mach number M_1. Real gas effects significantly modify the perfect gas relationships derived above [52]. Figure 2-5(a) shows that when the effects of vibrational excitation, dissociation, ionization and electronic excitation are taken into account, the density ratio ρ_2/ρ_1 can be as high as 14. The calculations of Kamel et al. [52] considered nitrogen for simplicity, but the results for air are qualitatively similar as

air comprises 78% nitrogen N_2 [110]. Real gas effects become significant only for very strong explosions: Mach number $M_1 = 10$ corresponds to pressure ratio $p_2/p_1 = 116.5$ and Mach number $M_1 = 30$ to pressure ratio $p_2/p_1 = 1050$. The real gas effects on the temperature jumps are shown in Figure 2-5(b).

In the case of water, the system of equations (2.25-2.27) is closed through the isentrope approximation (2.18) which renders the energy equation unnecessary. Assuming that the fluid to the left of the shock is stationary $u_1 = 0$ m·s^{-1} and at the reference state, $p_1 = p_0$, $\rho_1 = \rho_0$, the system is simplified to

$$\rho_2(u_2 + U_s) = \rho_1 U_s \tag{2.41}$$

$$B\left(\left(\frac{\rho_2}{\rho_1}\right)^{\Gamma_0+1} - 1\right) = -\rho_1 U_s u_2 \tag{2.42}$$

from which the shock speed is found to be

$$U_s^2 = \frac{B}{\rho_1}\frac{\rho_2}{\rho_1}\frac{\left(\frac{\rho_2}{\rho_1}\right)^{\Gamma_0+1} - 1}{\frac{\rho_2}{\rho_1} - 1}. \tag{2.43}$$

Setting $\rho_2/\rho_1 = 1 + x$ and assuming that x is small (as it would be for most liquids satisfying Tait's equation of state (2.18)), a first order approximation for U_s^2 may be obtained[1]:

$$U_s^2 \approx \frac{B}{\rho_1}(1+x)\frac{(\Gamma_0+1)x + \frac{\Gamma_0(\Gamma_0+1)}{2}x^2}{x} \approx \frac{B(\Gamma_0+1)}{\rho_1}\left(1 + \left(1 + \frac{\Gamma_0}{2}\right)x\right). \tag{2.44}$$

Using $\sqrt{1+\epsilon} \approx 1 + \frac{1}{2}\epsilon$ we arrive at

$$U_s \approx \sqrt{\frac{B(\Gamma_0+1)}{\rho_1}}\left(1 + \frac{\Gamma_0+2}{4}x\right). \tag{2.45}$$

This result implies that the reference sound speed in the liquid is $a_0 = \sqrt{\frac{B(\Gamma_0+1)}{\rho_1}}$. Using the values of the parameters quoted in Section 2.1.2, the sound speed is found

[1]For liquids satisfying Tait's equation of state, it is more convenient to use the density ratio ρ_2/ρ_1 as the independent variable characterizing the shock (as opposed to the pressure ratio p_2/p_1).

Table 2.1: Properties of shock waves with density ratio $\rho_2/\rho_1 = 1.05$ advancing into a stationary fluid at pressure $p_1 = 1.048 \times 10^5$ Pa.

fluid	ρ_2/ρ_1	p_s/p_1	p_2/p_1	U_s [m·s^{-1}]	a_1 [m·s^{-1}]
air	1.05	0.0707	1.0707	360.46	340.42
water	1.05	1252.3	1253.3	1633.0	1474.8

to be $a_0 = 1474.8$ m·s^{-1} which is within the typical range of 1450-1500 m·s^{-1} quoted in the literature for water at room temperature [121].

The particle velocity u_2 behind the shock is found to be

$$u_2 = -\frac{B}{\rho_1}\frac{\left(\frac{\rho_2}{\rho_1}\right)^{\Gamma_0+1} - 1}{U_s}, \tag{2.46}$$

which can be approximated up to second order in x as

$$u_2 \approx -\sqrt{\frac{B(\Gamma_0+1)}{\rho_1}}x\left(1 + \frac{\Gamma_0 - 2}{4}x\right). \tag{2.47}$$

The second order expression for the pressure p_2 follows directly from (2.18)

$$p_2 \approx p_1 + B(\Gamma_0+1)x\left(1 + \frac{\Gamma_0}{2}x\right). \tag{2.48}$$

Anderson [2] suggests that a fluid flow should be considered compressible if the density of the fluid changes by more than 5%. Using equations (2.18) and (2.40) we conclude that compressibility effects cannot be neglected for shock waves with overpressure ratios p_s/p_1 larger than 0.0707 and 1252.3 for air and water, respectively. A list of properties of interest of shock waves at these pressure ratios is given in Table 2.1. The table shows that conventional explosions generate strong shock waves in air and acoustic waves in water implying that the wave propagation processes in water and air are not only quantitatively, but also qualitatively different.

2.1.4 The Acoustic Limit

Many of the developments in this thesis have the acoustic case as the limit of small amplitude waves because, as it was shown in the previous section, this limit is applicable to water up to very high overpressures p_s and provides the basis onto which the compressible theory builds up. For completeness the acoustic theory is summarized in this section.

The mass (2.1) and momentum (2.2) conservation equation for one dimensional inviscid flow take the form

$$\frac{\partial \rho}{\partial t} + u\frac{\partial \rho}{\partial x} = -\rho\frac{\partial u}{\partial x}, \tag{2.49}$$

$$\frac{\partial u}{\partial t} + u\frac{\partial u}{\partial x} = -\frac{1}{\rho}\frac{\partial p}{\partial x}. \tag{2.50}$$

In the acoustic theory it is assumed that the density, pressure and velocity fields experience small perturbations $\tilde{\rho}$, $\tilde{p}$ and $\tilde{u}$ around an initial state $\bar{\rho}$, $\bar{p}$ and $\bar{u} = 0$ $\mathrm{m{\cdot}s^{-1}}$:

$$\rho = \bar{\rho} + \tilde{\rho}, \tag{2.51}$$

$$p = \bar{p} + \tilde{p}, \tag{2.52}$$

$$u = \bar{u} + \tilde{u} \tag{2.53}$$

and the governing equations take the form

$$\frac{\partial \tilde{\rho}}{\partial t} + \bar{\rho}\frac{\partial \tilde{u}}{\partial x} = 0 \tag{2.54}$$

$$\bar{\rho}\frac{\partial \tilde{u}}{\partial t} = -\frac{\partial \tilde{p}}{\partial x}. \tag{2.55}$$

Differentiating (2.54) with respect to t and (2.55) with respect to x and cross substituting gives

$$\frac{\partial^2 \tilde{\rho}}{\partial t^2} - \frac{\partial^2 \tilde{p}}{\partial x^2} = 0. \tag{2.56}$$

The sound speed (2.31) can be obtained as :

$$a^2 = \left.\frac{\partial p}{\partial \rho}\right|_{s=const.} = \frac{\tilde{p}}{\tilde{\rho}}, \tag{2.57}$$

and upon substitution in (2.56) gives

$$\frac{\partial^2 \tilde{p}}{\partial t^2} - a^2 \frac{\partial^2 \tilde{p}}{\partial x^2} = 0, \tag{2.58}$$

$$\frac{\partial^2 \tilde{\rho}}{\partial t^2} - a^2 \frac{\partial^2 \tilde{\rho}}{\partial x^2} = 0. \tag{2.59}$$

These expressions indicate that the propagation of weak pressure and density disturbances in an acoustic medium is governed by the linear wave equation with wave propagation speed a. The general solution of equation (2.58) was given by D'Alambert [133] in the form $\tilde{p} = f(x-at)+g(x+at)$ where f and g are arbitrary functions which can be determined from the initial conditions. The corresponding expressions for the velocity $\tilde{u}$ and density $\tilde{\rho}$ are obtained from equations (2.55) and (2.57), respectively, as

$$\tilde{u} = \frac{1}{a\bar{\rho}} \left(f(x-at) - g(x+at) \right), \tag{2.60}$$

$$\tilde{\rho} = \frac{1}{a^2} \left(f(x-at) + g(x+at) \right). \tag{2.61}$$

2.2 Wave Reflections

2.2.1 Wave Reflection from Rigid Boundaries

Consider an acoustic wave $g(x+at)$ traveling to the left which meets a rigid wall at $x = 0$ m. The boundary condition is $\tilde{u}(x = 0, t) = 0$ m·s^{-1} and the rigid wall acts as the source of a wave traveling in the positive x direction. Substitution of the boundary condition in equation (2.60) implies that $f(-at) = g(at)$ for all times t and therefore the pressure at the wall is twice the pressure of the incoming wave, $\tilde{p}(x = 0, t) = 2g(at)$. It is customary to express this fact by saying that the reflection

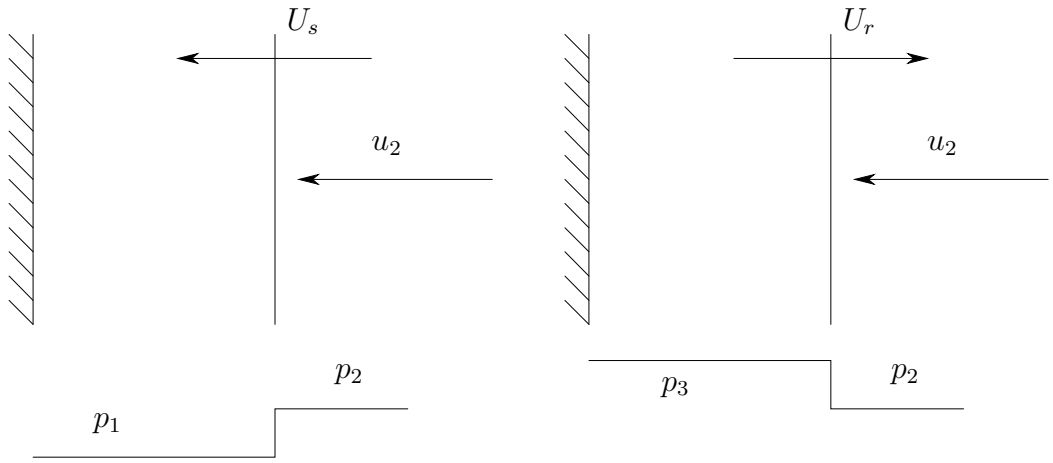

Figure 2-6: Reflection of a normal shock wave from a rigid wall.

Table 2.2: Reflection coefficient $C_R = p_r/p_s$ for air and water as a function of the incident overpressure ratio p_s/p_1 as obtained from equations (2.62) and (2.76), respectively.

p_s/p_1	0.01	1.0	3.0	10	30	100	1000	10000
air C_R	2.0086	2.7500	3.8000	5.5294	6.8649	7.6075	7.9583	7.9958
water C_R	2.0000	2.0002	2.0006	2.0019	2.0057	2.0187	2.1672	2.9142

coefficient for the acoustic wave is equal to 2.

The reflection of finite amplitude waves in air from rigid boundary departs significantly from acoustic theory even for overpressures as small as 1 atm and can be explained with the help of Figure 2-6. An incident wave of overpressure $p_s = p_2 - p_1$ approaches with speed U_s the fixed wall on the left, reflects from it and creates a reflected wave of overpressure $p_r = p_3 - p_1$ moving to the right at velocity U_r. Utilizing the Rankine-Hugoniot relations for a perfect gas, the reflection coefficient $C_R = p_r/p_s$ is found to be

$$C_R = \frac{p_r}{p_s} = \frac{(3\gamma - 1)\frac{p_s}{p_1} + 4\gamma}{(\gamma - 1)\frac{p_s}{p_1} + 2\gamma}. \tag{2.62}$$

The minimum value of the reflection coefficient is 2 for $p_s/p_1 \to 0$ and its maximum value is $\frac{3\gamma-1}{\gamma-1}$ for $p_s/p_1 \to \infty$ (for air with $\gamma = 1.4$, $\sup C_R = 8$). The behavior of equation (2.62) is shown in Figure 2-7 and some representative values of C_R are given in Table 2.2. The effects of compressibility become appreciable even for low incident overpressure ratios p_s/p_1 (for $p_s/p_1 = 1.0$ the reflection coefficient $C_R = p_r/p_s$ equals

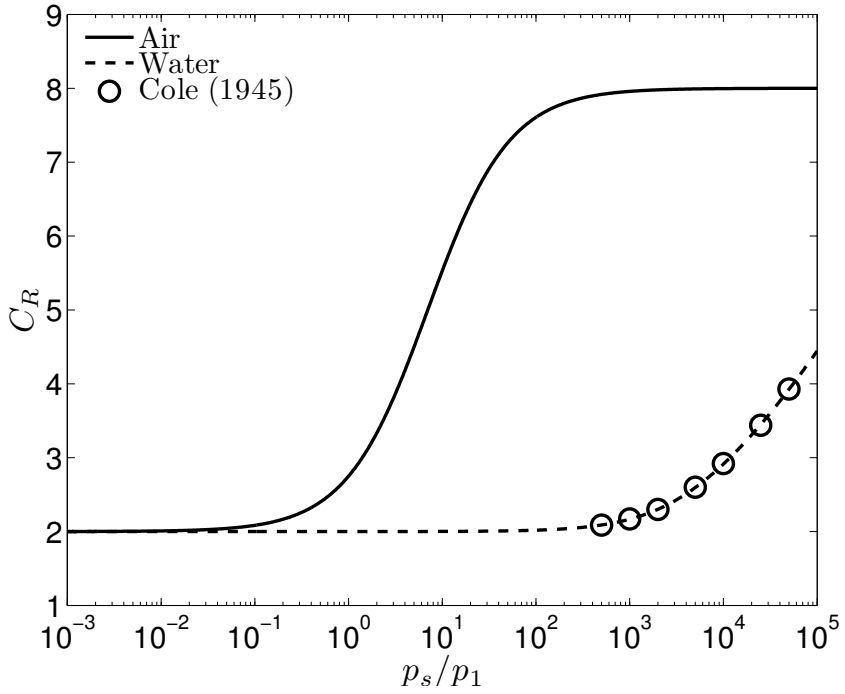

Figure 2-7: Variation of the reflection coefficient $C_R = p_r/p_s$ for air and water as a function of the incident overpressure ratio p_s/p_1. The circles represent the values reported by Cole [19].

2.75).

The density ratio ρ_3/ρ_1 of the reflected shock wave may also be expressed as a function of the incoming overpressure ratio p_s/p_1. More specifically, it is

$$\frac{\rho_3}{\rho_1} = \frac{\gamma\frac{p_s}{p_1} + \gamma}{(\gamma-1)\frac{p_s}{p_1} + \gamma}\frac{(\gamma+1)\frac{p_s}{p_1} + 2\gamma}{(\gamma-1)\frac{p_s}{p_1} + 2\gamma}, \tag{2.63}$$

with $\sup(\rho_3/\rho_1) = 21$. The variation of the density ratio ρ_3/ρ_1 with the overpressure ratio p_s/p_1, equation (2.63), is shown in Figure 2-4.

Similarly to the results for air presented above, relationships between the incident and reflected waves may also be derived for water. Tait's equation of state (2.18) makes it more convenient to use the density ratio ρ_2/ρ_1 as the independent variable and describe all parameters of the reflected shock in terms of it. The mass conservation, momentum conservation and the equation of state characterizing the incident

shock wave are:

$$\rho_2(u_2 - U_s) = -\rho_1 U_s, \tag{2.64}$$

$$p_2 - p_1 = \rho_1 U_s u_2, \tag{2.65}$$

$$p_2 - p_1 = B\left(\left(\frac{\rho_2}{\rho_1}\right)^{\Gamma_0+1} - 1\right). \tag{2.66}$$

The governing equations for the reflected wave are

$$\rho_2(u_2 + U_r) = \rho_3 U_r, \tag{2.67}$$

$$p_3 - p_2 = \rho_3 U_r u_2, \tag{2.68}$$

$$p_3 - p_1 = B\left(\left(\frac{\rho_3}{\rho_1}\right)^{\Gamma_0+1} - 1\right). \tag{2.69}$$

Subtracting (2.66) from (2.69) gives

$$p_3 - p_2 = B\left(\left(\frac{\rho_3}{\rho_1}\right)^{\Gamma_0+1} - \left(\frac{\rho_2}{\rho_1}\right)^{\Gamma_0+1}\right). \tag{2.70}$$

The shock velocities U_s and U_r can be expressed from (2.64) and (2.67)

$$U_s = \frac{\rho_2 u_2}{\rho_2 - \rho_1}, \tag{2.71}$$

$$U_r = \frac{\rho_2 u_2}{\rho_3 - \rho_1}. \tag{2.72}$$

Substituting these expressions into the momentum conservation equations (2.65) and (2.68) gives

$$B\left(\left(\frac{\rho_2}{\rho_1}\right)^{\Gamma_0+1} - 1\right) = \frac{\rho_1 \rho_2 u_2^2}{\rho_2 - \rho_1}, \tag{2.73}$$

$$B\left(\left(\frac{\rho_3}{\rho_1}\right)^{\Gamma_0+1} - \left(\frac{\rho_2}{\rho_1}\right)^{\Gamma_0+1}\right) = \frac{\rho_2 \rho_3 u_2^2}{\rho_3 - \rho_2}. \tag{2.74}$$

Division of the last two equations eliminates the unknown velocity u_2 and gives a

relationship between the density ratios ρ_2/ρ_1 and ρ_3/ρ_1

$$\frac{\left(\frac{\rho_3}{\rho_1}\right)^{\Gamma_0+1} - \left(\frac{\rho_2}{\rho_1}\right)^{\Gamma_0+1}}{\left(\frac{\rho_2}{\rho_1}\right)^{\Gamma_0+1} - 1} = \frac{\frac{\rho_3}{\rho_1}\left(\frac{\rho_2}{\rho_1} - 1\right)}{\frac{\rho_3}{\rho_1} - \frac{\rho_2}{\rho_1}}. \tag{2.75}$$

This equation cannot be solved explicitly for ρ_3/ρ_1, but its numerical evaluation is straightforward. Once the density ratio is obtained, the reflection coefficient C_R follows from

$$C_R = \frac{p_r}{p_s} = \frac{p_3 - p_1}{p_2 - p_1} = \frac{\left(\frac{\rho_3}{\rho_1}\right)^{\Gamma_0+1} - 1}{\left(\frac{\rho_2}{\rho_1}\right)^{\Gamma_0+1} - 1} = \frac{\frac{\rho_2}{\rho_1}\left(\frac{\rho_3}{\rho_1} - 1\right)}{\frac{\rho_3}{\rho_1} - \frac{\rho_2}{\rho_1}}. \tag{2.76}$$

The variation of C_R for water is shown in Figure 2-7 and compared with the data of Cole [19]. In clear contrast with the case of air, the reflection coefficient C_R for water remains close to the acoustic value of 2. Series expansion analysis of C_R sheds light into the nature of this behavior.

Equation (2.75) can be rewritten as

$$\left(\frac{\rho_2}{\rho_1}\right)^{\Gamma_0+2} - \frac{\rho_2}{\rho_1}\left(\frac{\rho_3}{\rho_1}\right)^{\Gamma_0+1} + \left(\frac{\rho_3}{\rho_1}\right)^{\Gamma_0+2} - \left(\frac{\rho_2}{\rho_1}\right)^{\Gamma_0+2}\frac{\rho_3}{\rho_1} + \frac{\rho_2}{\rho_1}\frac{\rho_3}{\rho_1} - \frac{\rho_3}{\rho_1} = 0. \tag{2.77}$$

Let $\rho_2/\rho_1 = 1 + x$ and $\rho_3/\rho_1 = 1 + ax + bx^2 + cx^3 + ...$ be the Taylor expansion of the reflected density ratio in terms of x. The terms in equation (2.77) can be expressed as

$$\left(\frac{\rho_2}{\rho_1}\right)^{\Gamma_0+2} = 1 + (\Gamma_0+2)x + \frac{(\Gamma_0+2)(\Gamma_0+1)}{2}x^2 + \frac{(\Gamma_0+2)(\Gamma_0+1)\Gamma_0}{6}x^3 + ... \tag{2.78}$$

$$\begin{aligned}\frac{\rho_2}{\rho_1}\left(\frac{\rho_3}{\rho_1}\right)^{\Gamma_0+1} =& 1 + ((\Gamma_0+1)a+1)x + (\Gamma_0+1)\left(a + b + \frac{\Gamma_0+2}{2}a^2\right)x^2 + \\ & (\Gamma_0+1)\left(b + c + \Gamma_0 ab + \frac{\Gamma_0+2}{2}a^2 + \frac{\Gamma_0(\Gamma_0-1)}{6}a^3\right)x^3 + ...\end{aligned} \tag{2.79}$$

$$\left(\frac{\rho_3}{\rho_1}\right)^{\Gamma_0+2} = 1 + (\Gamma_0+2)ax + (\Gamma_0+2)\left(b + \frac{\Gamma_0+1}{2}a^2\right)x^2 +$$

$$(\Gamma_0+2)\left(c+(\Gamma_0+1)ab+\frac{(\Gamma_0+1)\Gamma_0}{6}a^3\right)x^3+... \tag{2.80}$$

$$\left(\frac{\rho_2}{\rho_1}\right)^{\Gamma_0+2}\frac{\rho_3}{\rho_1}=1+(\Gamma_0+2+a)x+\left(\frac{(\Gamma_0+1)(\Gamma_0+2)}{2}+(\Gamma_0+2)a+b\right)x^2+ \left(\frac{(\Gamma_0+2)(\Gamma_0+1)\Gamma_0}{6}+\frac{(\Gamma_0+2)(\Gamma_0+1)}{2}a+(\Gamma_0+2)b+c\right)x^3+... \tag{2.81}$$

$$\frac{\rho_2}{\rho_1}\frac{\rho_3}{\rho_1}=1+(1+a)x+(a+b)x^2+(b+c)x^3+... \tag{2.82}$$

The zeroth and first order terms provide no specific information about a, b and c while the second order term leads to $a=2$ and the third order term to $b=2$. Substitution of the expansions of ρ_2/ρ_1 and ρ_3/ρ_1 in equation (2.76) gives the reflection coefficient up to first order:

$$C_r=\frac{a}{a-1}+\frac{a^2-a-b}{(a-1)^2}x+\mathcal{O}(x^2)=2+\mathcal{O}\left(\left(\frac{\rho_2}{\rho_1}-1\right)^2\right). \tag{2.83}$$

The reflection coefficient C_R is 2 up to first order in the density of the incoming wave explaining why C_R remains close to 2 up to very large pressure in Figure 2-7.

2.2.2 Wave Reflection from Free Boundaries

Consider an acoustic wave $g(x+at)$ traveling to the left which reaches a free boundary at $x=0$ m. The condition at the free boundary is $\tilde{p}(x=0,t)=0$ Pa. Similarly to the reflection from a rigid wall a right going wave is created. Substituting the general solution into the boundary condition gives $f(-at)=-g(at)$ implying the reflected wave is equal in magnitude and opposite in sign to the incoming wave. For a free boundary the reflection coefficient is 0, but the boundary point acquires a negative velocity $\tilde{u}(x=0,t)=-\frac{2g(at)}{a\bar{\rho}}$ (see equation (2.60)) implying that the free end moves to the left. Its displacement is first order within the acoustic theory, but can become quite large when the acoustic approximation breaks [51].

Wave reflection of finite amplitude waves from free boundaries is deferred to Chapter 4 where it will be considered in details.

Chapter 3

Solutions of Acoustic Blast Waves Interacting with Point Masses

This chapter contains the applications of the linear wave propagation theory for the analysis of the interaction of blast waves with point masses. The well established two wave solution method [133] is modified to account for the motion of the point masses and a level of generality sufficient for application to the problems of free-standing, supported and actively deployed masses is kept.

3.1 The General Solution Method

Consider an acoustic wave $f(x-at)$ traveling in the positive x direction towards a plate of mass per unit area m_p (Figure 3-1). At time t the plate is located at position $\xi(t)$ and has a reaction force per unit area $r(t,\xi,\dot{\xi},...)$ acting on it in the negative x direction. The reaction force r is the excess pressure (possibly negative) over the ambient pressure and represents the reaction of the plate supports, e.g. springs, dampers, fluids, etc. The ambient pressure in the fluid domain $x \leq 0$ is assumed to be exactly balanced by an additional force (not shown in the figure) on the plate's right hand side leaving it motionless until the arrival of the wave. For simplicity it will be assumed that $\xi(t=0) = 0$ m and that the wave reaches the plate at time $t = 0$ s. Similarly to the wave reflections from rigid walls and free boundaries, once the

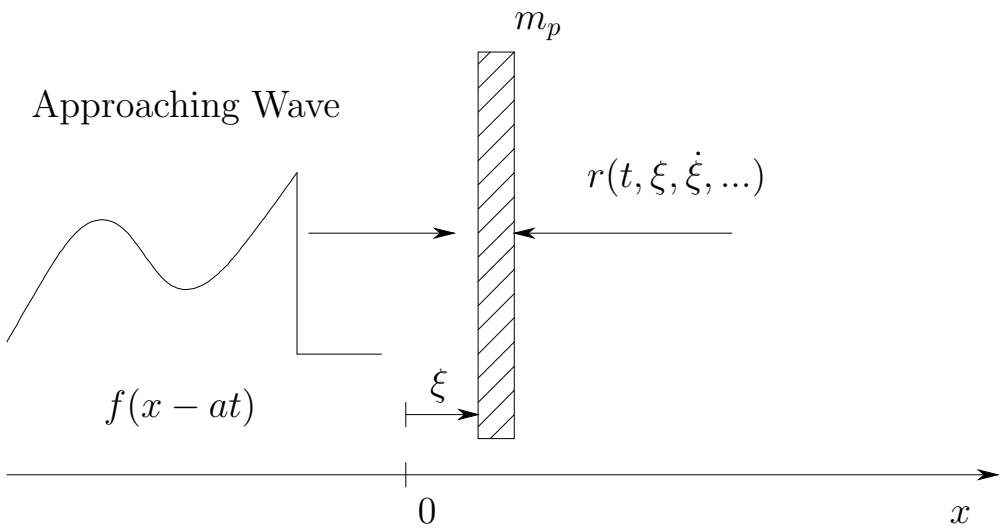

Figure 3-1: An acoustic wave f of arbitrary shape approaching a plate of mass per unit area m_p.

wave reaches the plate a reflected wave $g(x+at)$ traveling in the negative x direction is created making the total pressure perturbation on the left hand side of the plate $\tilde{p} = f(x-at) + g(x+at)$. The motion of the plate is governed by Newton's Second Law,

$$m_p \ddot{\xi} = f(\xi - at) + g(\xi + at) - r(t, \xi, \dot{\xi}, ...). \tag{3.1}$$

The motion of the fluid particle on the left side of the plate is governed by the conservation equations (2.1-2.3). In particular the momentum conservation equation (2.2) takes the form

$$\rho \frac{d^2\xi}{dt^2} = \rho \left(\frac{\partial u}{\partial t} + u \frac{\partial u}{\partial x} \right) = -\frac{\partial p}{\partial x} = -f'(\xi - at) - g'(\xi + at). \tag{3.2}$$

The reflected wave $g(x+at)$ is unknown and can be eliminated by differentiating (3.1) with respect to t, multiplying (3.2) with $\dot{\xi}+a$ and adding the resulting equations. The final differential equation for ξ is

$$m_p \dddot{\xi} + (\dot{\xi} + a)\rho \ddot{\xi} = -2af'(\xi - at) - \frac{d}{dt}(r(t, \xi, \dot{\xi}, ...)). \tag{3.3}$$

This equation is not an equation for ξ as it still contains the density of the particle next

to the plate $\rho = \rho(t, \xi)$. Within the acoustic approximation, a first order perturbation of the density $\rho = \bar{\rho} + \tilde{\rho}(t, \xi)$ can be assumed, where $\bar{\rho}$ is the background ambient density and $\tilde{\rho}(t, \xi)$ is the perturbation over the ambient state. The displacement $\xi(t)$ is also assumed to be small as well as are its derivatives, $\dot{\xi}(t)$ and $\ddot{\xi}(t)$. Ignoring the second order term containing $\tilde{\rho}$ and realizing that $\dot{\xi} \ll a$ implies $f'(\xi - at) \approx f'(-at)$, (3.3) simplifies to:

$$m_p \dddot{\xi} + a\bar{\rho}\ddot{\xi} = -2af'(-at) - \frac{d}{dt}(r(t, \xi, \dot{\xi}, ...)). \tag{3.4}$$

When f and r are specified together with an appropriate set of initial conditions, equation (3.4) can be solved for the displacement ξ. From the solution all quantities of interest such as impulse and energy transmitted to the plate can be determined. The reflected wave g can be found from the first order approximation of equation (3.1)

$$g(at) = m_p\ddot{\xi} - f(-at) + r(t, \xi, \dot{\xi}, ...), \tag{3.5}$$

from which the pressure field

$$\tilde{p}(x, t) = f(x - at) + g(x + at) \tag{3.6}$$

in the fluid domain can be obtained.

3.2 Response of Free-Standing Plates

In this section the general solution approach described above is used to derive a number of relevant cases of acoustic waves interacting with free-standing structures.

3.2.1 Uniform Wave Profile

One of the simplest cases to solve arises when there is no excess force applied on the right hand side $r(t) = 0$ Pa, $\forall t$ and the incident wave is uniform

$$f(x - at) = \begin{cases} 0, & x \geq at \\ p_s, & x < at \end{cases} . \tag{3.7}$$

The governing equation (3.4) becomes

$$m_p \dddot{\xi} + a\bar{\rho}\ddot{\xi} = 0 \tag{3.8}$$

with initial conditions

$$\xi(t = 0) = 0, \tag{3.9}$$

$$\dot{\xi}(t = 0) = 0, \tag{3.10}$$

$$\ddot{\xi}(t = 0) = \frac{2p_s}{m_p}. \tag{3.11}$$

The factor of 2 is present in the condition for the acceleration because the initially stationary plate behaves instantaneously as a rigid wall and the wave reflects completely. The solution for the displacement ξ is found to be

$$\xi = \frac{2p_s}{\bar{\rho}^2 a^2} \left(e^{-\frac{\bar{\rho}a}{m_p}t} - 1 \right) + \frac{2p_s}{\bar{\rho}a} t \tag{3.12}$$

with

$$\dot{\xi} = -\frac{2p_s}{\bar{\rho}a} e^{-\frac{\bar{\rho}a}{m_p}t} + \frac{2p_s}{\bar{\rho}a}, \tag{3.13}$$

$$\ddot{\xi} = \frac{2p_s}{m_p} e^{-\frac{\bar{\rho}a}{m_p}t}. \tag{3.14}$$

The solution clearly reveals that the fluid-structure interaction is governed by the time scale $t^* = m_p/\bar{\rho}a$.

A quantity of interest is the maximum impulse acquired by the plate as a fraction

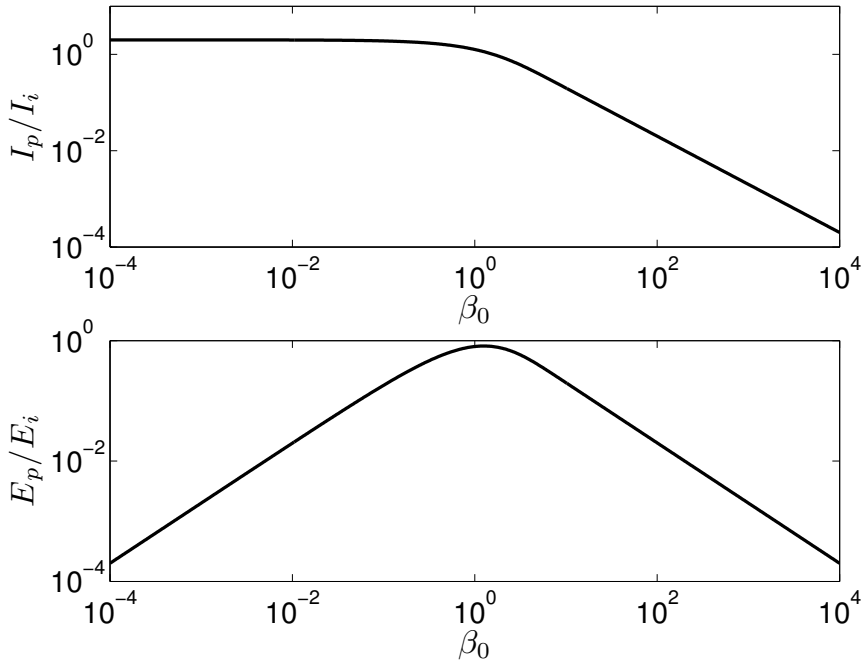

Figure 3-2: Transmitted impulse and energy as given by equations (3.15) and (3.16).

of the impulse available in the incident wave $I_i = \int_0^{t_i} \tilde{p} dt = p_s t_i$. The available impulse I_i can be interpreted as the impulse carried by the incident pressure wave through the point $x = 0$ from $t = 0$ up to the moment of interest $t = t_i$ which can be chosen arbitrarily. The maximum impulse is

$$\frac{I_p}{I_i} = \frac{\max\limits_{0 \le t \le t_i} \left(m_p \dot{\xi}(t) \right)}{p_s t_i} = 2 \frac{1 - e^{-\beta_0}}{\beta_0}, \tag{3.15}$$

where the non-dimensional parameter β_0 describes the fluid-structure interaction. This non-dimensional parameter $\beta_0 = t_i/t^*$ compares the relative time scales of the fluid structure interaction t^* and the incident wave t_i. It was first identified by Taylor [119] in the context of exponentially decaying pressure waves and plays an important role in the description of the interactions between blast waves and plates. A plot of the dependence of the transmitted impulse I_p/I_i on β_0 on log-log scale is shown in Figure 3-2. The transmitted impulse is a monotonically decreasing function of β_0 implying that less impulse is transmitted to lighter plates. As it can be seen in the figure, the function I_p/I_i asymptotes to a constant value of 2 for small β_0 and $2/\beta_0$

for large β_0. These asymptotes will be used as a basis for extending (3.15) to the compressible range in Chapter 4.

Similarly to the impulse, the maximum kinetic energy transmitted to the plate is found to be

$$\frac{E_p}{E_i} = \frac{\max\limits_{t\geq 0}\left(\frac{m_p\dot{\xi}^2(t)}{2}\right)}{\frac{p_s^2 t_i}{\bar{\rho}a}} = 2\frac{\left(1-e^{-\beta_0}\right)^2}{\beta_0}, \tag{3.16}$$

where $E_i = p_s^2 t_i/\bar{\rho}a$ is a non-dimentionalization constant[1]. The dependence of the transmitted energy on the fluid-structure interaction parameter β_0 is also shown in Figure 3-2. The transmitted energy achieves its maximum at $\beta_0 = 1.2564$ which is the positive solution of $e^{-\beta_0}(2\beta_0+1) = 1$. There is a resonance-like behavior around $\beta_0 = 1.2564$ and unlike the momentum, the energy transmitted to the plate can be reduced with either very light plates or with very heavy plates. The energy ratio E_p/E_i asymptotes to $2\beta_0$ for small β_0 and $2/\beta_0$ for large β_0.

The reflected wave is $g(at) = p_s\left(2e^{-\frac{\bar{\rho}a}{m_p}t} - 1\right)$ and the pressure field within the fluid domain is

$$\tilde{p}(x, t\geq 0) = \begin{cases} 2p_s e^{-\frac{\bar{\rho}}{m_p}(x+at)}, & x+at \geq 0 \\ p_s, & x+at < 0 \end{cases}. \tag{3.17}$$

In water if the pressure $\tilde{p}(x,t)$ becomes negative the fluid cavitates and the analysis ceases to be valid [119]. Methods extending the solutions beyond the cavitation time have been proposed, but in this work the interaction between the blast waves and the plates will be considered only until the point of cavitation [53, 70]. According to equation (3.17) the pressure remains positive at all times and therefore no cavitation occurs when uniform waves interact with free-standing rigid plates.

3.2.2 Exponential Wave Profile

This problem was studied by G. I. Taylor [119] during the Second World War in connection with underwater explosion damage to ship hulls. For completeness, we provide a derivation of Taylor's solution and give some additional details about the transmitted energy.

[1] E_i can be interpreted as the "pressure" energy carried by the wave.

An exponential pressure wave of the form

$$f(x-at) = \begin{cases} p_s e^{\frac{x-at}{at_i}}, & x-at \leq 0 \\ 0, & x-at > 0 \end{cases} \tag{3.18}$$

is considered. Equation (3.4) takes the form

$$m_p \dddot{\xi} + a\bar{\rho}\ddot{\xi} = -2\frac{p_s}{t_i}e^{-\frac{t}{t_i}} \tag{3.19}$$

with initial conditions (3.9-3.11). Equation (3.19) can be rewritten in the non-dimensional form

$$\frac{d^3\zeta}{d\tau^3} + \beta_0 \frac{d^2\zeta}{d\tau^2} = -2\beta_0 e^{-\tau} \tag{3.20}$$

with the initial conditions becoming

$$\zeta(\tau = 0) = 0, \tag{3.21}$$

$$\frac{d\zeta}{d\tau}(\tau = 0) = 0, \tag{3.22}$$

$$\frac{d^2\zeta}{d\tau^2}(\tau = 0) = 2\beta_0, \tag{3.23}$$

where the non-dimensional displacement $\zeta = \frac{a\bar{\rho}\xi}{p_s t_i}$ and time $\tau = t/t_i$ have been introduced. In these equations, the single fluid-structure interaction parameter is defined as $\beta_0 = t_i/t^*$ where $t^* = m_p/\bar{\rho}a$ represents the characteristic time of the fluid-structure interaction. Physically, β_0 may also be interpreted as the relative inertia of the volume of compressed gas $\bar{\rho}at_i$ and the plate m_p:

$$\beta_0 = \frac{a\bar{\rho}t_i}{m_p}. \tag{3.24}$$

The solution of equation (3.20) is

$$\zeta = 2 + \frac{2\beta_0}{1-\beta_0}e^{-\tau} - \frac{2}{1-\beta_0}e^{-\beta_0\tau} \tag{3.25}$$

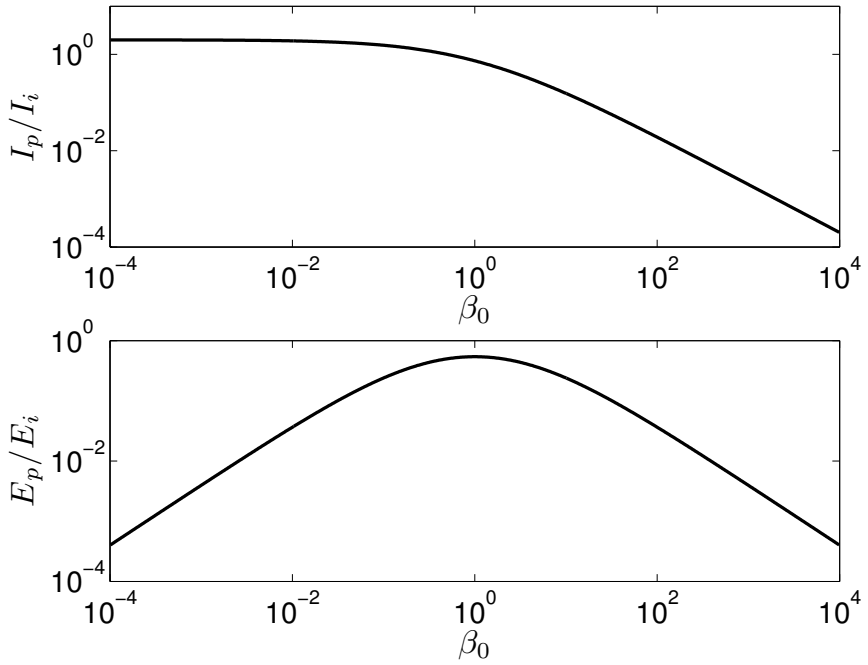

Figure 3-3: Transmitted impulse and energy for an exponential incident wave profile

with

$$\frac{d\zeta}{d\tau} = \frac{2\beta_0}{1-\beta_0}\left(e^{-\beta_0\tau} - e^{-\tau}\right), \tag{3.26}$$

$$\frac{d^2\zeta}{d\tau^2} = \frac{2\beta_0}{1-\beta_0}\left(e^{-\tau} - \beta_0 e^{-\beta_0\tau}\right). \tag{3.27}$$

The maximum transmitted impulse

$$\frac{I_p}{I_i} = \max_{\tau\geq 0}\left(\frac{1}{\beta_0}\frac{d\zeta}{d\tau}\right) = 2\beta_0^{\frac{\beta_0}{1-\beta_0}} \tag{3.28}$$

and energy

$$\frac{E_p}{E_i} = \max_{\tau\geq 0}\left(\frac{1}{\beta_0}\left(\frac{d\zeta}{d\tau}\right)^2\right) = 4\beta_0^{\frac{1+\beta_0}{1-\beta_0}} \tag{3.29}$$

are achieved simultaneously at time

$$\tau_m = \frac{\log\beta_0}{\beta_0 - 1} \tag{3.30}$$

which is a decreasing function of β_0. Figure 3-3 shows plots of I_p/I_i and E_p/E_i versus

β_0. The overall shape of these curves is found to be similar to those obtained for uniform wave profiles in Section 3.2.1. The non-dimensionalization of the impulse curve is accomplished through division by $I_i = \int_0^\infty \tilde{p} dt = t_i \int_0^\infty p_s e^{-\tau} d\tau = p_s t_i$. The function I_p/I_i asymptotes to 2 for small β_0 and to $2/\beta_0$ for large β_0. Similarly to the case of uniform wave profiles, Figure 3-3 indicates that the impulse transmitted to lighter plates is less. The dependence of the energy transmission on β_0 is inversion invariant, i.e. it has the property $f(\beta_0) = f(1/\beta_0)$, and is symmetric with respect to $\beta_0 = 1$ where it attains its maximum value $E_p/E_i = 4/e^2 < 1$. The asymptotes are $E_p/E_i = 4\beta_0$ for small β_0 and $E_p/E_i = 4/\beta_0$ for large β_0.

The advantage of sandwich over solid plates of the same mass can be explained in terms of the impulse and energy curves as follows. Consider a sandwich plate with mass of the front face sheet m_p such that the corresponding fluid-structure interaction parameter β_0 is greater than 1, $\beta_0 > 1$. If the front face sheet thickness is reduced by a factor of 2, its mass reduces by a factor of 2 to $m_p/2$, and the effective fluid-structure interaction parameter doubles to $2\beta_0$. Approximating the impulse and energy curves in Figure 3-3 by their asymptotes in the region $\beta_0 > 1$, one can immediately conclude that both the transmitted impulse I_p/I_i and the transmitted energy E_p/E_i are reduced by a factor of 2 for the face sheet with the reduced mass. This reduction effect is responsible for the advantageous response of sandwich plates with thinner face sheets to blast waves. Similar parallel can be drawn when comparing a sandwich and monolithic plates of the same mass as the front face sheet of the sandwich is necessarily lighter than the monolithic plate itself.

It should be noted that reducing the plate mass in the region $\beta_0 < 0.5$ is detrimental for the blast performance. Consider a sandwich plate with front face sheet mass m_p such that $\beta_0 < 0.5$. If the thickness of the face sheet is reduced by a factor of 2, the mass of the face sheet again becomes $m_p/2$ and the effective fluid-structure interaction parameter is again doubled to $2\beta_0 < 1$. However in the region $\beta_0 < 1$, the momentum transmission curve can be approximated by a constant asymptote implying no reduction in the transmitted impulse. Using similar asymptotic approximation for the energy transmission E_p/E_i we observe that it actually doubles. This implies

loss rather than increase in performance for the sandwich plate with the lighter face sheet in the region $\beta_0 < 1$, hence care must be exercised when trying to utilize sandwich plates for blast protection as having a light front face sheet is not necessarily always beneficent. The transition between the asymptotes happens in a vicinity of $\beta_0 = 1$ and potential advantages or disadvantages of the use of sandwich plates with values of the fluid-structure interaction parameter in that region must be evaluated using more precise approaches.

For water, it is important to evaluate the range of validity of this analysis by identifying the cavitation point. Utilizing the non-dimensional reflected wave g

$$\frac{g(\tau)}{p_s} = \frac{1+\beta_0}{1-\beta_0} e^{-\tau} - \frac{2\beta_0}{1-\beta_0} e^{-\beta_0 \tau} \tag{3.31}$$

the pressure in the fluid domain is found to be

$$\frac{\tilde{p}(\chi,\tau)}{p_s} = \begin{cases} \frac{1+\beta_0}{1-\beta_0} e^{-\chi-\tau} - \frac{2\beta_0}{1-\beta_0} e^{-\beta_0(\chi+\tau)} + e^{\chi-\tau}, & \chi+\tau \geq 0 \\ e^{\chi-\tau}, & \chi+\tau < 0 \end{cases}, \tag{3.32}$$

where the non-dimensional location $\chi = x/at_i$ has been introduced. It can be assumed that cavitation occurs when the minimum pressure becomes 0, i.e. when $\tilde{p}(\chi_c, \tau_c) = 0$ and $\frac{\partial \tilde{p}}{\partial \chi}(\chi_c, \tau_c) = 0$ [70]. Both conditions are satisfied only when $\chi_c = 0$ and $\tau_c = \tau_m$. Thus cavitation occurs at the front face of the plate at the instant when the plate has achieved its maximum velocity. The location of the plate at the time of cavitation, which is also the time of maximum plate velocity, can be obtained from equation (3.25) as

$$\zeta(\tau_m) = 2 - 2(1+\beta_0)\beta_0^{\frac{\beta_0}{1-\beta_0}} \tag{3.33}$$

and achieves a maximum for $\beta_0 = 1$. For water, the dimensional displacement $\xi(\tau_m)$ remains small (less than 0.04m for blast overpressure of 1 GPa) due to the large speed of sound and density of water, but for air this displacement can become large (on the order of 1 meter) and intolerable [51].

3.3 Response of Supported Plates

In this section the general solution approach described in Section 3.1 is used to derive a number of relevant cases of acoustic waves interacting with supported structures.

3.3.1 Perfectly Plastic Support

The interaction between an exponential blast wave and a plate on a perfectly plastic support was considered by Hutchinson and Xue [46]. Their analysis has been extended to sandwich plates with perfectly plastic cores by Deshpande and Fleck [29] who included the effect of plastic wave propagation within the core. In this section the model of Hutchinson and Xue will be reviewed and some new insights into the impulse and energy transmission will be provided.

For the case of a perfectly plastic support the reaction force is a discontinuous function of the plate velocity $\dot{\xi}$. If the plate is moving to the right, the reaction force is $r(\dot{\xi} > 0) = \sigma_c$. If the plate is stationary, $\dot{\xi} = 0$ the reaction force can take any value between 0 and σ_c necessary to keep the plate stationary. Definition of the reaction force for $\dot{\xi} < 0$ is not required as the solution derived in this section ceases to be valid before the velocity $\dot{\xi}$ becomes negative. In the follow up analysis it will be assumed that $\sigma_c < 2p_s$ so that the support undergoes plastic deformation. Otherwise the problem degenerates to reflection from a rigid wall.

The governing equation for the displacement until the moment at which the velocity $\dot{\zeta}$ becomes zero is the same as in the case of no support, namely equation (3.20). Its initial conditions are slightly modified and become

$$\zeta(\tau = 0) = 0, \tag{3.34}$$

$$\frac{d\zeta}{d\tau}(\tau = 0) = 0, \tag{3.35}$$

$$\frac{d^2\zeta}{d\tau^2}(\tau = 0) = \left(2 - \frac{\sigma_c}{p_s}\right)\beta_0. \tag{3.36}$$

The solution for the non-dimensional displacement is

$$\zeta = 2 + \frac{\sigma_c}{p_s}\left(\frac{1}{\beta_0} - \tau\right) - \left(\frac{1}{\beta_0}\frac{\sigma_c}{p_s} + \frac{2}{1-\beta_0}\right)e^{-\beta_0\tau} + \frac{2\beta_0}{1-\beta_0}e^{-\tau} \tag{3.37}$$

with

$$\frac{d\zeta}{d\tau} = -\frac{\sigma_c}{p_s} + \left(\frac{\sigma_c}{p_s} + \frac{2\beta_0}{1-\beta_0}\right)e^{-\beta_0\tau} - \frac{2\beta_0}{1-\beta_0}e^{-\tau}, \tag{3.38}$$

$$\frac{d^2\zeta}{d\tau^2} = -\left(\beta_0\frac{\sigma_c}{p_s} + \frac{2\beta_0^2}{1-\beta_0}\right)e^{-\beta_0\tau} + \frac{2\beta_0}{1-\beta_0}e^{-\tau}. \tag{3.39}$$

For no resistance force, $\sigma_c = 0$ Pa, these expressions simplify to Taylor's solution. The maximum transmitted impulse

$$\frac{I_p}{I_i} = \max_{\tau\geq 0}\left(\frac{1}{\beta_0}\frac{d\zeta}{d\tau}\right) = \frac{2}{\beta_0}\left(\beta_0 + \frac{\sigma_c}{p_s}\frac{1-\beta_0}{2}\right)^{\frac{1}{1-\beta_0}} - \frac{1}{\beta_0}\frac{\sigma_c}{p_s} \tag{3.40}$$

and energy

$$\frac{E_p}{E_i} = \max_{\tau\geq 0}\left(\frac{1}{\beta_0}\left(\frac{d\zeta}{d\tau}\right)^2\right) = \frac{1}{\beta_0}\left(2\left(\beta_0 + \frac{\sigma_c}{p_s}\frac{1-\beta_0}{2}\right)^{\frac{1}{1-\beta_0}} - \frac{\sigma_c}{p_s}\right)^2, \tag{3.41}$$

are achieved simultaneously at $\tau_m = (\beta_0 - 1)^{-1}\log\left(\beta_0 + \frac{\sigma_c}{p_s}\frac{1-\beta_0}{2}\right)$. Their dependence on the resistance force σ_c is shown in Figure 3-4. In addition to the expected behavior that a larger resistance force leads to a larger reduction in the impulse and the energy, it can be seen that heavier plates benefit more from presence of the plastic supports. The effect is due to the longer time period τ_m (see Figure 3-5) during which the resistance force σ_c acts on the plate canceling a larger fraction of the transmitted impulse. The larger benefits occurring for heavier plates form a recurring pattern which appears again in later developments including the analysis of viscoelastic supports and active protection concepts.

The results above are valid only until the onset of cavitation. The expressions for

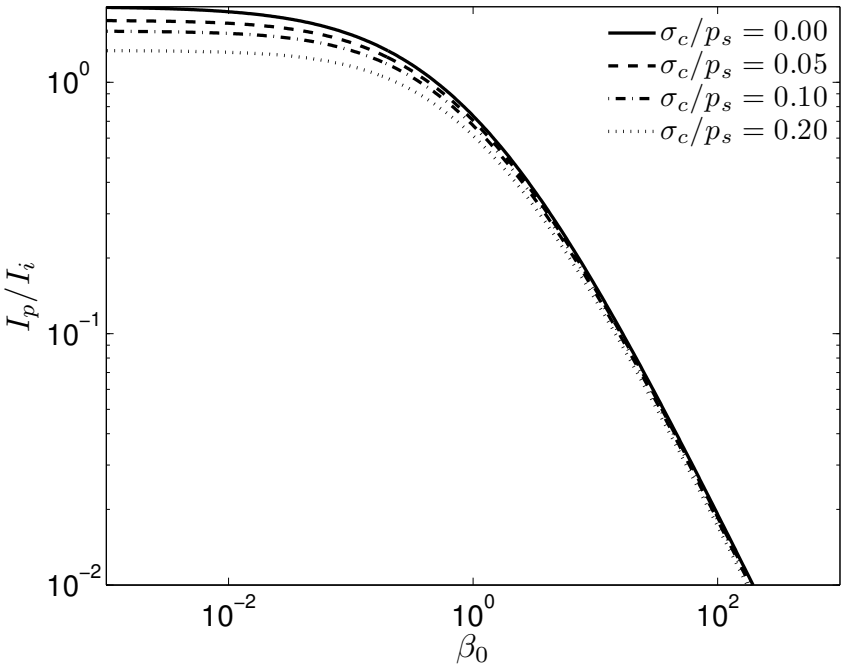

(a) Impulse

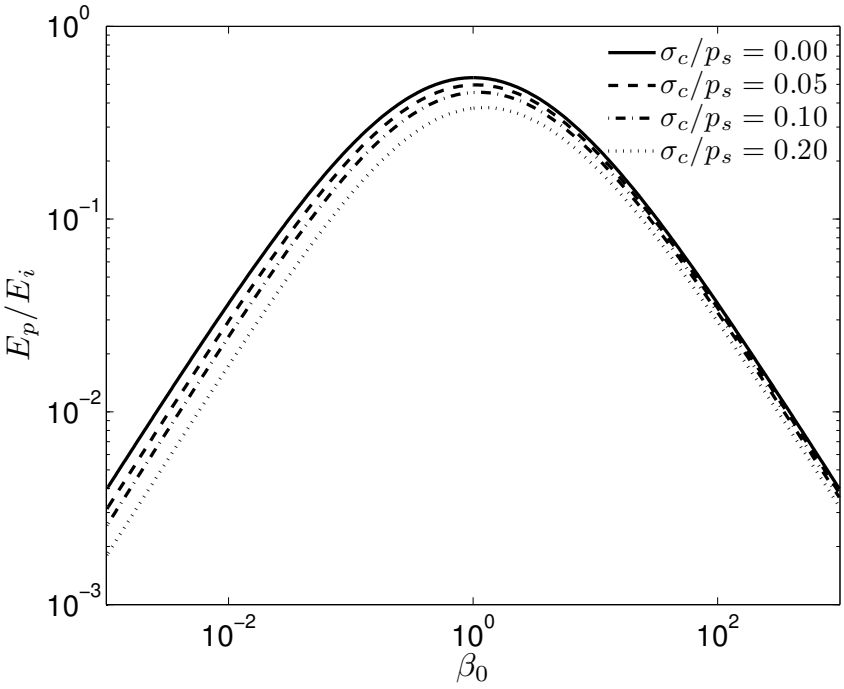

(b) Energy

Figure 3-4: Maximum transmitted impulse I_p/I_i and energy E_p/E_i versus β_0 for different relative strengths of the plate support σ_c/p_s.

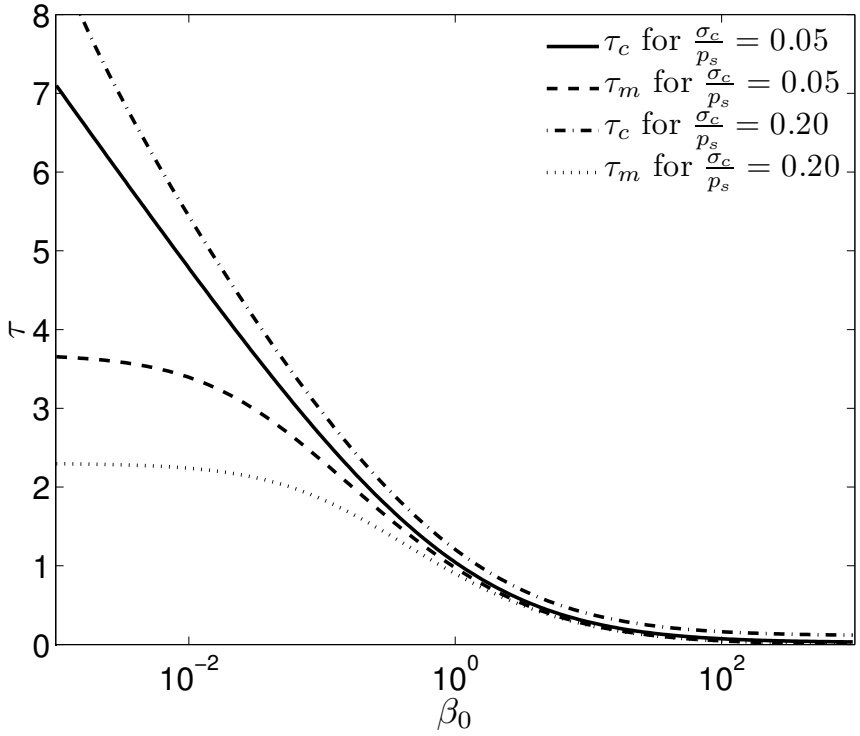

Figure 3-5: The cavitation time τ_c is always larger than the maximum velocity time τ_m. The difference between τ_c and τ_m is especially large for heavy plates (small β_0).

the reflected wave g and the pressure $\tilde{p}$ are

$$\frac{g(\tau)}{p_s} = \frac{\sigma_c}{p_s} - \left(\frac{\sigma_c}{p_s} + \frac{2\beta_0}{1-\beta_0}\right) e^{-\beta_0 \tau} + \frac{1+\beta_0}{1-\beta_0} e^{-\tau} \tag{3.42}$$

and

$$\frac{\tilde{p}(\chi,\tau)}{p_s} = \frac{\sigma_c}{p_s} - \left(\frac{\sigma_c}{p_s} + \frac{2\beta_0}{1-\beta_0}\right) e^{-\beta_0(\chi+\tau)} + \frac{1+\beta_0}{1-\beta_0} e^{-\chi-\tau} + e^{\chi-\tau}, \tag{3.43}$$

respectively. Cavitation occurs at location χ_c and time τ_c for which the conditions $\tilde{p}(\chi_c, \tau_c) = 0$ and $\frac{\partial \tilde{p}}{\partial \chi}(\chi_c, \tau_c) = 0$ are satisfied. It was shown in Section 3.2.2 that for the case of a free-standing plate cavitation occurs when the plate achieves its maximum velocity. In contrast, in the case of a plastic support cavitation occurs later while the plate is slowing down (see Figure 3-5). The difference between τ_c and τ_m is largest for small values of β_0 and becomes negligible at values of $\beta_0 \geq 1$. Additionally a difference in the trends of τ_c and τ_m with σ_c/p_s can be seen. Increases in the relative

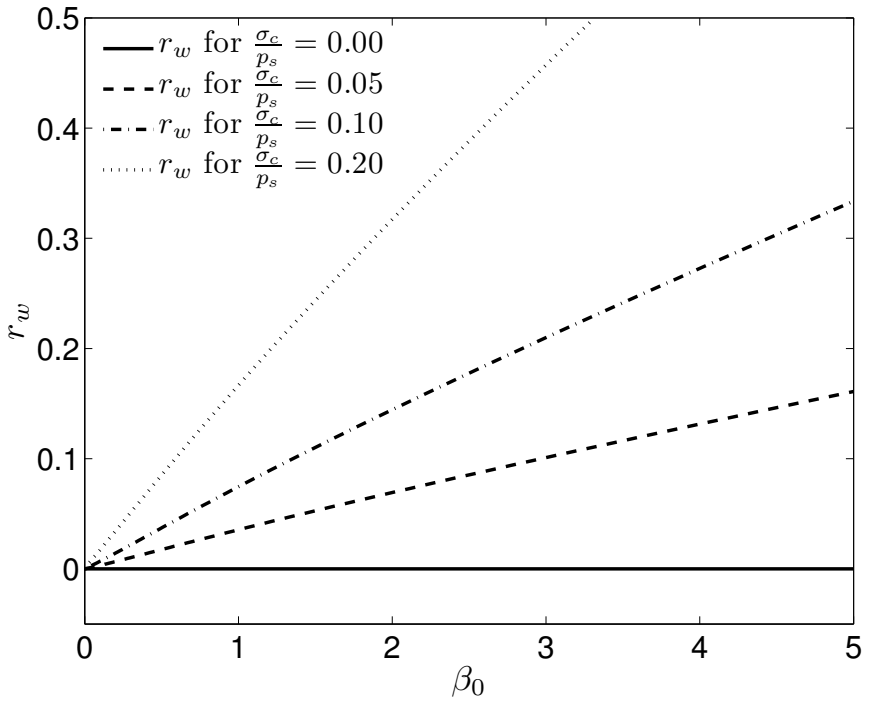

Figure 3-6: The relationship between β_0 and the parameter r_w characterizing the mass of water between the plate and the cavitation point is close to linear and can be approximated as $r_w = 0.71\beta_0\sigma_c/p_s$ [46].

strength of the support σ_c/p_s reduce the time when the plate acquires its maximum velocity, but increase τ_c delaying cavitation further in time. These observations are consistent with the results for a rigid wall ($\sigma_c/p_s \geq 2$) for which $\tau_m = 0$ and $\tau_c = +\infty$.

Hutchinson and Xue [46] suggest a modification of the maximum transmitted impulse that accounts for the effect of cavitation by taking into account the momentum of the mass of fluid between the cavitation point $\chi_c = x_c/at_i$ and the plate. The quantity of water can be characterized by the non-dimensional number

$$r_w = \frac{|x_c|\bar{\rho}}{m_p} = \beta_0|\chi_c|. \tag{3.44}$$

The dependence of this number on β_0 is shown in Figure 3-6. Hutchinson and Xue approximate the dependence as $r_w = 0.71\beta_0\sigma_c/p_s$ [46]. This formula provides a practical way for estimating r_w even though it tends to overestimate r_w for small σ_c/p_s and underestimate it for large σ_c/p_s.

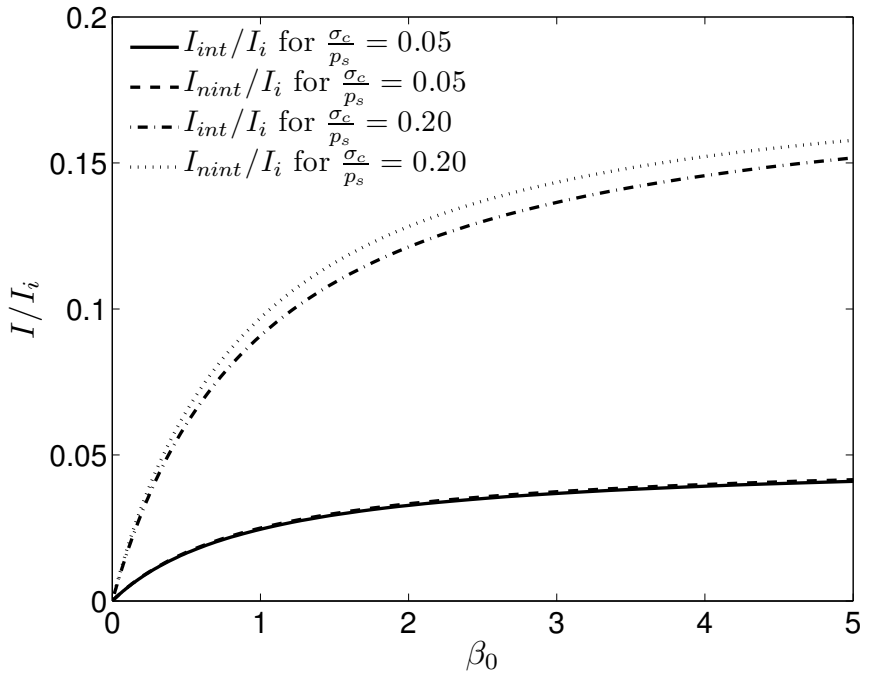

Figure 3-7: The approximation method of Hutchinson and Xue [46] tends to overestimate the exact value of the impulse contained within the liquid layer.

Assuming uniform fluid velocity between $\chi = \chi_c$ and $\chi = 0$ at time $\tau = \tau_c$ and utilizing the parameter r_w, Hutchinson and Xue [46] propose the following formula for the momentum of the fluid:

$$\frac{I_{nint}}{I_i} = \frac{|x_c|\bar{\rho}\dot{\xi}}{p_s t_i} = \frac{r_w}{\beta_0}\frac{a\bar{\rho}\dot{\xi}}{p_s} = \frac{r_w}{\beta_0}\left(\frac{\sigma_c}{p_s}\left(e^{-\beta_0\tau_c}-1\right) + \frac{2\beta_0}{1-\beta_0}\left(e^{-\beta_0\tau_c}-e^{-\tau_c}\right)\right). \quad (3.45)$$

The total momentum $I_{total} = I_p + I_{nint}$ of the water layer and the plate is

$$\frac{I_{total}}{I_i} = \frac{1+r_w}{\beta_0}\left(\frac{\sigma_c}{p_s}\left(e^{-\beta_0\tau_c}-1\right) + \frac{2\beta_0}{1-\beta_0}\left(e^{-\beta_0\tau_c}-e^{-\tau_c}\right)\right), \quad (3.46)$$

which after the substitution of the empirical expression for r_w becomes

$$\frac{I_{total}}{I_i} \approx \left(2 - 4.91\frac{\sigma_c}{p_s}\right)\beta_0^{\frac{\beta_0}{1-\beta_0}} + 1.27\frac{\sigma_c}{p_s}. \quad (3.47)$$

The exact method to find the impulse of the fluid layer would be to integrate the

momentum of each material particle between $\chi = \chi_c$ and $\chi = 0$ at time $\tau = \tau_c$:

$$\frac{I_{int}}{I_i} = \frac{\int_{x_c}^{0} \tilde{u}\bar{\rho}dx}{p_s t_i} = \frac{\int_{\chi_c}^{0} a\bar{\rho}\tilde{u}d\chi}{p_s} = \frac{2}{1-\beta_0}e^{-\tau_c} + \frac{\sigma_c}{p_s}\chi_c - e^{\chi_c - \tau_c} + \left(\frac{\sigma_c}{p_s\beta_0} + \frac{2}{1-\beta_0}\right)\left(e^{-\beta_0(\chi_c+\tau_c)} - e^{-\beta_0\tau_c}\right) - \frac{1+\beta_0}{1-\beta_0}e^{-\chi_c-\tau_c}. \tag{3.48}$$

The approximate method of Hutchinson and Xue [46] tends to overestimate the impulse contained within the liquid layer by a few percent when compared to the exact formula above. The error of the approximate method becomes larger for larger σ_c/p_s (see Figure 3-7).

The impulse given by the formula of Hutchinson and Xue (3.46) is compared to the transmitted impulse from Taylor's analysis (3.28) in Figure 3-8 for two different values of σ_c/p_s. The difference between the two curves is on the order of 10% except for very small values of β_0 for which it can be as large as 100%. The figure also shows the results of two alternative methods to estimate the transmitted impulse. If the fluid layer is considered to be part of the plate then the formulas for the maximum impulse can be applied to this equivalent plate. The effective fluid-structure interaction parameter accounting for both the plate and the cavitated water is

$$\beta_{eff} = \frac{a\bar{\rho}t_i}{m_p + |x_c|\bar{\rho}} = \frac{\beta_0}{1+r_w} \tag{3.49}$$

and can be substituted either in equation (3.28), or in equation (3.40). All four alternative methods for estimation of the transmitted impulse coincide with each other for $\sigma_c/p_s = 0$ and slowly diverge from each other as σ_c/p_s increases (see Figure 3-8). Within the range of practical interest for blasts in water the best approximation to the result of Hutchinson and Xue, equation (3.46), is given by using β_{eff} in equation (3.40): β_{eff} takes into account the added fluid layer and the use of equation (3.40) takes into account the resistance force σ_c.

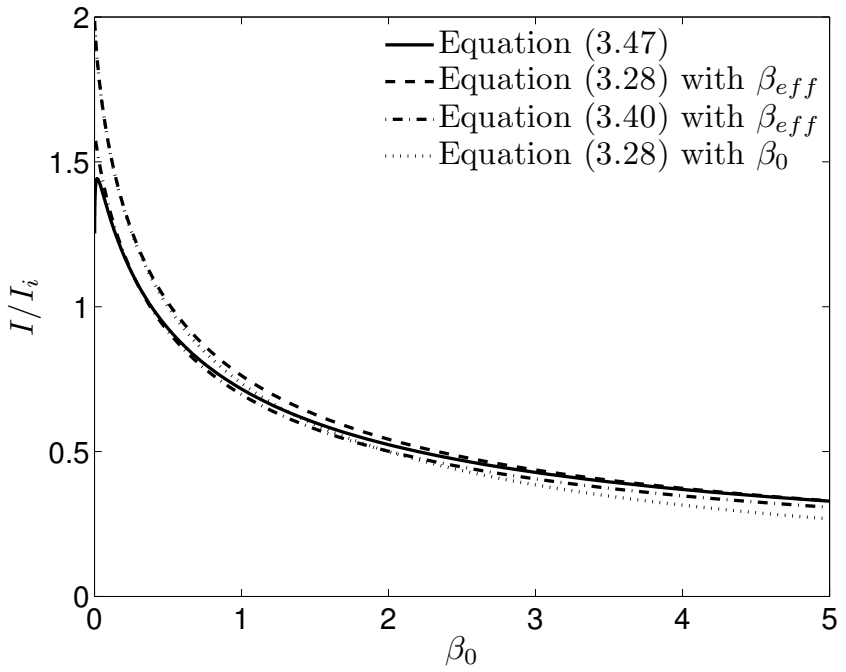

(a) $\sigma_c/p_s = 0.10$

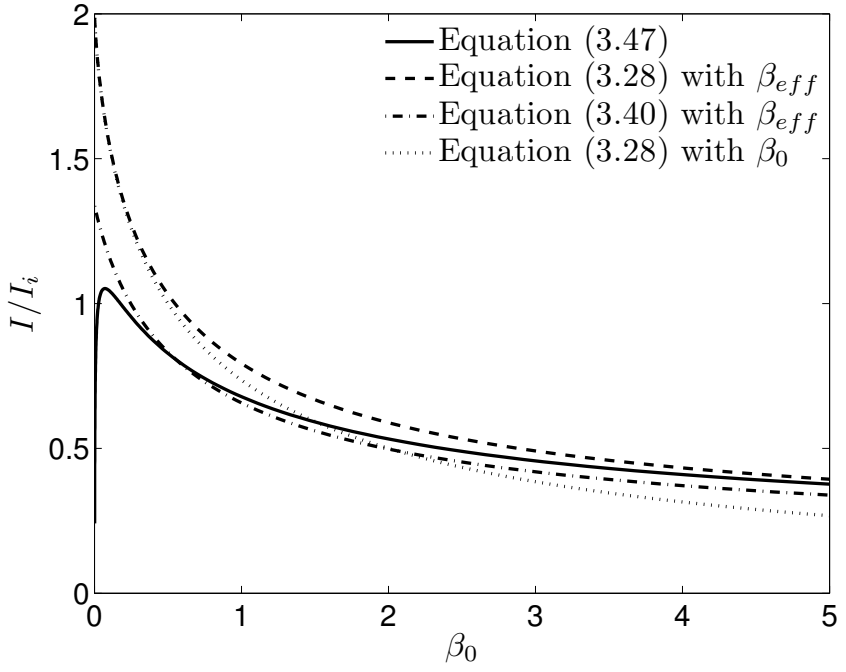

(b) $\sigma_c/p_s = 0.20$

Figure 3-8: A comparison of different approximations of the transmitted impulse for a perfectly plastic resistance force.

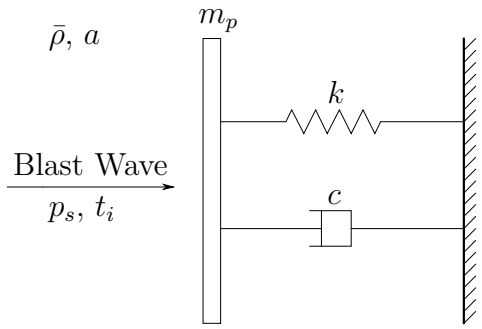

Figure 3-9: A plate of m_p supported by a spring-dashpot system.

3.3.2 Viscoelastic Support

Another case in which an exact solution can be obtained and which may be of practical interest comprises a plate of mass m_p supported by a spring-dashpot system (see Figure 3-9). The need to include the influence of viscoelastic supports in the modeling of idealized blast experiments in a laboratory facility has been recently demonstrated [132].

The resistance force $r(t, \xi, \dot{\xi}, \dots)$ of a viscoelastic support is given by

$$r(t, \xi, \dot{\xi}, \dots) = k\xi + c\dot{\xi}, \tag{3.50}$$

where k and c are the distributed stiffness and the distributed viscosity per unit area, respectively. For an exponential incident wave, the governing equation (3.4) becomes

$$m_p \dddot{\xi} + (a\bar{\rho} + c)\ddot{\xi} + k\dot{\xi} = -2\frac{p_s}{t_i} e^{-\frac{t}{t_i}} \tag{3.51}$$

and its initial conditions are given by (3.9-3.11). This equation can be rewritten in non-dimensional form as

$$\frac{d^3\zeta}{d\tau^3} + \beta_0(1+\alpha)\frac{d^2\zeta}{d\tau^2} + \beta_0\gamma\frac{d\zeta}{d\tau} = -2\beta_0 e^{-\tau}, \tag{3.52}$$

where the stiffness and viscous parts of the resistance force are characterized by the non-dimensional parameters $\gamma = kt_i/a\bar{\rho}$ and $\alpha = c/a\bar{\rho}$, respectively. The initial conditions are given by (3.21-3.23). After one integration this non-dimensional equation

is transformed into

$$\frac{d^2\zeta}{d\tau^2} + \beta_0(1+\alpha)\frac{d\zeta}{d\tau} + \beta_0\gamma\zeta = 2\beta_0 e^{-\tau} \tag{3.53}$$

with zero initial conditions $\zeta(\tau=0)=0$ and $\frac{d\zeta}{d\tau}(\tau=0)=0$. This is the equation of a harmonic oscillator with forcing $2\beta_0 e^{-\tau}$. As it can be seen from the coefficient in front of $\frac{d\zeta}{d\tau}$, there are two contributions to the damping of the oscillator: the contribution of the damper $\beta_0\alpha$ and the contribution of the fluid-structure interaction β_0. The damping ratio $\eta = \frac{(1+\alpha)\sqrt{\beta_0}}{2\sqrt{\gamma}}$ of the system is an increasing function of β_0 implying that larger values of β_0 lead to faster decay of the response, but it is premature to conclude that larger values of β_0 are desirable as the forcing $2\beta_0 e^{-\tau}$ also increases with β_0. The explicit solution of equation (3.53) is

$$\zeta = \frac{2\beta_0}{1-\beta_0(1+\alpha-\gamma)}\left(e^{-\tau} + \frac{1+\lambda_2}{\lambda_1-\lambda_2}e^{\lambda_1\tau} - \frac{1+\lambda_1}{\lambda_1-\lambda_2}e^{\lambda_2\tau}\right) \tag{3.54}$$

where λ_1 and λ_2 are the roots of the characteristic equation

$$\lambda_j^2 + \beta_0(1+\alpha)\lambda_j + \beta_0\gamma = 0, \quad j=1,2. \tag{3.55}$$

Some quantities of interest which follow from the explicit solution (3.54) are:

- the impulse I_p transmitted to the plate

$$\frac{I_p}{I_i} = \frac{m_p\dot{\xi}}{p_s t_i} = \frac{2}{1-\beta_0(1+\alpha-\gamma)}\left(\frac{\lambda_1(1+\lambda_2)}{\lambda_1-\lambda_2}e^{\lambda_1\tau} - \frac{\lambda_2(1+\lambda_1)}{\lambda_1-\lambda_2}e^{\lambda_2\tau} - e^{-\tau}\right) \tag{3.56}$$

- the energy E_p transmitted to the plate

$$\frac{E_p}{E_i} = \frac{\frac{m_p\dot{\xi}^2}{2}}{\frac{p_s^2 t_i}{2a\bar{\rho}}} = \frac{4\beta_0}{\left(1-\beta_0(1+\alpha-\gamma)\right)^2}\left(\frac{\lambda_1(1+\lambda_2)}{\lambda_1-\lambda_2}e^{\lambda_1\tau} - \frac{\lambda_2(1+\lambda_1)}{\lambda_1-\lambda_2}e^{\lambda_2\tau} - e^{-\tau}\right)^2 \tag{3.57}$$

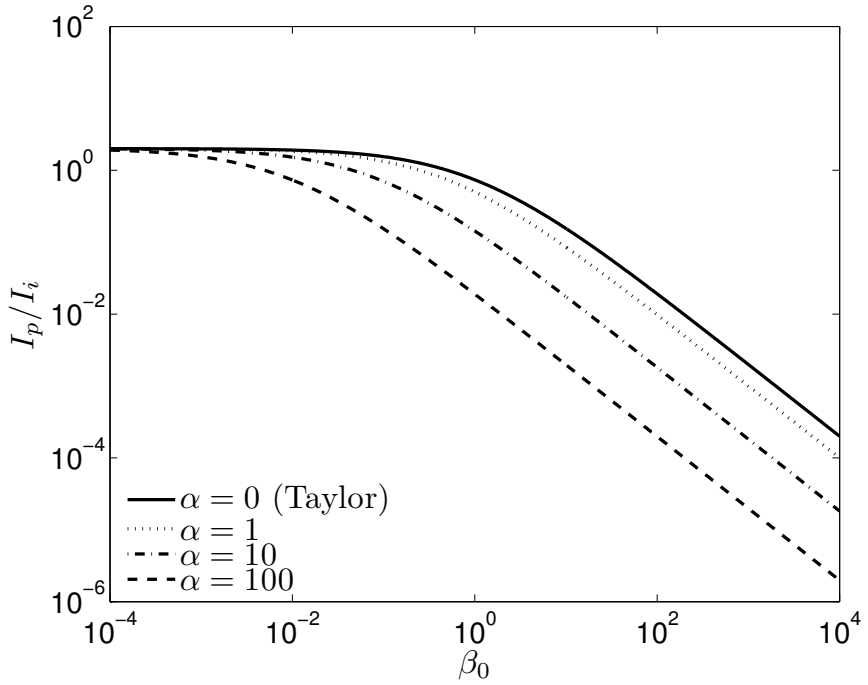

Figure 3-10: Maximum impulse transmitted to the plate as given by equation (3.60) for different values of the parameter α.

- the force $r(t, \xi, \dot{\xi}, \dots)$ exerted on the support

$$\frac{r}{p_s} = \frac{k\xi + c\dot{\xi}}{p_s} = \frac{2\beta_0}{1 - \beta_0(1 + \alpha - \gamma)} \Bigg((\gamma - \alpha)e^{-\tau} + \frac{(\gamma + \alpha\lambda_1)(1 + \lambda_2)}{\lambda_1 - \lambda_2} e^{\lambda_1 \tau} - \frac{(\gamma + \alpha\lambda_2)(1 + \lambda_1)}{\lambda_1 - \lambda_2} e^{\lambda_2 \tau} \Bigg). \tag{3.58}$$

- the total energy E_d dissipated by the damper

$$\frac{E_d}{E_i} = \frac{\int_0^\infty c\dot{\xi}^2 dt}{\frac{p_s^2 t_i}{2a\bar{\rho}}} = \frac{4\alpha\beta_0}{(1 + \alpha)(1 + \beta_0(1 + \alpha + \gamma))} \leq 1. \tag{3.59}$$

For viscoelastic supports, two additional performance metrics are of interest: the total reaction force on the supports and the maximum displacement of the plate. The case of a purely viscous support will be considered first because it allows for explicit expressions for the maxima to be derived. In this case $\gamma = 0$ and one of the two characteristic roots λ_1 and λ_2 becomes 0. The maximum impulse transmitted to the

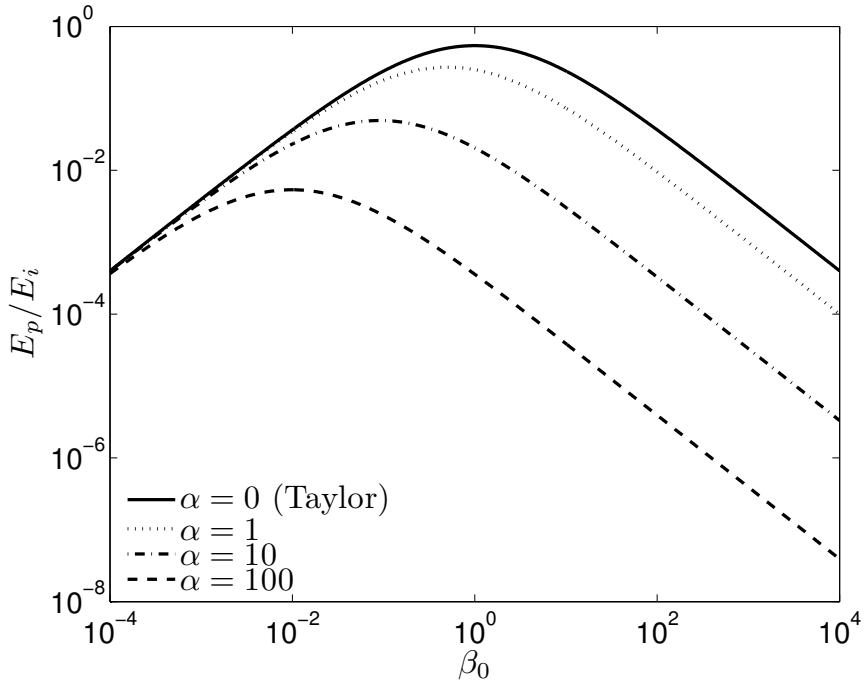

Figure 3-11: Maximum energy transmitted to a plate with purely viscous support.

plate

$$\frac{I_p}{I_i} = 2[\beta_0(1+\alpha)]^{\frac{\beta_0(1+\alpha)}{1-\beta_0(1+\alpha)}} \tag{3.60}$$

is achieved at $\tau_m = \frac{\log((1+\alpha)\beta_0)}{(1+\alpha)\beta_0 - 1}$. This result collapses to the well known result of Taylor [119], equation (3.28), for the case of $\alpha = 0$, as expected. Equation (3.60) can be obtained from Taylor's result by replacing β_0 with $\beta_0(1+\alpha)$ and therefore the effect of large β_0 reducing the transmitted impulse can also be obtained by increasing α. This is illustrated in Figure 3-10 which shows that as α increases the momentum transmission curves shift to the left. A similar shift can be observed for the energy transmission curves in Figure 3-11. The shift to the left of the energy transmission curves is accompanied with a simultaneous shift down because larger values of α lead to larger dissipation in the dashpot and increased energy return into the fluid by the reflected wave.

This maximum force is given by

$$\frac{r}{p_s} = 2\beta_0\alpha[\beta_0(1+\alpha)]^{\frac{\beta_0(1+\alpha)}{1-\beta_0(1+\alpha)}}, \tag{3.61}$$

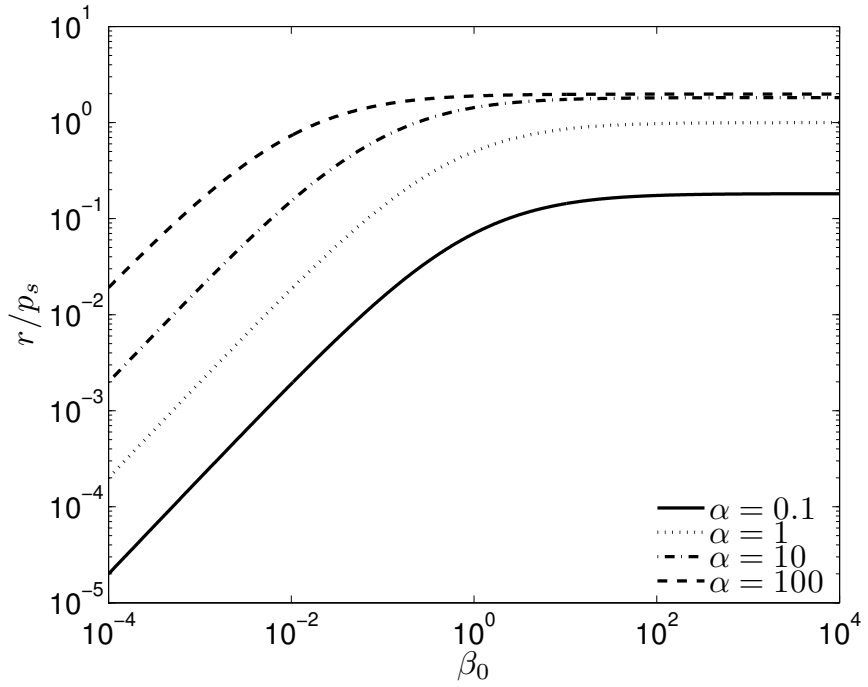

Figure 3-12: Maximum force transmitted to supporting structure as given by equation (3.61) for different values of the parameter α.

and its dependence on β_0 for four different values of α is shown in Figure 3-12. Two conclusions can be drawn from this figure. First, larger values of α lead to larger maximal forces on the supporting structure as the plate moves less and the wave reflection becomes closer to reflection from a rigid wall. Second, for a fixed value of α heavier plates reduce the maximum force by acting as a buffer which first absorbs the impulse of the wave and then slowly transmits it to the supports. These two observations can be better understood after computing the total impulse transmitted to the back wall

$$\frac{\int_0^\infty r dt}{p_s t_i} = \int_0^\infty \alpha \dot{\zeta} d\tau = \frac{2\alpha}{1+\alpha} \tag{3.62}$$

which is an increasing function of α and independent of the fluid-structure interaction parameter β_0. As expected, there is no impulse transmitted to the supports for $\alpha = 0$ and the non-dimensional impulse transmitted to the supporting structure equals 2 for $\alpha = \infty$.

In equations (3.60) and (3.61) the non-dimensional parameter $\alpha = c/\bar{\rho}a$ quantifies the relative strength of the damping due to the dashpot c and the damping due to

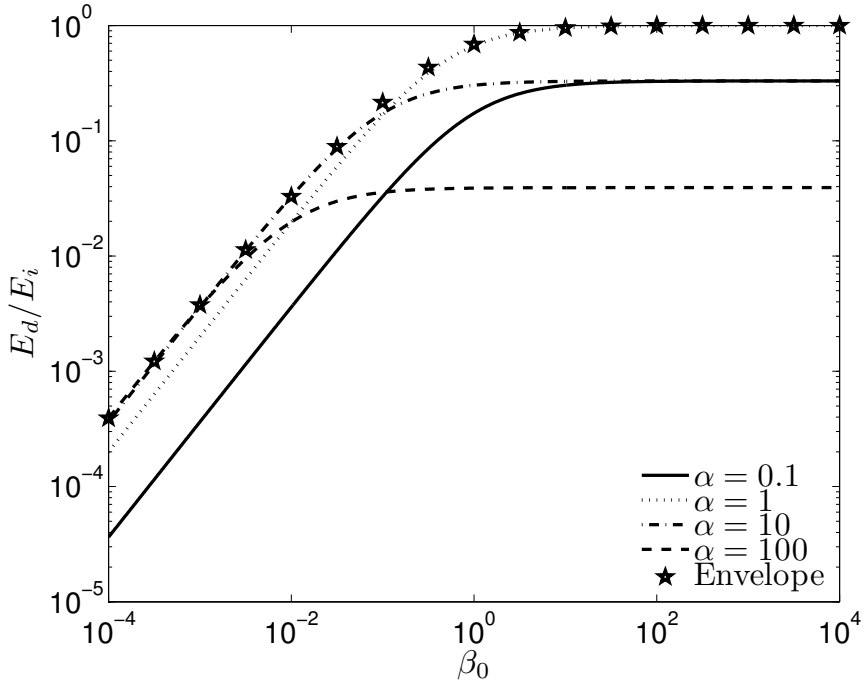

Figure 3-13: Total energy dissipated by the damper c for a purely viscous support as given equation (3.59) for different values of the parameter α.

the fluid $\bar{\rho}a$. Both types of damping have the same effect on the motion of the plate, but their overall effect is different because there is force on the supporting structure due to c, but not due to $\bar{\rho}a$.

The maximum non-dimensional displacement is achieved for $\tau = +\infty$:

$$\zeta = \frac{2}{1+\alpha}. \tag{3.63}$$

For $\alpha = 1$ and a blast with $p_s = 100$ MPa and $t_i = 0.1$ ms in water ($\bar{\rho} = 1000$ kg·m^{-3} and $a = 1475$ m·s^{-1}) this implies that the distance between the plate and the rigid wall must be at least $\xi = 0.0068$ m. The displacement of only 7 mm is an underestimate because, as it will be shown later, cavitation occurs and the damping effect of the water term $a\bar{\rho}$ is lost.

Figure 3-13 displays the energy E_d dissipated by the damper in the case of purely viscous support. The rest of the energy of the incident wave is returned into the fluid by the reflected wave. The figure shows that the dissipated energy fraction E_d/E_i is

largest for large values of β_0 irrespective of the values of the damper constant α. This is consistent with the physical intuition that heavy plates behave similarly to fixed walls for which all of the incoming energy is returned into the fluid by the reflected wave and that light plates absorb significant fraction of the incoming energy returning only a small portion of it into the fluid. It can be observed in Figure 3-13 that the dissipated energy E_d/E_i is not a monotonic function of α for any fixed value of β_0. For a given β_0 the energy dissipation E_d is maximized for $\alpha = \sqrt{\frac{1}{\beta_0} + 1}$. The envelope line

$$\max_{\alpha \geq 0} \left(\frac{E_d}{E_i} \right) = \frac{4\beta_0}{1 + 2\beta_0 + 2\sqrt{\beta_0(1+\beta_0)}} \tag{3.64}$$

bounding the level of dissipation achievable for each value of β_0 is also shown in the figure. Dissipation levels above this line cannot be achieved even for non-zero values of the parameter γ because according to (3.59) E_d/E_i is a decreasing function of γ .

In the general case of non-zero spring parameter γ, the maximum values of expressions (3.54) and (3.56-3.58) cannot be found in a closed form and have to be obtained numerically. The behavior of the maximum impulse I_p transmitted to the plate is shown in Figure 3-14. The symbols represent values obtained with a non-linear optimization code in MATLAB which has been verified against the analytical expression (3.60) represented by the solid line. Two important conclusions can be drawn from this figure. First, as the spring becomes stronger and γ increases, the maximum impulse transmitted to the plate decreases consistent with the stronger constraint imposed on the plate. Second, as the damper becomes stronger and α increases, the curves for the same levels of γ become closer to each other implying a reduction of the effect of γ. In physical terms this means that as the damper becomes stronger the additional effect of the spring becomes less important. For both levels of α shown, the values of the maximum impulse transmitted to the plate are practically independent of γ for $\gamma < 0.2$. Based on Figures 3-10 and 3-14 one can conclude that Taylor's original curve for unsupported plates is a good approximation even for supported plates with $\alpha < 0.1$ and $\gamma < 0.2$ or equivalently $c < 1.475 \times 10^5$ Pa s$\cdot$m^{-1} and $k < 2.950 \times 10^8$ Pa$\cdot$m^{-1} for underwater blasts.

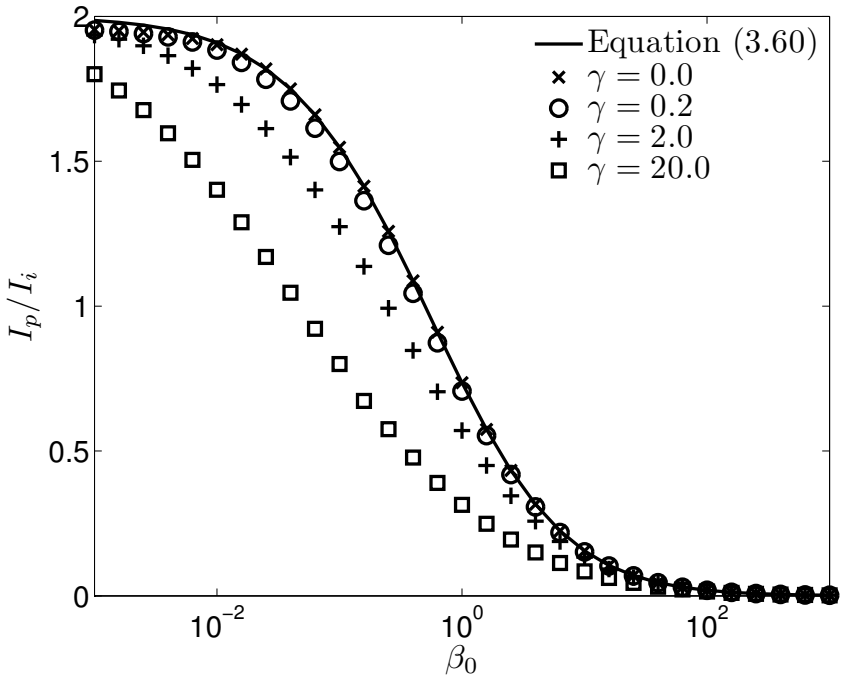

(a) $\alpha = 0.0001$

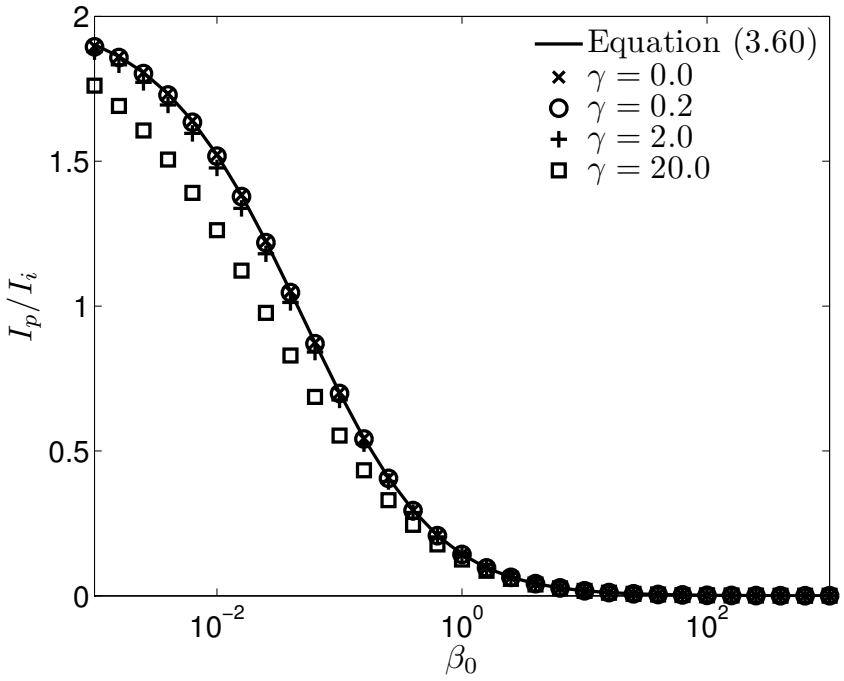

(b) $\alpha = 10$

Figure 3-14: Maximum impulse I_p/I_i transmitted to the plate for two different values of the damper parameter α and various values of γ between 0 and 20. A nonlinear optimization algorithm is used to obtain values represented by the symbols.

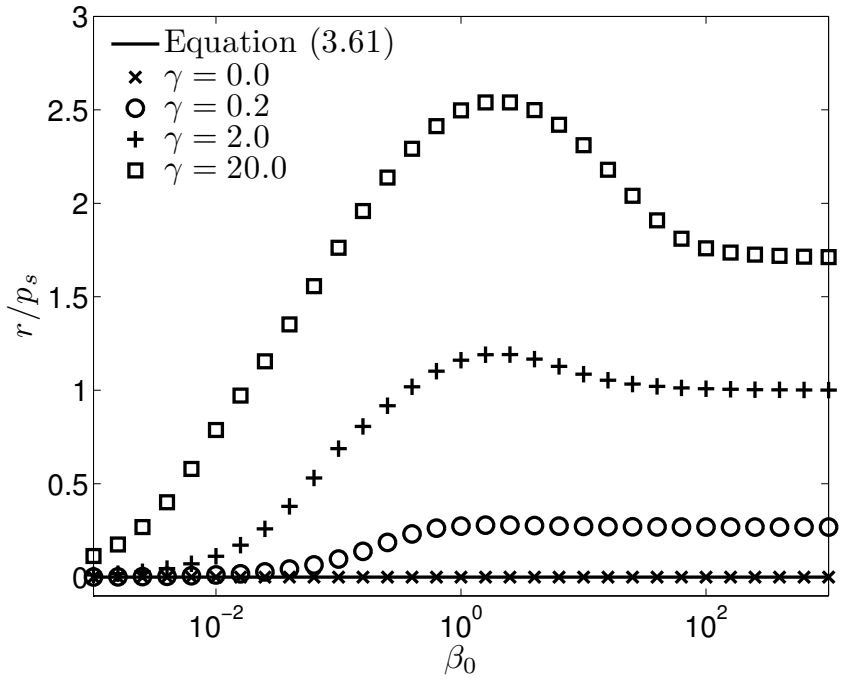

(a) $\alpha = 0.0001$

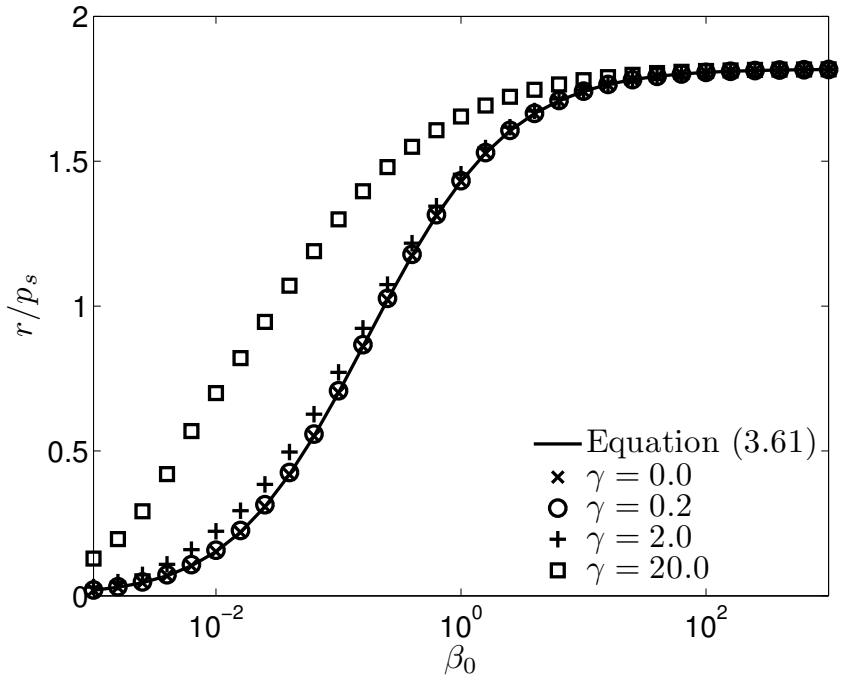

(b) $\alpha = 10$

Figure 3-15: Maximum force r/p_s applied to the supporting structure for two different values of the damper parameter α and various values of γ between 0 and 20. A nonlinear optimization algorithm is used to obtain values represented by the symbols.

The maximum force experienced by the back wall is shown in Figure 3-15 for two different values of the damper constant α. A departure from the typical behavior when a spring is not present is evident in Figure 3-15(a). The curves for large values of the parameter γ cease to be monotonically increasing in β_0, but exhibit a local maximum instead. As the curve for $\gamma = 20.0$ demonstrates, this maximum can exceed the value of 2 corresponding to reflection on a rigid wall. As this maximum lies in the range of β_0 achievable for typical water blasts, it needs to be taken into consideration for structures exploiting the fluid structure interaction effect reducing the momentum transferred to the plate facing the blast. If the structural damping represented by α is increased for constant values of γ the increase in the maximal force transmission disappears because the system becomes overdamped as shown in Figure 3-15(b). For $\alpha = 10$ and the practically achievable range of $\gamma < 2.0$ the curves in the figure coincide for all practical purposes and the maximum force can be well approximated by equation (3.61).

The resonance-like behavior of the system for some values of β_0 is also visible in Figure 3-16 which shows the maximum displacement of the plate. The amplification of the response is present for both $\alpha = 0.0001$ and $\alpha = 10.0$. An important difference between this case and the purely viscous support is that the displacement is dependent on β_0 with it being smaller for smaller values of β_0. A typical dimensional value of the required displacement for underwater blast with $p_s = 100$ MPa, $t_i = 1.0 \times 10^{-3}$ s and a structure with $c = 140$ Pa·s·m^{-1}, $k = 2.8 \times 10^7$ Pa·m^{-1} is $\xi = 0.132$ m.

There are two additional differences between the systems with purely viscous and viscoelastic supports. First, due to the action of the spring, a viscoelastic support always returns the plate to its original position at $\xi = 0$ m, while the deformation is permanent for a purely viscous support. Second, the integral of the force (3.58) transmitted to the supporting structure by a viscoelastic support is always the same:

$$\frac{\int_0^\infty f dt}{p_s t_i} = \int_0^\infty \alpha \dot{\zeta} d\tau = 2, \tag{3.65}$$

while for a purely viscous support it equals $2\alpha/(1+\alpha)$ as given by equation (3.62).

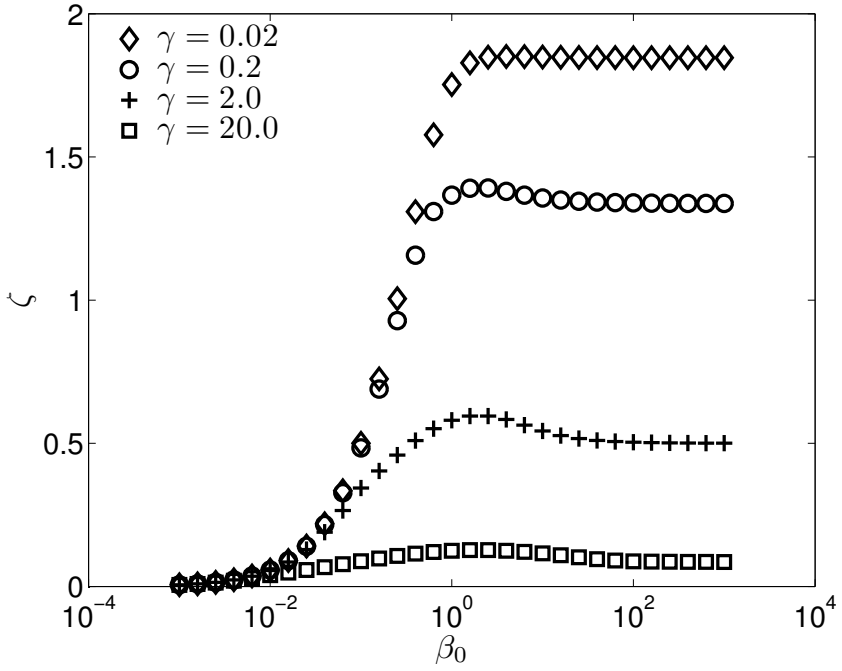

(a) $\alpha = 0.0001$

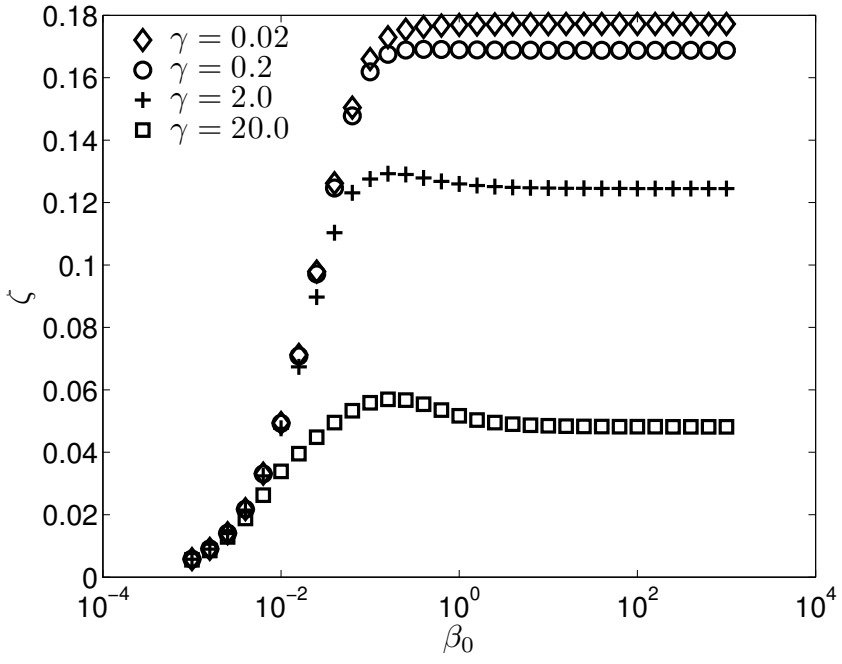

(b) $\alpha = 10$

Figure 3-16: Maximum displacement ζ of the plate for two different values of the damper parameter α and various values of γ between 0.02 and 20.

Equation (3.65) implies that for viscoelastic support the back wall always absorbs the same total impulse independently of the value of β_0.

3.3.3 Supporting Acoustic Medium

There are applications of practical interest such as tankers and petroleum products storage facilities which involve a second fluid behind the plate. The fluid is a wave transmitting medium and the resistance force r it exerts on the plate is wave dependent and therefore unknown. In spite of that, the problem remains tractable because a new equation is available.

Let the plate have thickness D and the transmitted pressure wave into the second fluid be $\check{h}(x - a_r t)$ where a_r is the speed of sound in the second fluid whose density is ρ_r. The equation of motion of the plate becomes

$$m_p \ddot{\xi} = f(\xi - at) + g(\xi + at) - \check{h}(D + \xi - a_r t). \tag{3.66}$$

The momentum conservation equation for the particle to the right of the plate is

$$\rho_r \frac{d^2\xi}{dt^2} = -\frac{\partial p}{\partial x} = -\check{h}'(D + \xi - a_r t), \tag{3.67}$$

while the momentum conservation equation (3.2) for the particle to the left of the plate remains unchanged. These expressions can be simplified by the introduction of $h(x) = \check{h}(x + D)$ eliminating the thickness D from the equations. Differentiation of (3.66) with follow-up elimination of the two unknown waves g and h leads to

$$m\dddot{\xi} + (a\rho + a_r\rho_r)\ddot{\xi} + (\rho - \rho_r)\ddot{\xi}\dot{\xi} = -2af'(\xi - at). \tag{3.68}$$

Elimination of the second order terms leads to a solvable linear equation for ξ

$$m_p\dddot{\xi} + (a\bar{\rho} + a_r\bar{\rho}_r)\ddot{\xi} = -2af'(-at). \tag{3.69}$$

The difference between equations (3.4) for $r = 0$ Pa and (3.69) is a minor one: the

coefficient $a\bar{\rho}$ is replaced by $a\bar{\rho} + a_r\bar{\rho}_r$. Due to this, the solutions of equation (3.69) are the same as those of equation (3.4) for $r = 0$ Pa with the only difference being in the definition of the fluid-structure interaction parameter β_0, which becomes

$$\beta_0 = \frac{(a\bar{\rho} + a_r\bar{\rho}_r)t_i}{m_p}. \tag{3.70}$$

With this new β_0 the non-dimensional governing equation in the case of an exponential incident wave is equation (3.20) with the initial conditions being (3.21-3.23). The non-dimensional displacement has been redefined to $\zeta = (a\bar{\rho} + a_r\bar{\rho}_r)\xi/p_s t_i$. There is no modification in the initial conditions because, due to the screening effect of the plate, the transmitted wave satisfies the property $h(0) = 0$. Using the non-dimensional solution (3.25) and its derivatives, the transmitted and reflected waves can be found to be

$$\frac{h(\tau)}{p_s} = \frac{a_r\bar{\rho}_r}{a\bar{\rho} + a_r\bar{\rho}_r}\frac{d\zeta}{d\tau}(-\tau) = \frac{z}{1+z}\frac{2\beta_0}{1-\beta_0}\left(e^{\beta_0\tau} - e^{\tau}\right),\ \tau \leq 0 \tag{3.71}$$

and

$$\frac{g(\tau)}{p_s} = \frac{1}{1-\beta_0}\left(\left(1 + \beta_0\frac{1-z}{1+z}\right)e^{-\tau} - \frac{2\beta_0}{1+z}e^{-\beta_0\tau}\right),\ \tau \geq 0 \tag{3.72}$$

respectively, where $z = a_r\bar{\rho}_r/a\bar{\rho}$ is the impedance ratio.

The maximum

$$\max_{\tau\leq 0}\left(\frac{h(\tau)}{p_s}\right) = \frac{2z}{1+z}\beta_0^{\frac{1}{1-\beta_0}} \tag{3.73}$$

of the transmitted wave achieved at $\tau = (1 - \beta_0^{-1})\log\beta_0$ might be of interest in some applications. Its dependence on β_0 is shown in Figure 3-17 for three different values of the impedances ratio z. For very light plates ($\beta_0 \gg 1$) the behavior becomes very similar to the behavior of acoustic wave transmission between two different media [133]: for large z the maximum is amplified twice, while for small z the maximum is attenuated by a factor $2z$. The behavior for very heavy plates ($\beta_0 \ll 1$) is significantly different and the maximum is attenuated regardless of the value of z. Heavy plates accelerate slowly regardless of the value of z, store significant fraction of the incoming momentum and then decelerate releasing the momentum into the fluid on the right over long periods of time and at low pressures. This observation can be substantiated

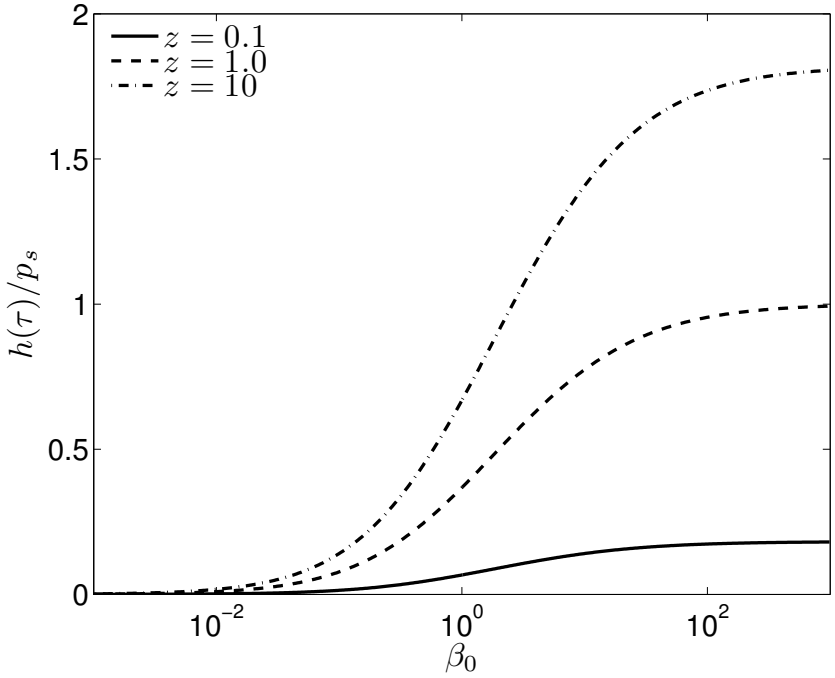

Figure 3-17: Maximum transmitted pressure h/p_s as a function of β_0. Heavy plates (small values of β_0) attenuate the wave regardless of the impedances ratio z.

Table 3.1: Reduction of the maximum transmitted pressure for water medium on both sides ($z = 1$) and steel plates. The assumed density of steel is 7800 kg·m^{-3}.

plate thickness [in]	0.2	0.5	1.0	2.0	5.0	10.0
β_0	7.4450	2.9780	1.4890	0.7445	0.2978	0.1489
$\max_{\tau \le 0} \frac{h(\tau)}{p_s}$	0.7324	0.5760	0.4430	0.3151	0.1782	0.1067

by the fact that the total impulse transmitted into the second fluid is independent of the mass of the plate:

$$\frac{\int_0^\infty h(-\tau)d\tau}{p_s} = \frac{2z}{1+z}, \tag{3.74}$$

and therefore if it is rejected over a longer time period, the process is necessarily completed at lower pressures.

Table 3.1 is an illustration of the achievable reductions in maximum transmitted pressure. The values in the table are computed under the assumption that the liquid on both sides of the plate is water. While the thickest plates provide the largest reductions in the maximum pressure, even relatively thin plates experience some benefits. For example, the one fifth inch thick plate reduces the maximum by 27%

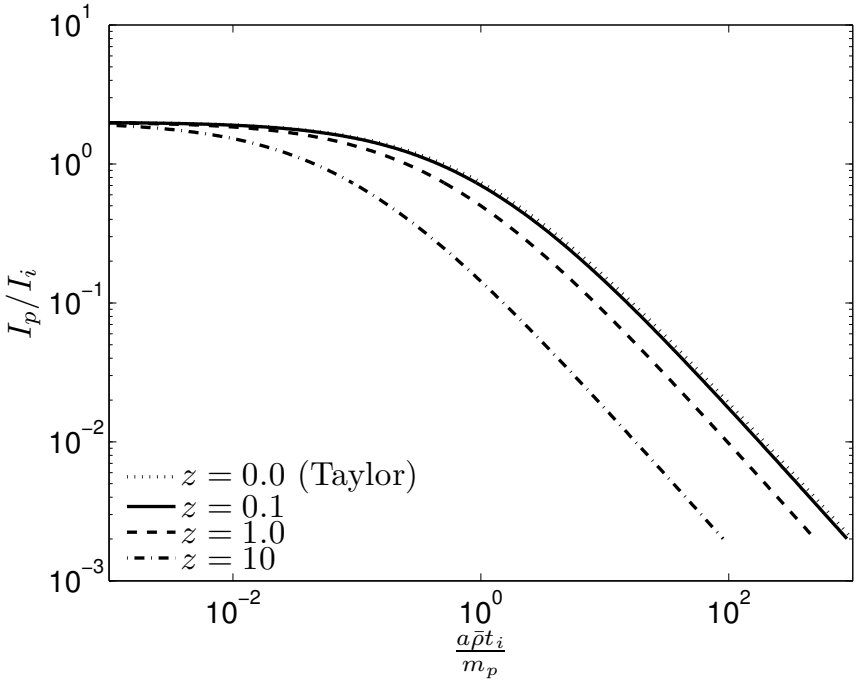

Figure 3-18: Maximum impulse transmitted to the plate versus the original Taylor's fluid-structure interaction parameter $a\bar{\rho}t_i/m_p$. The effect of the second fluid is to shift the curves to the left.

while the ten inch thick plate reduces the maximum by more than 90%.

Even though the governing equation is the same as in the case of a single fluid and the maximum impulse transmitted to the plate is again given by equation (3.28), it is incorrect to conclude that the second fluid has no effect. Figure 3-18 plots the maximum transmitted impulse to the plate against Taylor's original fluid-structure interaction parameter $a\bar{\rho}t_i/m_p$. It can be observed that as the impedance ratio z increases the curves shift to the left, thus reducing the maximum impulse for a fixed value of the original fluid-structure interaction parameter. This trend is caused by the supporting medium which exerts a larger resistance force on the plate and reduces acceleration and velocity of the plate.

The energies contained in the transmitted and reflected waves can also be computed from the exact solution. They are found to be

$$\frac{E_h}{E_i} = \frac{\frac{1}{a_r\bar{\rho}_r}\int_0^\infty h^2(-\tau)d\tau}{\frac{p_s^2 t_i}{2a\bar{\rho}}} = \frac{1}{1+\beta_0}\frac{4\beta_0 z}{(1+z)^2} \tag{3.75}$$

and

$$\frac{E_g}{E_i} = \frac{\frac{1}{a_r \bar{\rho}_r} \int_0^\infty g^2(\tau) d\tau}{\frac{p_s^2 t_i}{2a\bar{\rho}}} = \frac{1}{1+\beta_0} \left(1 + \beta_0 \left(\frac{1-z}{1+z} \right)^2 \right), \tag{3.76}$$

respectively. The expression for the transmitted energy E_h/E_i, equation (3.75), is an increasing function of β_0 implying that the heavier the plate is, the lower the transmitted energy is. This is an important observation because if the energy transmitted into the second fluid has to be dissipated, then heavier plates would reduce the total amount of energy to be dissipated. This reduction in the energy to be dissipated for small β_0 comes together with the similar reduction in the maximum pressure illustrating that there are some benefits to heavier plates, especially given that the total impulse transmitted into the second medium (3.74), as well as the maximum displacement of the plate

$$\frac{a\bar{\rho}\xi}{p_s t_i} = \frac{2}{1+z} \tag{3.77}$$

are independent of the fluid-structure interaction parameter β_0.

Additional insight into the wave reflection and transmission processes can be obtained by looking at the time evolution and the frequency content of the waves. The time history of the three waves, f, g and h, for the case of $z = 1$ and $\beta_0 = 0.5$ is shown in Figure 3-19(a). The curve for the transmitted wave h reveals that the wave amplitude is reduced at the expense of the increased time duration of the wave. The reflected wave pressure g becomes negative shortly after $\tau = 1$ indicating that cavitation does occur in water opening the possibility of significant differences between the real flow and the acoustic solution.

The frequency content of the waves can be found through the application of the Fourier transform, which is defined as [85]

$$\frac{\hat{f}}{p_s t_i}(\Omega) = \int_{-\infty}^{\infty} \frac{f(\tau)}{p_s} e^{-i\Omega\tau} d\tau, \tag{3.78}$$

with its inverse being

$$\frac{f(\tau)}{p_s} = \int_{-\infty}^{\infty} \frac{\hat{f}(\tau)}{p_s t_i} e^{i\tau\Omega} d\Omega. \tag{3.79}$$

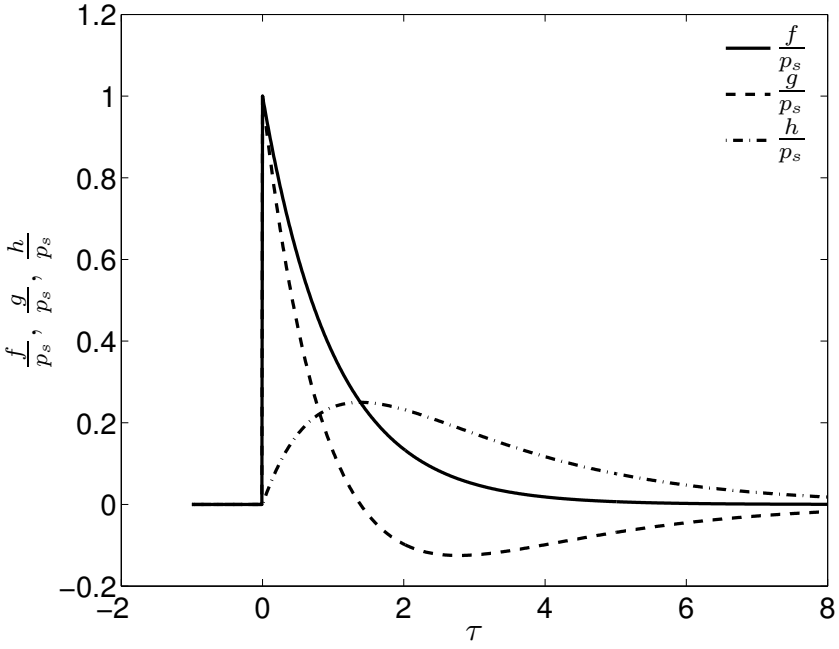

(a) Time evolution

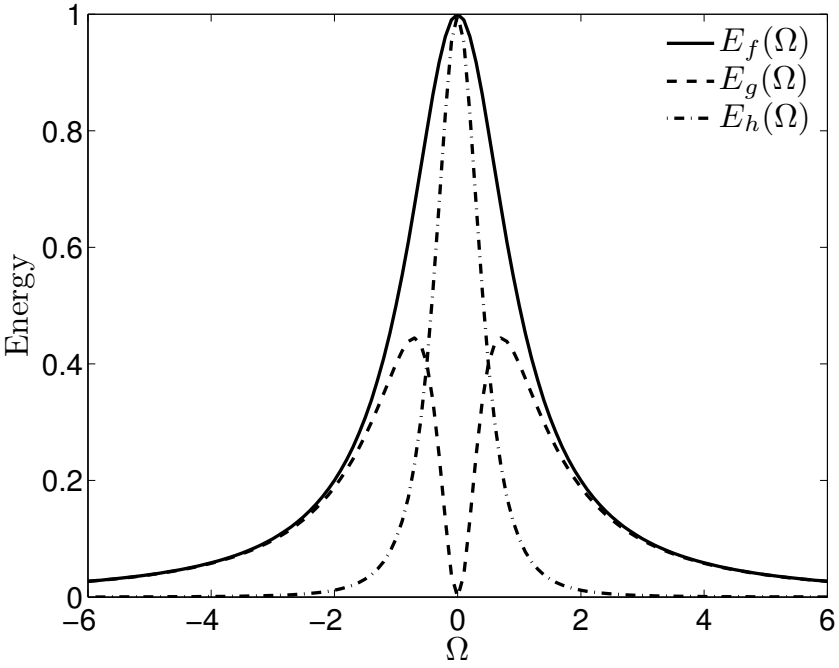

(b) Frequency content

Figure 3-19: Time evolution and frequency content of the incident f, reflected g and transmitted h waves for $z = 1$ and $\beta_0 = 0.5$.

The Fourier transforms of the three waves are found to be

$$\frac{\hat{f}(\Omega)}{p_s t_i} = \frac{1}{1+i\Omega}, \tag{3.80}$$

$$\frac{\hat{g}(\Omega)}{p_s t_i} = \frac{1}{1+i\Omega}\frac{\beta_0\frac{1-z}{1+z}+i\Omega}{\beta_0+i\Omega}, \tag{3.81}$$

and

$$\frac{\hat{h}(\Omega)}{p_s t_i} = \frac{1}{1+i\Omega}\frac{2}{1+z}\frac{\beta_0}{\beta_0+i\Omega}. \tag{3.82}$$

The energy density spectrum of the wave f is defined as

$$S_f(\Omega) = |\hat{f}(\Omega)|^2 = \hat{f}(\Omega)\hat{f}^*(\Omega), \tag{3.83}$$

where the star * denotes complex conjugate. The non-dimensional energy densities of the waves are

$$E_f(\Omega) = S_f(\Omega) = \frac{1}{1+\Omega^2}, \tag{3.84}$$

$$E_g(\Omega) = S_g(\Omega) = \frac{1}{1+\Omega^2}\frac{\beta_0^2\left(\frac{1-z}{1+z}\right)^2+\Omega^2}{\beta_0^2+\Omega^2} \tag{3.85}$$

and

$$E_h(\Omega) = zS_h(\Omega) = \frac{1}{1+\Omega^2}\frac{4z}{(1+z)^2}\frac{\beta_0^2}{\beta_0^2+\Omega^2}. \tag{3.86}$$

The last equation has a factor of z in order to make the non-dimensionalization the same for the fluids on both sides. A plot of the frequency content is shown in Figure 3-19(b). It can be observed that the plate acts as a low pass filter significantly attenuating the high frequencies contained in the incident wave which are present at very low levels in the transmitted wave. The last factor in equation (3.86) $(1+\Omega^2/\beta_0^2)^{-1}$ exhibits quadratic decay in respect to the frequency Ω and reveals that, *ceteris paribus*, heavier plates cause more attenuation of the transmitted wave because

for a wave of a fixed frequency Ω this factor is an increasing function of β_0.

3.4 Response of Actively Deployed Plates

In this section the general solution approach described in Section 3.1 is used to derive a number of relevant cases of acoustic waves interacting with deployable structures.

3.4.1 Active Protection without Detection

Taylor's fluid-structure interaction problem considered in Section 3.2.2 can be extended to the case of a plate moving with velocity $-V$ against the blast wave. As a first approximation, the process by which the plate acquired this velocity and the pressure wave generated by it within the fluid up to the time of impact of the blast wave will be ignored. This may be a good approximation when the impulse $-m_p V$ is imparted to the plate in a time much shorter than the decay time of the incoming wave or the pressure wave generated by the plate motion within the fluid is much weaker than the incident wave.

The motion is still governed by equation (3.20), but the initial conditions are modified and take the form

$$\zeta(\tau = 0) = 0, \tag{3.87}$$

$$\frac{d\zeta}{d\tau}(\tau = 0) = -\delta, \tag{3.88}$$

$$|\zeta(\tau = +\infty)| < +\infty, \tag{3.89}$$

where $\delta = aV\bar{\rho}/p_s$ is an additional non-dimensional parameter of the problem. The last condition arises from the physical requirement that the displacement remains bounded. A similar condition could have been applied to Taylor's original problem which corresponds to $\delta = 0$. The solution of the governing equation is

$$\zeta = \left(\frac{\delta}{\beta_0} - \frac{2}{1-\beta_0}\right) e^{-\beta_0 \tau} + \frac{2\beta_0}{1-\beta_0} e^{-\tau} + 2 - \frac{\delta}{\beta_0} \tag{3.90}$$

with the velocity and acceleration given by

$$\frac{d\zeta}{d\tau} = \left(\frac{2\beta_0}{1-\beta_0} - \delta\right) e^{-\beta_0\tau} - \frac{2\beta_0}{1-\beta_0} e^{-\tau} \tag{3.91}$$

and

$$\frac{d^2\zeta}{d\tau^2} = \beta_0 \left(\delta - \frac{2\beta_0}{1-\beta_0}\right) e^{-\beta_0\tau} + \frac{2\beta_0}{1-\beta_0} e^{-\tau}, \tag{3.92}$$

respectively. Figure 3-20 shows the evolution of the velocity of the plate in the case of small and large values of β_0 for different values of the non-dimensional velocity δ. The effect of the initial plate velocity is to reduce and delay the maximum positive velocity that the plate achieves. This effect is especially strong for heavy plates whose velocity may never become positive for large enough δ. The maximum value of the impulse is achieved when

$$\tau_m = \frac{1}{\beta_0 - 1} \log\left(\beta_0 - \frac{1-\beta_0}{2}\delta\right) \tag{3.93}$$

and is given by

$$\frac{I_p}{I_i} = \frac{1}{\beta_0}\frac{d\zeta}{d\tau}(\tau = \tau_m) = \underbrace{2\beta_0^{\frac{\beta_0}{1-\beta_0}}}_{\text{Taylor's Solution}} \underbrace{\left(1 - \delta\frac{1-\beta_0}{2\beta_0}\right)^{\frac{1}{1-\beta_0}}}_{\text{Reduction Factor}}. \tag{3.94}$$

This extended fluid-structure interaction formula indicates that the maximum momentum transmitted to the plate can be reduced by imparting to the plate an initial momentum toward the blast, i.e. $\delta > 0$. For $\beta_0 > 1$ the maximum impulse is always achieved, whereas for $\beta_0 < 1$ it exists only if δ is small enough, i.e. $\delta < \frac{2\beta_0}{1-\beta_0}$; if $\beta_0 < 1$ and $\delta \geq \frac{2\beta_0}{1-\beta_0}$ the plate never acquires a positive velocity. This is shown in Figure 3-20(b) where for the three cases shown the plate loses its negative velocity within one fifth of the decay time of the incoming wave. For light plates this is not the case because the plate is stopped by the resistance of the fluid to compression rather than by the blast wave and the desired impulse cancellation does not occur. The resistance

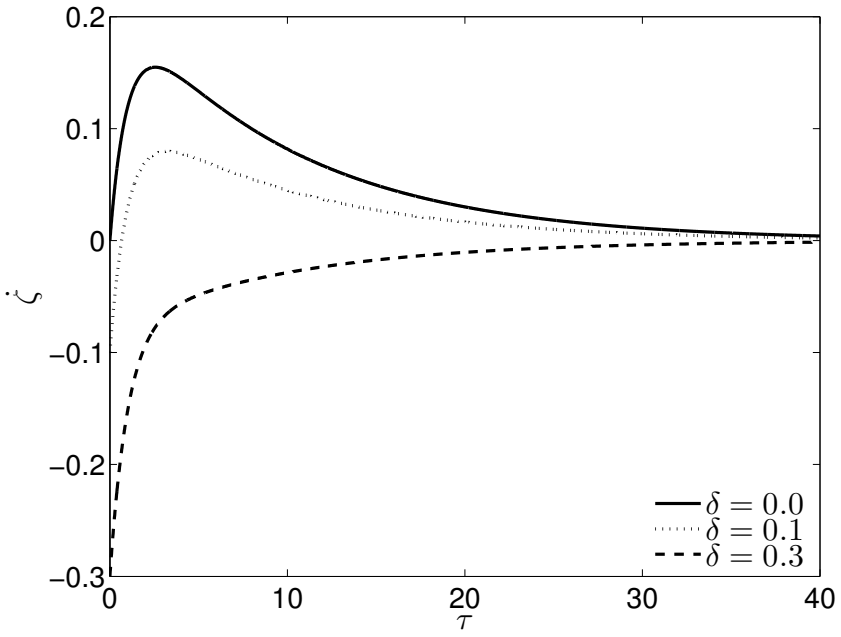

(a) $\beta_0 = 0.1$

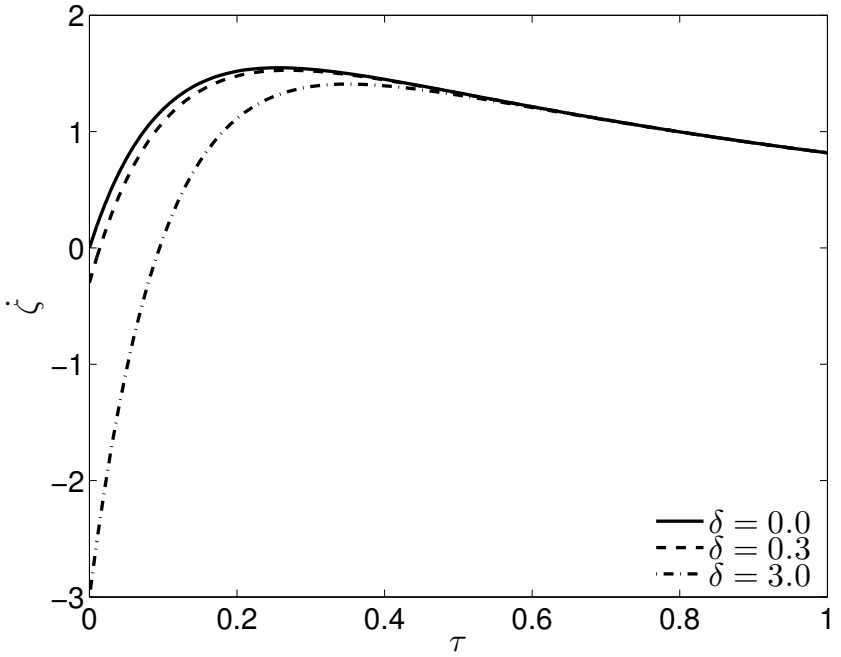

(b) $\beta_0 = 10$

Figure 3-20: Velocity evolution for plates with small and large β_0 and different values of the initial non-dimensional velocity $\delta = aV\bar{\rho}/p_s$.

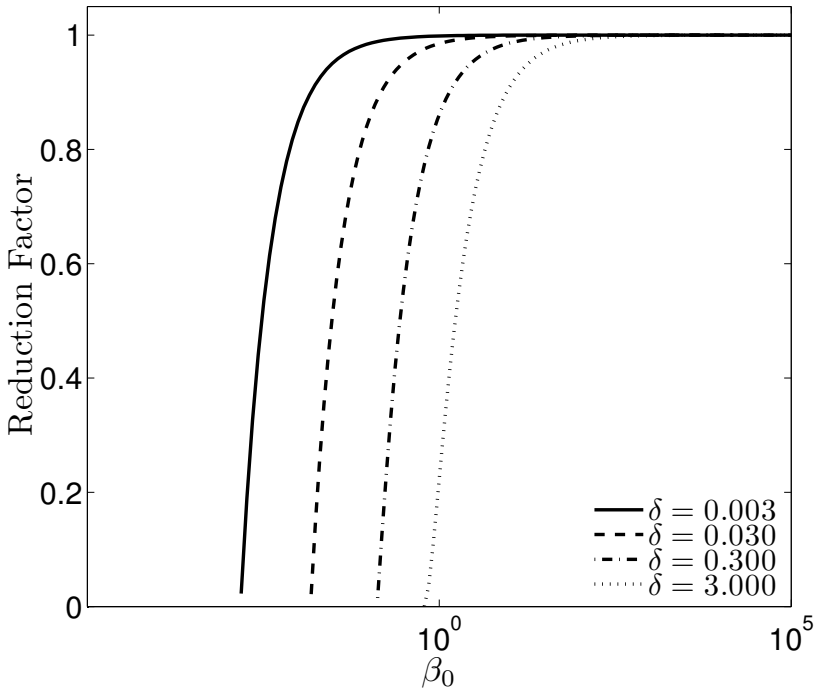

(a) Red. Fact.$= \left(1 - \delta\frac{1-\beta_0}{2\beta_0}\right)^{\frac{1}{1-\beta_0}}$

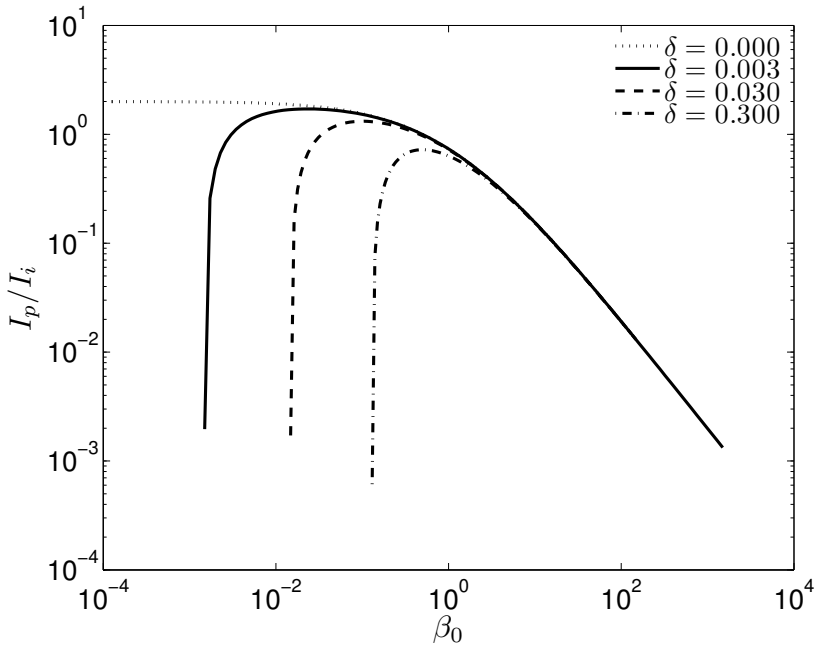

(b) Maximum Momentum

Figure 3-21: Maximum momentum transmitted to the plate according to equation (3.94) for different values of the parameter $\delta = aV\bar{\rho}/p_s$.

Table 3.2: Maximum impulse transmitted to a steel plate with density $\rho_p = 8,000$ kg·m^{-3} for a blast with peak overpressure $p_s = 20$ MPa and decay time $t_i = 0.1$ ms in water ($\bar{\rho} = 1,000$ k·m^{-3} and $a = 1,475$ m·s^{-1}).

		$h_p = 2.0$ in		$h_p = 1.0$ in		$h_p = 0.1$ in	
V [m·s^{-1}]	δ	Red. Fact.	I_p/I_i	Red. Fact.	I_p/I_i	Red. Fact.	I_p/I_i
0.000	0.00	1.0000	1.1424	1.0000	0.8762	1.0000	0.2092
0.429	0.03	0.9568	1.0930	0.9784	0.8573	0.9978	0.2087
4.296	0.30	0.5989	0.6841	0.7982	0.6994	0.9797	0.2050
8.592	0.60	0.2751	0.3142	0.6263	0.5488	0.9620	0.2013

of the fluid to compression also causes the velocity of the plate to decay to zero (see Figure 3-20(a)).

Figure 3-21(a) shows a plot of the momentum reduction relative to Taylor's solution as given by Equation (3.94) achieved for different values of δ. Heavy plates experience large benefits while light plates register no significant improvement over Taylor's solution because for the same δ the heaver plates have significantly larger momenta going against the blast compared to the lighter plates (the proportionality goes as the plate mass for a fixed δ). The maximum impulse transmitted to the plate as a function of the fluid-structure interaction parameter β_0 is shown in Figure 3-21(b) where Taylor's solution ($\delta = 0$) is shown for comparison. As an actual example of the benefits of the initial velocity V for heavy plates, consider three plates of thicknesses $h_p = 2$ in, $h_p = 1$ in and $h_p = 0.1$ in exposed to a blast with peak overpressure $p_s = 20$ MPa and decay time $t_i = 0.1$ ms. The assumed density of steel is $\rho_p = 8,000$ kg·m^{-3} giving fluid-structure interaction parameters $\beta_0 = 0.3445$, $\beta_0 = 0.6890$ and $\beta_0 = 6.8898$, respectively. The values of the reduction factors and the maximum transmitted impulses are given in Table 3.2 for four different values of the imparted velocity V. Velocities V larger than 10 m·s^{-1} were not considered because of the significant practical difficulties in imparting such high velocities to plates in water. For all values of V, the light plate outperforms the two heavier plates significantly in terms of the maximum impulse absorbed by the plate, but the reduction factor ranging from 0.96 to 1.0 reveals that this out-performance is due to the fluid-structure interaction effect, not to the initial velocity V. A very different effect can be seen when the two heavy plates are compared to each other. For an initial

velocity $V = 4.296$ m·s^{-1} the 2 inch plate outperforms the 1 inch plate in terms of I_p/I_i by a small margin and by more than 40% for $V = 8.592$ m·s^{-1}. The superior performance of the heavier plate is solely due to the initial velocity V because for $V = 0.0$ m·s^{-1} 1 inch plate would outperform the 2 inch plate with $I_p/I_i = 0.8762$ versus $I_p/I_i = 1.1424$.

Additional insight into the factors influencing the momentum transmission can be obtained if the performance for the same total forward momentum

$$\eta = \frac{I_f}{I_i} = \frac{V m_p}{p_s t_i} = \frac{\delta}{\beta_0} \tag{3.95}$$

carried by the plate is considered. For the same forward momentum η heavier plates (lower δ) will move slower than lighter plates which will move faster (higher δ). Heavier plates perform better because their lower velocities imply smaller amplitude waves generated into the fluid and less dissipation of the momentum η with a larger fraction of it available for the momentum cancellation taking place within the plate. The variation of the maximum impulse of the plate I_p/I_i with η is shown in Figure 3-22. While all plates benefit from the availability of the forward momentum η, it should be emphasized that the heavy plates benefit the most, Figure 3-22(a).

The reflected wave g is given by

$$\frac{g(\tau)}{p_s} = \left(\delta - \frac{2\beta_0}{1-\beta_0}\right) e^{-\beta_0 \tau} + \frac{1+\beta_0}{1-\beta_0} e^{-\tau}, \tag{3.96}$$

and the expression for the pressure within the fluid domain is

$$\frac{\tilde{p}(\chi,\tau)}{p_s} = e^{\chi-\tau} + \left(\delta - \frac{2\beta_0}{1-\beta_0}\right) e^{-\beta_0(\chi+\tau)} + \frac{1+\beta_0}{1-\beta_0} e^{-\chi-\tau}. \tag{3.97}$$

The cavitation point follows from the conditions $\tilde{p}(\chi_c, \tau_c) = 0$ and $\frac{\partial \tilde{p}(\chi_c,\tau_c)}{\partial \chi} = 0$ which lead to:

$$(\beta_0 - \delta \frac{1-\beta_0}{2}) = e^{(\beta_0 - 1)(\chi_c + \tau_c)}. \tag{3.98}$$

If $\beta_0 \geq 1$ this equation always has a solution for $\chi_c + \tau_c$, but if $\beta_0 < 1$ it has a solution

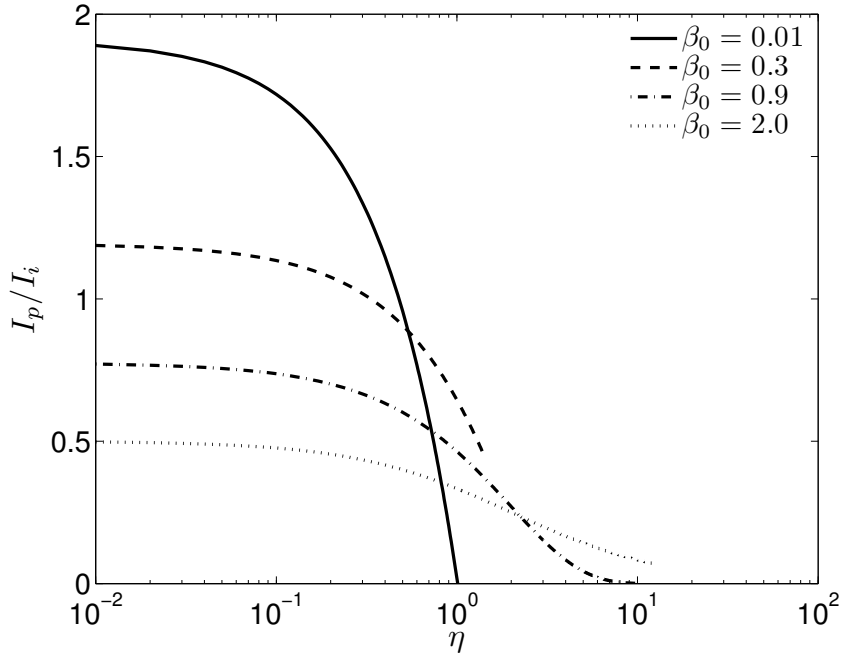

(a) Absolute maximum impulse

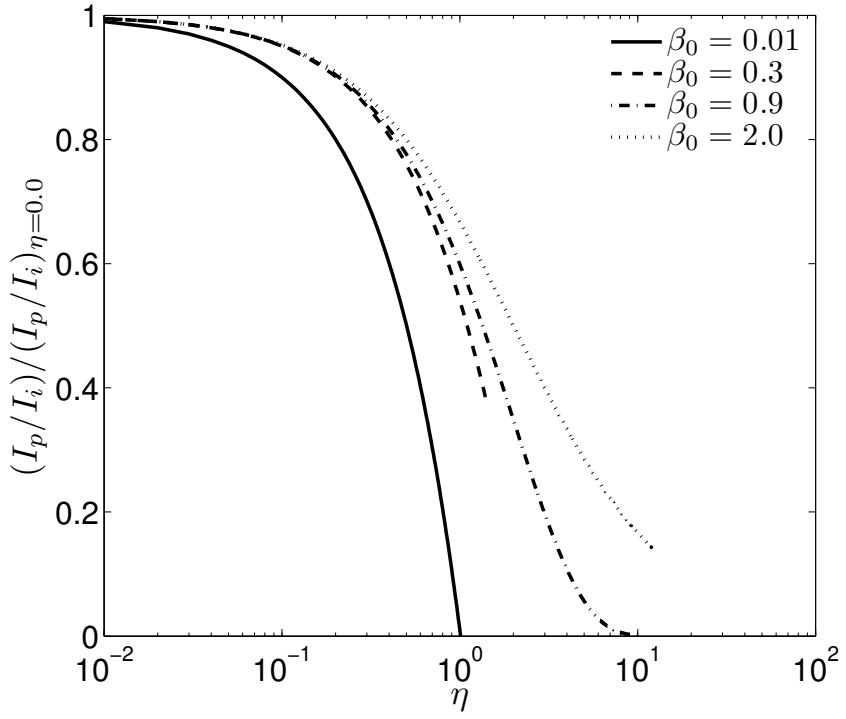

(b) Relative maximum impulse

Figure 3-22: Maximum momentum I_p/I_i versus the parameter η

only when $\delta < \frac{2\beta_0}{1-\beta_0}$. It can be shown that cavitation occurs at $\chi_c = 0$ and $\tau = \tau_m$ just as in Taylor's case. In other words cavitation occurs at the front face of the plate at the instant when the plate has acquired its maximum velocity.

3.4.2 Active Protection with Detection

This section considers the case of the interaction of blast waves with plates deployed by constant actuation pressure. This scenario has been proposed as better model of actively deployable armor than the one considered in the previous section [128]. The deployment must be initiated before the blast wave has reached the plate. The first step of the analysis is to describe the interaction between the actively deployed plate and stationary medium in the absence of blast waves.

Consider the motion of a plate subject to a constant pressure $r(t, \xi, \dot{\xi}, \dots) = -\sigma_c < 0$ acting in the negative x-direction and the pressure wave $g(x + at)$ ensuing in the fluid. The flow can be described by the governing equation (3.8) with initial conditions

$$\xi(t = 0) = 0, \tag{3.99}$$

$$\dot{\xi}(t = 0) = 0, \tag{3.100}$$

and

$$\ddot{\xi} = -\frac{\sigma_c}{m_p}. \tag{3.101}$$

The solution of the system is:

$$\xi = -\frac{\sigma_c m_p}{a^2\bar{\rho}^2} e^{-\frac{a\bar{\rho}t}{m_p}} - \frac{\sigma_c}{a\bar{\rho}} t + \frac{\sigma_c m_p}{a^2\bar{\rho}^2}, \tag{3.102}$$

with

$$\dot{\xi} = \frac{\sigma_c}{a\bar{\rho}} e^{-\frac{a\bar{\rho}t}{m_p}} - \frac{\sigma_c}{a\bar{\rho}}, \tag{3.103}$$

$$\ddot{\xi} = -\frac{\sigma_c}{m_p} e^{-\frac{a\bar{\rho}t}{m_p}}, \tag{3.104}$$

respectively. It is convenient to non-dimensionalize the solution using the parameters p_s and t_i of the blast wave even though this solution is for a problem in which no blast wave is present:

$$\zeta = \frac{\sigma_c}{p_s}\left(-\frac{1}{\beta_0}e^{-\beta_0\tau} - \tau + \frac{1}{\beta_0}\right). \tag{3.105}$$

Equation (3.103) implies that the velocity imparted to the plate cannot be made arbitrary large by detecting the blast wave earlier. The maximum momentum I_d available for impulse cancellation is

$$\frac{I_d}{I_i} = \frac{\sigma_c}{p_s}\frac{1}{\beta_0}. \tag{3.106}$$

Usually $p_s \gg \sigma_c$ implying that the impulse cancellation fraction I_d/I_i is strongly dependent on β_0. More specifically, the cancellation fraction is a decreasing function of β_0 implying that heavier plates achieve better impulse cancellation than lighter ones. However equation (3.106) is only an upper bound of the impulse cancellation and a more precise estimate can be obtained if the time evolution of the momentum of the plate

$$\frac{I_p(\tau)}{I_i} = \frac{|\dot{\xi}|m_p}{p_s t_i} = \frac{\sigma_c}{p_s}\frac{1}{\beta_0}(1 - e^{-\beta_0\tau}) \tag{3.107}$$

is considered. If σ_c, p_s, t_i and the detection time $\tau = \tau_d$ are fixed, expression (3.107) is a decreasing function of β_0 once again implying better impulse cancellation potential for heavier plates[2].

As an indication of the achievable cancellation momentum I_d/I_i for problem parameters representative of air blast, consider a blast of peak overpressure $p_s = 1$ MPa

[2]The derivative with respect to β_0 is

$$\frac{1}{I_i}\frac{\partial I_p(t)}{\partial \beta_0} = \frac{\sigma_c}{p_s}\frac{e}{\beta_0^2}\left[\left(\frac{t}{t_i}\beta_0 + 1\right)e^{-\beta_0\frac{t}{t_i}-1} - e^{-1}\right].$$

The function $\psi(x) = xe^{-x} - e^{-1}$ has a zero at $x = 1$. Its derivative equals to $(1-x)e^{-x}$ which is smaller than 0 for $x > 1$ implying that $\psi(x)$ is decreasing in $(1, +\infty)$. This is enough to conclude that $\psi(x)$ has a maximum at $x = 1$ in $[1, \infty)$. The maximum equals $\psi(1) = 0$ and the derivative $\partial I_p(t)/\partial\beta_0$ is always negative implying that the impulse fraction is a decreasing function of β_0.

and decay time $t_i = 1$ ms which is representative of the blasts generated by improvised explosive devices [106]. A reasonable threshold value of σ_c for human protection is $\bar{p} = 0.3$ MPa and a reasonable value of m_p for body armor in the order of $m_p = 1$ kg·m^{-2} [128]. In air with $\beta_0 = 0.4165$ ($\bar{\rho} = 1.225$ kg·m^{-3}, $a \approx 340$ m·s^{-1} and $t_i = 1.0$ ms) equation (3.106) gives $I_d/I_i = 0.7203$ suggesting significant potential for impulse cancellation. It should be carefully noted that this result ignores the very significant compressibility effects in air considered in Chapter 4.

The solution presented above is now used to solve the coupled fluid-structure interaction problem. The solution approach is based on the superposition of the two acoustic solutions (3.25) and (3.105). Assuming that the blast wave reaches the plate at time $\tau = 0$ and that the deployment mechanism was activated at $-\tau_d = -t_d/t_i$, the velocity of the plate is found to be

$$v_p = \underbrace{\frac{2p_s t_i}{m_p}\frac{1}{1-\beta_0}(-e^{-\frac{t}{t_i}} + e^{-\beta_0\frac{t}{t_i}})}_{\text{Taylor's Solution}} + \underbrace{\frac{\sigma_c t_i}{m_p\beta_0}(e^{-\beta_0\frac{t+t_d}{t_i}} - 1)}_{\text{Deployment Contribution}} \tag{3.108}$$

and its acquired momentum expressed in non-dimensional quantities follows as

$$\frac{I_p(\tau)}{I_i} = -\frac{2}{1-\beta_0}e^{-\tau} + e^{-\beta_0\tau}\left(\frac{2}{1-\beta_0} + \frac{\sigma_c}{p_s}\frac{1}{\beta_0}e^{-\beta_0\tau_d}\right) - \frac{\sigma_c}{p_s}\frac{1}{\beta_0}. \tag{3.109}$$

This function reaches a maximum

$$\frac{I_p}{I_i} = \beta_0^{\frac{\beta_0}{1-\beta_0}} 2^{-\frac{\beta_0}{1-\beta_0}}\left(2 + \frac{\sigma_c}{p_s}\frac{1-\beta_0}{\beta_0}e^{-\beta_0\tau_d}\right)^{\frac{1}{1-\beta_0}} - \frac{\sigma_c}{p_s}\frac{1}{\beta_0} \tag{3.110}$$

at time

$$\tau_m = \frac{1}{\beta_0 - 1}\log\left(\beta_0 + \frac{\sigma_c}{p_s}\frac{1-\beta_0}{2}e^{-\beta_0\tau_d}\right). \tag{3.111}$$

If $\sigma_c/p_s = 0$ the result collapses to the well known result of Taylor (Section 3.2.2). Figure 3-23 shows the effect of σ_c/p_s and t_d/t_i on the maximum transmitted impulse. For a fixed detection time, an increase in the deployment pressure causes a reduction of the transmitted impulse, as shown in Figure 3-23(a). This decrease is significant for heavy plates and negligibly small for light plates. A similar trend is obtained

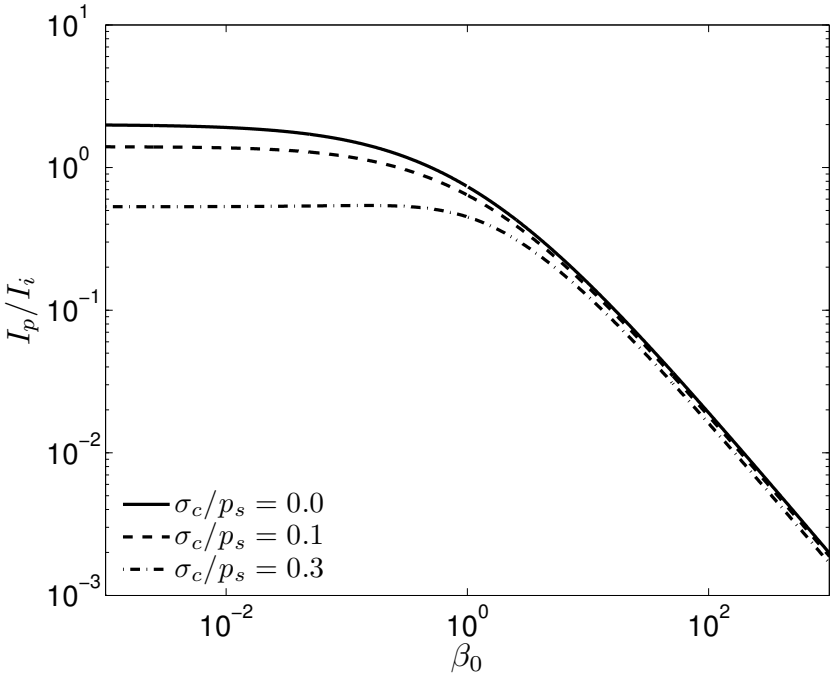

(a) Fixed detection time $\tau_d = t_d/t_i = 2$

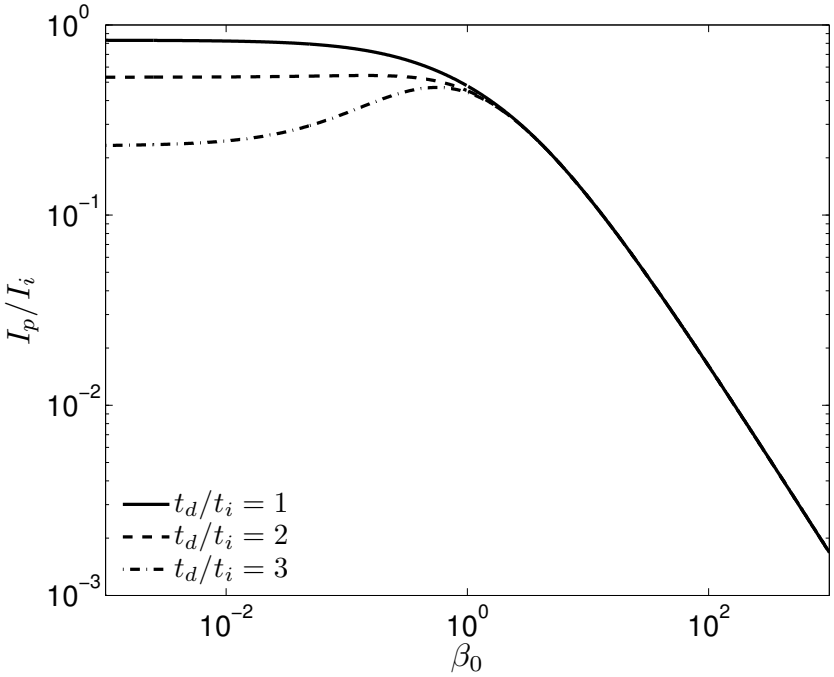

(b) Fixed deployment pressure $\sigma_c/p_s = 0.3$

Figure 3-23: Effect of the deployment pressure σ_c (fixed detection time t_d) and the detection time t_d (fixed deployment pressure σ_c) on the maximum transmitted impulse I_p/I_d.

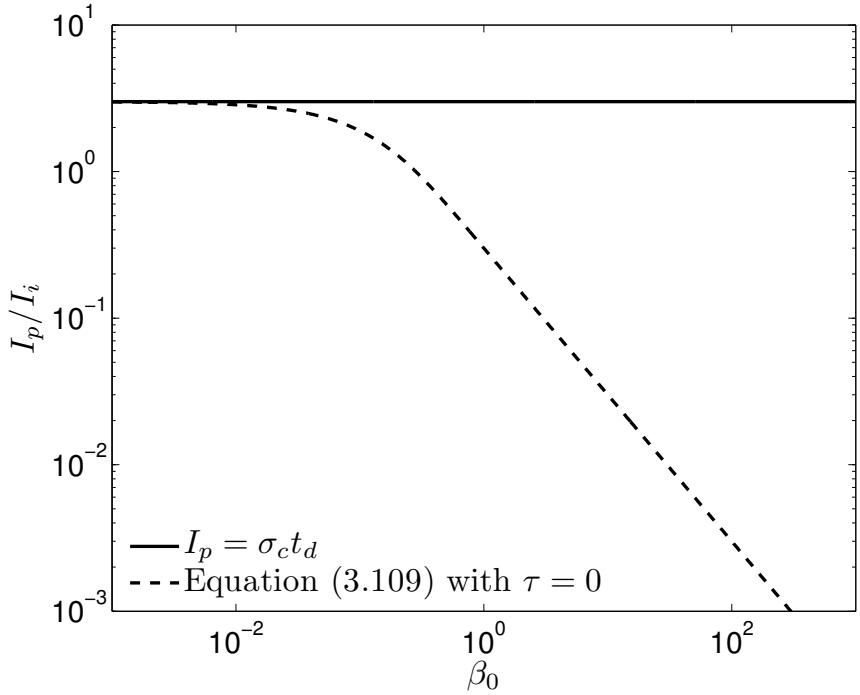

Figure 3-24: Comparison between estimates of the cancellation impulse available at time $t = 0$: the simple one given by $I_d = \sigma_c t_d$ and the one given by equation (3.109)

when the pressure ratio σ_c/p_s is kept constant and the detection time is varied, as shown in Figure 3-23(b). Significant benefits are observed only for heavy plates. The curves have a peak around $\beta_0 = 1$ suggesting that such values should be avoided. The largest benefits of the active mitigation concept are obtained for heavy plates as it was found in the case with imparted forward velocity; the fluid-structure interaction advantages of light plates are so substantial that they render any additional impulse reduction mechanism irrelevant.

The results of this section can be compared with the work of Wadley et al. [128] in which it is assumed that the cancellation impulse at time $t = 0$ is $I_d = \sigma_c t_d$. This assumption is compared to equation (3.109) in Figure 3-24 in which the cancellation impulse is shown as a function of β_0. The assumption closely agrees with the exact solution for small values of β_0, but significantly differs from it for large values of β_0. The constant deployment pressure σ_c accelerates the plate only up to the point at which the same pressure develops in the fluid on the other side of the plate limiting the plate velocity to the fluid particle velocity given by the shock jump relationships.

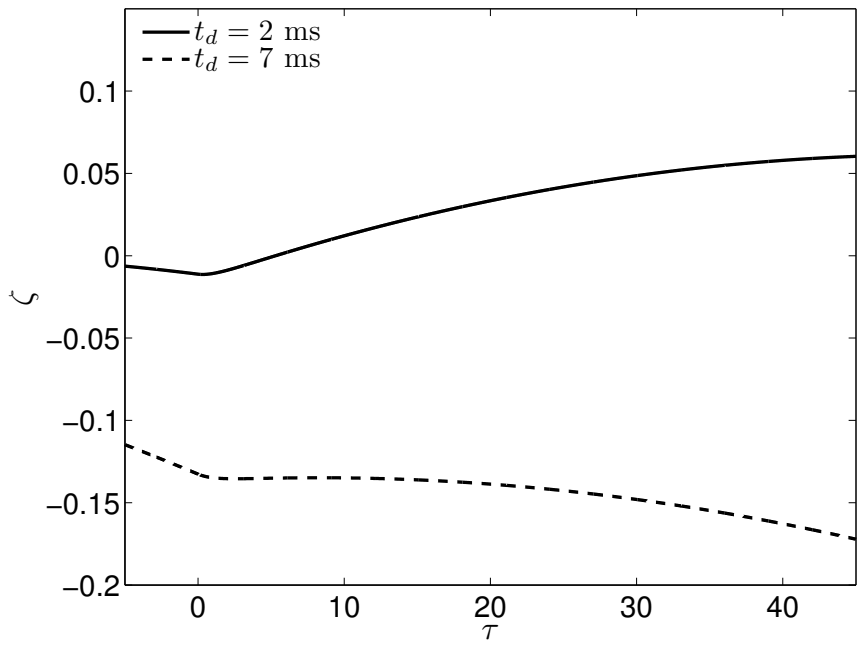

Figure 3-25: Time histories of the displacement for the two different values of t_d (corresponding to 3 m and 6 m explosions of 10 kg of TNT).

Therefore the momentum of the plate becomes proportional to its mass and inversely proportional to β_0. The large difference between the two lines in the figure can lead to serious errors if the simple formula of Wadley et al. [128] is used and cancellation is just assumed to occur.

A stringent metric of the effectiveness of the active deployment concept is to require that the plate remain at $\xi(t) < 0$ m for all times [128]. To investigate the difference of the simplified analysis proposed in [128] with the complete solution above, the non-dimensional displacement

$$\zeta = \begin{cases} \frac{2\beta_0}{1-\beta_0} e^{-\tau} - \frac{2}{1-\beta_0} e^{-\beta_0 \tau} + 2 + \frac{\sigma_c}{p_s} \left(\frac{1}{\beta_0} - \tau - \tau_d - \frac{1}{\beta_0} e^{-\beta_0(\tau+\tau_d)} \right), & \tau \geq 0 \\ \frac{\sigma_c}{p_s} \left(\frac{1}{\beta_0} - \tau - \tau_d - \frac{1}{\beta_0} e^{-\beta_0(\tau+\tau_d)} \right), & -\tau_d \leq \tau \leq 0 \end{cases} \tag{3.112}$$

is needed.

Wadley et al. [128] consider explosions of 10 kg of TNT at 3 m and 6 m from the plate and assumed $t_i = 0.1$ ms. Using the simplified formula $I_d = \sigma_c t_d$ they conclude that an actively deployed plate with $\sigma_c = 0.3$ MPa offers sufficient protection in both

cases because it never returns to its original location. As it can be seen from Figure 3-25 the displacement (3.112) in the first case ($t_d \approx 2$ ms for distance of 3 m) becomes zero at $\tau = 5.306$ and therefore the desired protection is not achieved. For the case of $t_d = 7$ ms (6 m) the displacement never becomes positive confirming the conclusion of Wadley et al. that the plate successfully defeats the blast in this case [128].

There are two compressibility effects which have been ignored in the derivation of the results above. First, the wave generated by the forward motion is not acoustic. It can be shown to be stronger and reduces the total impulse which can be imparted onto the plate before it interacts with the blast wave. Second, the reflection and interaction of the incident blast wave is not acoustic. Due to the compressibility, the pressure amplification is stronger than acoustic (with a factor $C_R > 2$) leading to more momentum being transfered to the plate in the direction of the blast. Theories which account correctly for either of these two effects of compressibility will show reduction in the efficiency of the active protection system.

Chapter 4

Compressibility Effects on Blast Structure Interactions

4.1 The General Solution Method

The analyses in the previous chapter provide significant insights into the interaction of blast waves and structures. However, those analyses were limited to blast waves propagating in fluids in which the effects of compressibility can be ignored, e.g. water. When the blast wave propagates in a highly compressible medium such as air, the analysis must consider the non-linear effects of compressibility, as discussed in Section 2.2.1. It was seen in this discussion that there is a significant departure from the acoustic approximation even for very low intensity waves in air. The purpose of this chapter is to derive basic results of blast-structure interaction incorporating the effects of fluid compressibility, with focus on the impulse transmission from the blast wave to the structure.

The major focus of this chapter is the derivation of practical formulae describing the transmission of impulse from the blast wave to the structure motivated by the need to extend Taylor's basic fluid-structure interaction result into the compressible range. It is expected that due to non-linearities caused by fluid compressibility such formulae will depend on the intensity of the blast in addition to Taylor's fluid-structure interaction parameter representing the relative inertias. Towards this end three cases

are considered. The interaction of uniform shocks with structures is of interest for comparison with shock tube experiments in which blast wave profiling is difficult to achieve. The interaction of exponentially decaying pressure profiles, representative of real blast waves, with structures is analyzed afterwards. The last case considered is a generalization of the formulas for actively deployed plates to compressible media.

The three problems are tackled by a four step approach:

1. Exact asymptotic limits for very light plates are derived.

2. Exact or approximate asymptotic limits for very heavy plates are derived.

3. Numerical simulations for intermediate plate masses are performed.

4. Empirical formulae, matching the two asymptotic limits for light and heavy plates, agreeing closely with the numerical results and collapsing to the acoustic limits for weak pressure waves are proposed.

It will be shown that in the extremely light plate case the only pressure experienced by the plate is the pressure at the blast front and thus is independent of the blast profile. The analysis of the light plate limit is based on the corresponding limit of Taylor's acoustic solution for exponential wave profiles which predicts that as $\beta_0 \to \infty$, the limiting plate velocity (equation (3.26))

$$\lim_{\beta_0 \to \infty} \frac{d\zeta}{d\tau} = 2e^{-\tau} \tag{4.1}$$

attains its maximum at $\tau = 0^+$. A similar result is obtained in the acoustic fluid-structure interaction solution for uniform wave profiles in which case the limiting plate velocity (equation (3.13))is

$$\lim_{\beta_0 \longrightarrow \infty} \frac{d\zeta}{d\tau} = 2 \tag{4.2}$$

for all times including $\tau = 0^+$. In both cases the maximum impulse transmitted to the plate is

$$\frac{I_p}{I_i} = \frac{2}{\beta_0}. \tag{4.3}$$

An important implication of these results is that the specific shape of the incident wave does not affect the response of the plate. Based on this observation, it is sensible to assume that in the non-linear regime the maximum plate velocity is also achieved instantaneously at $\tau = 0^+$. The plate velocity u_p as well as the impulse transmitted to the plate may then be derived by considering the expansion wave produced by a fluid initially compressed at a pressure $C_R p_s$ on a free surface which is initially at rest. Instantaneously upon reflection, the fluid state is characterized by the normal shock reflection on a fixed boundary ($u_p = 0$ m·s^{-1}, $u_r = 0$ m·s^{-1}), independently of the mass of the plate. The reflected state may be expressed in terms of the peak intensity of the blast p_s/p_1 as:

$$p_r = C_R p_s \tag{4.4}$$

$$\begin{aligned}\rho_r &= \rho_s \frac{2\gamma(p_s + p_1) + (\gamma+1)(p_r - p_s)}{2\gamma(p_s + p_1) + (\gamma-1)(p_r - p_s)}, \\ &= \rho_1 \frac{(2\gamma + (\gamma+1)\frac{p_s}{p_1})}{(2\gamma + (\gamma-1)\frac{p_s}{p_1})} \frac{\left(2\gamma + (\gamma - 1 + (\gamma+1)C_R)\frac{p_s}{p_1}\right)}{\left(2\gamma + (\gamma + 1 + (\gamma-1)C_R)\frac{p_s}{p_1}\right)}.\end{aligned} \tag{4.5}$$

Due to its negligible mass, the plate's motion corresponds to a free surface acted upon by fluid in the reflected state on one side and subject to atmospheric pressure on the other side. This results in an expansion wave ($p_e = 0$ Pa) propagating at speed U_e in which the plate velocity matches the fluid particle velocity $u_p = u_e$. These quantities are determined from mass and momentum conservation:

$$\rho_r \left(-U_e\right) = \rho_e \left(u_p - U_e\right), \tag{4.6}$$

$$p_e - p_r = \rho_r \left(-U_e\right)^2 - \rho_e \left(u_p - U_e\right)^2, \tag{4.7}$$

resulting in:

$$u_p^2 = \left(\frac{\rho_r}{\rho_e} - 1\right)\frac{p_r}{\rho_r} = \frac{p_r}{\rho_r}\frac{2\frac{p_r}{p_1}}{2\gamma + (\gamma-1)\frac{p_r}{p_1}} \tag{4.8}$$

where the density in the expansion state ρ_e has been expressed in terms of the reflected density ρ_r using the jump condition (2.40) between the reflected state and

the expansion again. After expressing the reflected properties in terms of their corresponding incident values using (4.4) and (4.5), the following expression of the plate velocity is obtained:

$$u_p = C_R p_s \sqrt{\frac{2}{p_1 \rho_s} \frac{2\gamma + (\gamma + 1 + (\gamma - 1)C_R)\,\frac{p_s}{p_1}}{\left[2\gamma + (\gamma - 1 + (\gamma + 1)C_R)\,\frac{p_s}{p_1}\right]\left[2\gamma + (\gamma - 1)C_R \frac{p_s}{p_1}\right]}}. \tag{4.9}$$

The relative momentum acquired by the plate is:

$$\lim_{m_p \to 0} \frac{I_p}{I_i} = \frac{m_p C_R}{t_i} \sqrt{\frac{2}{p_1 \rho_s} \frac{2\gamma + (\gamma + 1 + (\gamma - 1)C_R)\,\frac{p_s}{p_1}}{\left[2\gamma + (\gamma - 1 + (\gamma + 1)C_R)\,\frac{p_s}{p_1}\right]\left[2\gamma + (\gamma - 1)C_R \frac{p_s}{p_1}\right]}}. \tag{4.10}$$

It is instructive to express the factor $\sqrt{\frac{2}{p_1 \rho_s}}$ in terms of the blast propagation speed using (2.40) and (2.38):

$$\sqrt{\frac{2}{p_1 \rho_s}} = \frac{1}{\rho_s U_s} \frac{(\gamma + 1)\frac{p_s}{p_1} + 2\gamma}{\sqrt{(\gamma - 1)\frac{p_s}{p_1} + 2\gamma}} \tag{4.11}$$

in which case (4.10) may be expressed as:

$$\lim_{m_p \to 0} \frac{I_p}{I_i} = \frac{m_p C_R f_R}{\rho_s U_s t_i} \tag{4.12}$$

where:

$$f_R = \left[(\gamma + 1)\frac{p_s}{p_1} + 2\gamma\right] \times \sqrt{\frac{2\gamma + [\gamma + 1 + (\gamma - 1)C_R]\,\frac{p_s}{p_1}}{\left[(\gamma - 1)\frac{p_s}{p_1} + 2\gamma\right]\left\{2\gamma + [\gamma - 1 + (\gamma + 1)C_R]\,\frac{p_s}{p_1}\right\}\left[2\gamma + (\gamma - 1)C_R \frac{p_s}{p_1}\right]}}. \tag{4.13}$$

Equation (4.12) reveals the important role played by the non-dimensional parameter

$$\beta_s = \frac{t_i}{t_s^*}, \tag{4.14}$$

$$\text{where } t_s^* = \frac{m_p}{\rho_s U_s}, \tag{4.15}$$

in the fluid-structure interaction response of light plates to intense shocks. The parameters t_s^* and β_s are respectively analogous to the acoustic fluid-strcuture interaction time scale t^* and non-dimensional parameter β_0, but represent values affected by the state of compressibility and, thus, by the intensity of the blast. When expressed in terms of β_s, (4.12) reduces to

$$\lim_{m_p \to 0} \frac{I_p}{I_i} = \frac{C_R f_R}{\beta_s} \tag{4.16}$$

which is the final form of the impulse transmitted to the plate in the limit of a very light plate regardless of the specific shape of the pressure profile. It bears emphasis that both β_s and the asymptotic expressions for the transmitted impulse reduce to their corresponding acoustic values for blast intensities of negligible strength, i.e., $p_s \to 0 \Rightarrow (C_R \to 2;\ f_R \to 1;\ U_s \to a_0;\ \rho_s \to \rho_0;\ t_s^* \to m_p \rho_1 a = t_0^*;\ \beta_s \to \beta_0$ and $I_p/I_i \to 2/\beta_0)$, as expected.

The factor f_R in equation (4.16) is specific to air and remains close to one for any value of the overpressure. Its maximum value is 1.26 and occurs for $\frac{p_s}{p_1} \simeq 3.5$, while its limiting value for high overpressures ($p_s/p_1 \to \infty$) is $\sqrt{9/7} = 1.13$

4.2 Response of Unsupported Plates

4.2.1 Uniform Shock Waves in Air

The interaction of uniform shock waves with structures is of interest for comparison with shock tube experiments. The analysis continues with the second step of the four step approach outlines earlier.

The reflection of the uniform shock from a very heavy plate is immediately available from gas dynamics theory. In this case the plate acts as a rigid stationary wall and the pressure on such wall remains constant at all times. The impulse transmitted to the plate is

$$\lim_{m_p \longrightarrow \infty} \frac{I_p}{I_i} = \frac{\int_0^{t_i} p_r dt}{\int_0^{t_i} p_s dt} = \frac{p_r t_i}{p_s t_i} = C_R, \tag{4.17}$$

where the incident impulse I_i has been defined as in Section 3.2.1.

It is useful for the purpose of practical application to devise an expression for the maximum momentum transmission coefficient for arbitrary plate weights and shock intensities. As discussed in [49], the resulting expression should reduce to:

- the acoustic result (3.15) for weak pressure waves,
- the heavy plate response (4.17) for small β_s and arbitrary shock overpressures p_s,
- the light plate response (4.16) for large β_s and arbitrary shock overpressures p_s.

A possible expression satisfying these requirements is

$$\frac{I_p}{C_R I_i} = \frac{1 - e^{-\beta_s / f_R}}{\beta_s / f_R}. \tag{4.18}$$

This formula represents the ratio of momentum acquired by the plate for an arbitrary plate weight and shock intensity and the impulse that would otherwise be transmitted to the plate, should fluid-structure interaction effects be ignored by assuming a rigid wall. It is interesting that in the case of a uniform incident shock, the resulting expression (4.18) collapses into a single curve as a function of the parameter β_s / f_R. The main difference between equation (4.18) and the result presented in Section 4.2.2 is that the expression proposed here is exact in the heavy plate limit, while the expression in the same limit for the exponential profiles is approximate.

Numerical simulations have been used for the purposes of verifying the various results of this analysis as well as the accuracy of the empirical formula (4.18) in the intermediate range of plate masses where exact solutions are not available. A description of the numerical method employed can be found in Appendix B. These consisted of generating uniform shocks of varying intensity by applying a piston velocity at one end of the computational grid, followed by computations of the propagation of the shocks and their reflections on plates of different masses which were modeled as concentrated masses at the opposite end of the computational domain. The transmitted

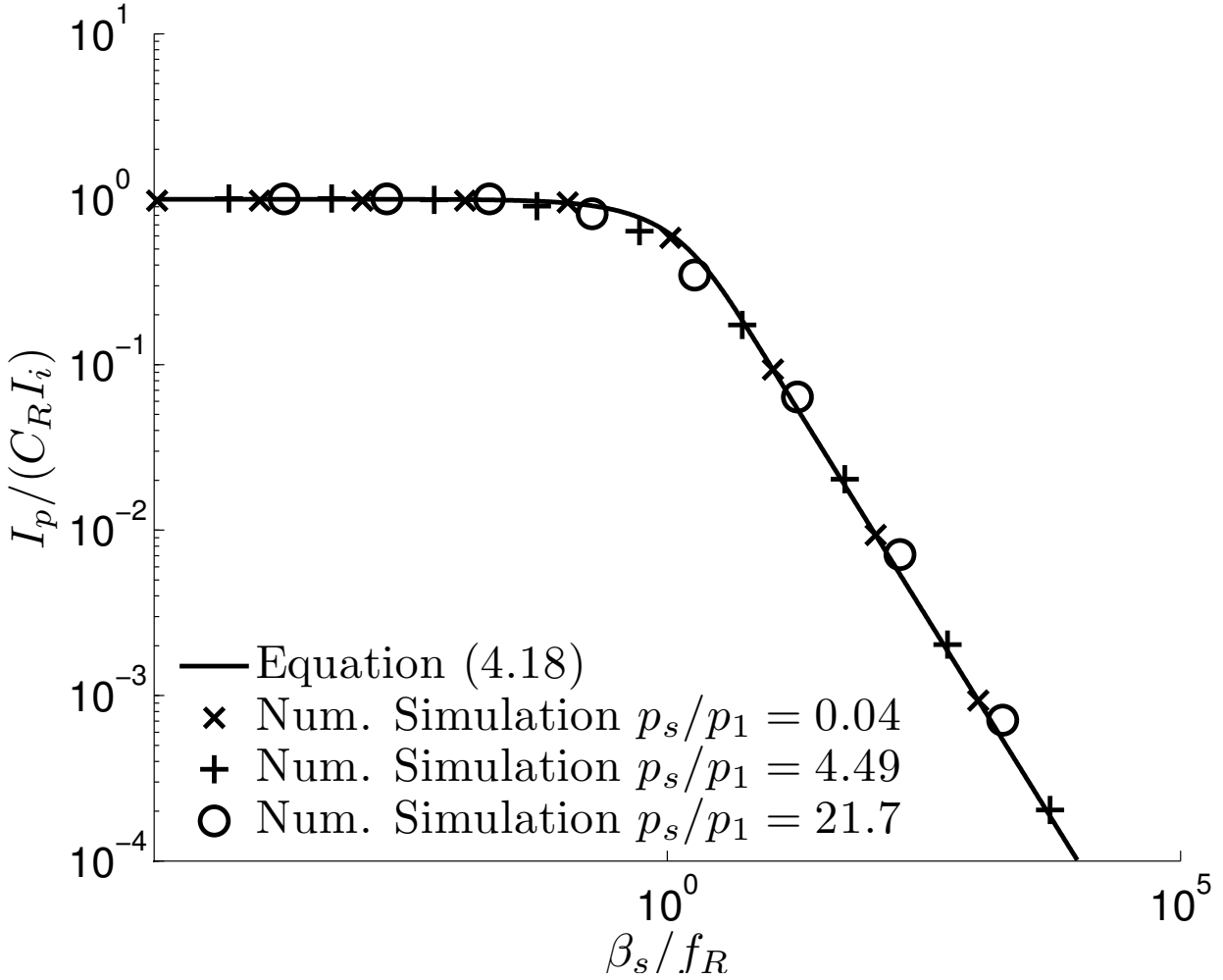

Figure 4-1: Impulse transmission as function of the compressible parameter β_s for different values of the incident overpressure p_s/p_1.

impulse I_p was extracted from the simulations and compared with the predictions of equation (4.18).

The numerical results as well as the comparisons with the theory are shown in Figure 4-1 where the normalized transmitted impulse $I_p/C_R I_i$ versus the combination of parameters β_s/f_R. As it can be seen in this figure, an excellent agreement is found between the numerical results and the theory. Specifically, for $\beta_s \to 0$ the curve becomes horizontal supporting the correctness of the assumption that heavy plates behave as fixed walls and therefore absorb the same impulse independently of the plate mass. For $\beta_s \to \infty$ the curve has slope -1 which is consistent with the assumption that all plates acquire the same maximum velocity (specifically $I_p/I_i \propto m_p$ while $\beta_s \propto 1/m_p$, so that $I_p/I_i \propto 1/\beta_s$). In addition and most importantly, the numerical results support the predictions of the proposed formula (4.18) for the intermediate range of plate masses.

4.2.2 Exponential Shock Waves in Air

The interaction of exponential pressure profiles, representative of blast waves in air, with structures is considered in this section extending Taylor's acoustic results into the compressible range.

In the limit of very heavy plates, $\beta_0 \to 0$, the blast reflection approaches the conditions found for reflection on a fixed wall, i.e., the reflected fluid particle velocity $u_r = 0$ and the instantaneous reflected value of the blast peak overpressure p_r is given by the Rankine-Hugoniot conditions (2.62). Although the solution for the problem of the normal reflection of a blast wave of a general exponential profile,

$$p(t) = p_s e^{-\frac{t}{t_i}}, \tag{4.19}$$

escapes an exact analytic treatment, a working approximation may be obtained by assuming that the reflected pressure profile corresponds to

$$p_r(t) \approx C_R \left(\frac{p(t)}{p_1} \right) p(t) = C_R \left(\frac{p_s}{p_1} e^{-\frac{t}{t_i}} \right) p_s e^{-\frac{t}{t_i}}. \tag{4.20}$$

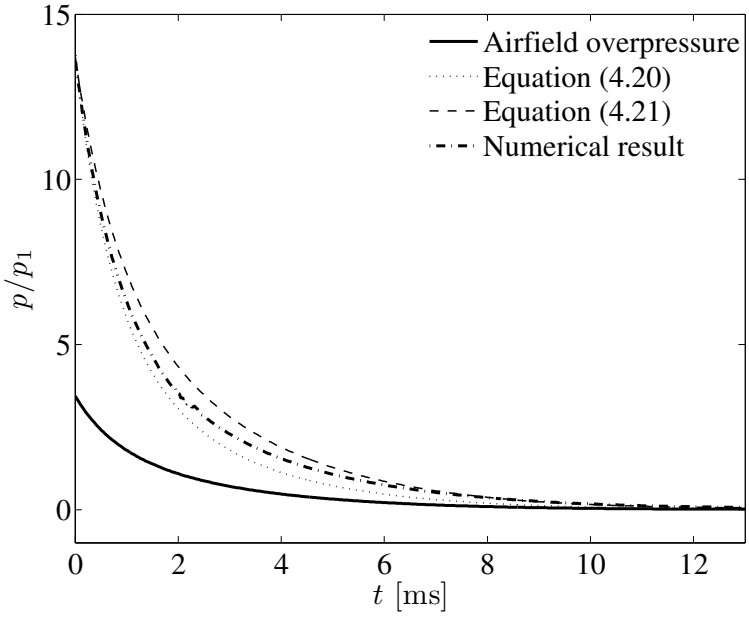

Figure 4-2: Comparison of the reflected pressure profile obtained in the limit of very heavy plates between numerical results and the approximations given by equations (4.20) and (4.21) for $p_s/p_1 = 3.29$

The accuracy of this approximation may be ascertained by comparison with numerical results. In Figures 4-2 and 4-3 the comparison is done for two different blast intensities. In addition, the figures show the pressure profiles obtained by magnifying the incident profile $p(t)$ by a constant reflection coefficient corresponding to the peak incident overpressure, i.e.

$$p_r(t) = C_R \left(\frac{p_s}{p_1} \right) p_s(t) \tag{4.21}$$

It can be concluded from the figures that equation (4.20) provides a more accurate representation of the pressure profiles reflecting from fixed rigid walls, especially at higher blast intensities and at short times after the blast impact. However, it should also be carefully noted that this approximation is a lower bound of the pressure and, thus, of the transmitted impulse.

The approximate impulse acquired by the plate can be computed by time inte-

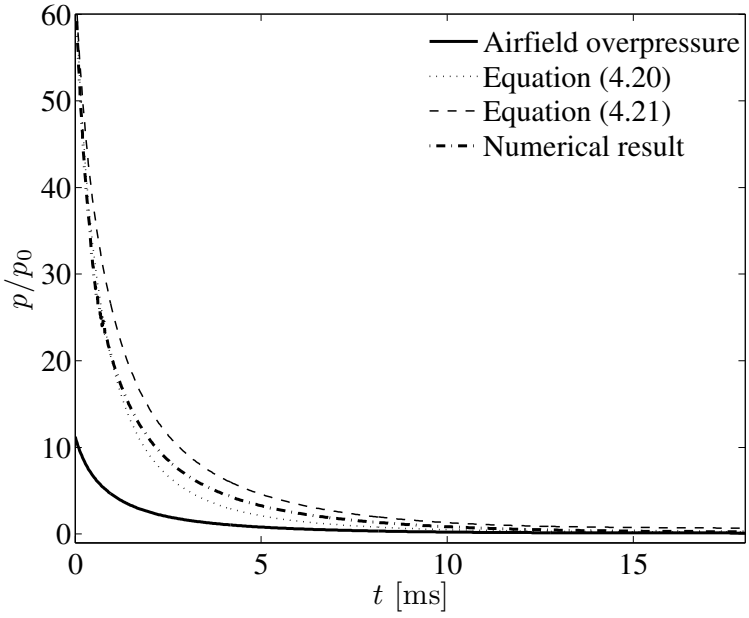

Figure 4-3: Comparison of the reflected pressure profile obtained in the limit of very heavy plates between numerical results and the approximations given by equations (4.20) and (4.21) for $p_s/p_1 = 10.85$

gration of (4.20):

$$\gamma_R = \lim_{m_p \to \infty} \frac{I_p}{I_i} = \frac{1}{t_i} \int_0^\infty C_R e^{-\frac{t}{t_i}} dt \tag{4.22}$$

in which γ_R has been defined as the relative transmitted impulse in the heavy plate limit. In the case of air, the reflection coefficient is defined by equation (2.62) and the value of γ_R can be obtained explicitly as a function of the blast intensity:

$$\gamma_R = \frac{2}{t_i} \int_0^\infty e^{-\frac{t}{t_i}} \frac{4\gamma + (3\gamma - 1)\frac{p_s}{p_1} e^{-\frac{t}{t_i}}}{2\gamma + (\gamma - 1)\frac{p_s}{p_1} e^{-\frac{t}{t_i}}} dt = \frac{3\gamma - 1}{\gamma - 1} - \frac{2\gamma(\gamma + 1)}{(\gamma - 1)^2} \frac{p_1}{p_s} \ln\left(1 + \frac{\gamma - 1}{2\gamma} \frac{p_s}{p_1}\right). \tag{4.23}$$

It follows from this expression that $2 \leq \gamma_R \leq C_R \leq 8$ for air ($\gamma = 1.4$). In the limit of heavy plates the blast pulse delivers all the available momentum (4.23) to the plate and reflects in approximately the same way independently of the plate mass. A comparison between γ_R and C_R is shown in Figure 4-4.

An approximate practical expression of transmitted momentum for arbitrary blast

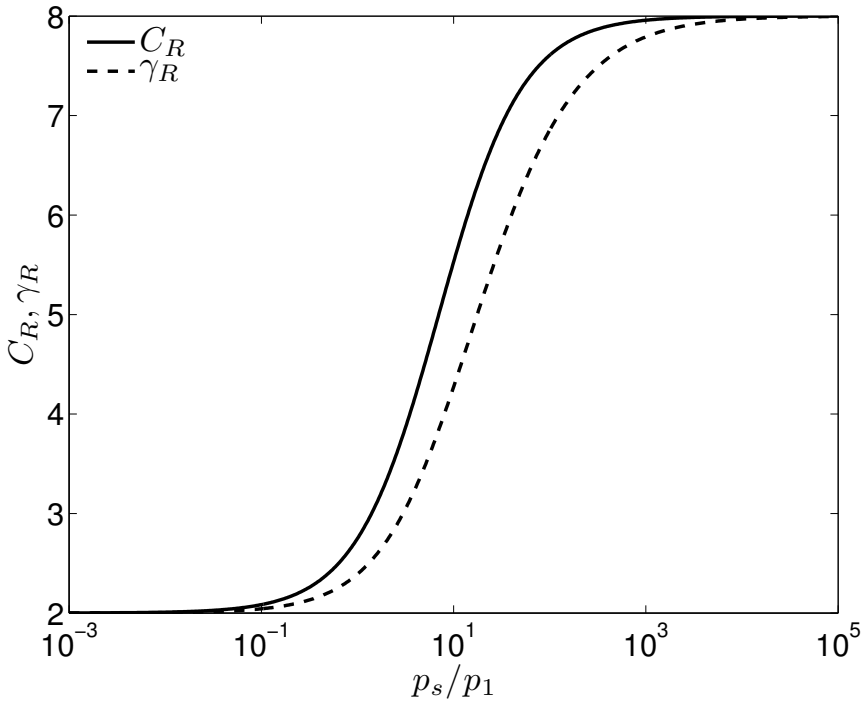

Figure 4-4: The impulse reflection coefficient γ_R, equation (4.23), is an increasing function of p_s/p_1 and has the same limits, but always remains smaller than C_R. Values shown are for air with $\gamma = 1.4$.

intensity and plate mass may be obtained satisfying the following conditions: the exact acoustic result of Taylor (3.28) is recovered for low-intensity blast waves, and the exact asymptotic limits (4.16) and (4.23) are respectively recovered for very light and very heavy plates for arbitrary blast intensities. An expression satisfying these requirements is given in terms of the compressible fluid-structure interaction parameter β_s (4.14), C_R (2.62), γ_R (4.23) and f_R (4.13) by:

$$\frac{I_p}{I_i} = \mathcal{E}(\beta_s, \frac{p_s}{p_1}) = \gamma_R \left(\frac{C_R f_R}{\gamma_R} \right)^{\frac{\beta_s}{1+\beta_s}} \beta_s^{\frac{\beta_s}{1-\beta_s}}. \tag{4.24}$$

Plots of this expression versus β_s in log-log scale are shown in Figure 4-5 for different blast intensities from very low $p_s/p_1 = 0.0167$ to very high $p_s/p_1 = 250$ peak overpressures. Higher overpressure curves almost overlap with the highest overpressure curve shown, as in this case $\gamma_R \simeq C_R \simeq 8$. In practice, all possible air blast fluid-structure interaction curves will lie between the limiting curves shown.

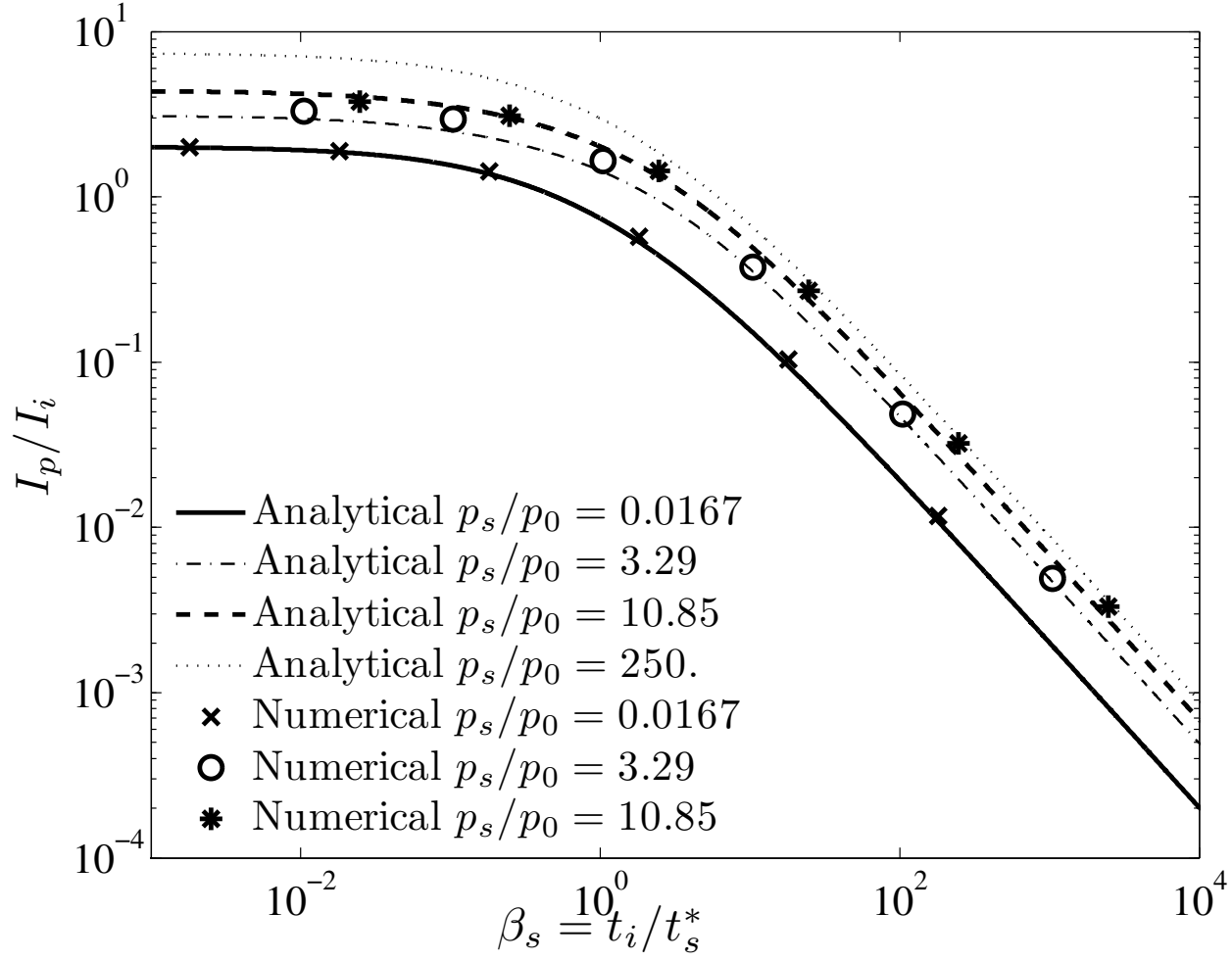

Figure 4-5: Transmitted impulse versus compressible fluid-structure interaction parameter for different blast intensities. Symbols represent numerical results; lines correspond to formula (4.24).

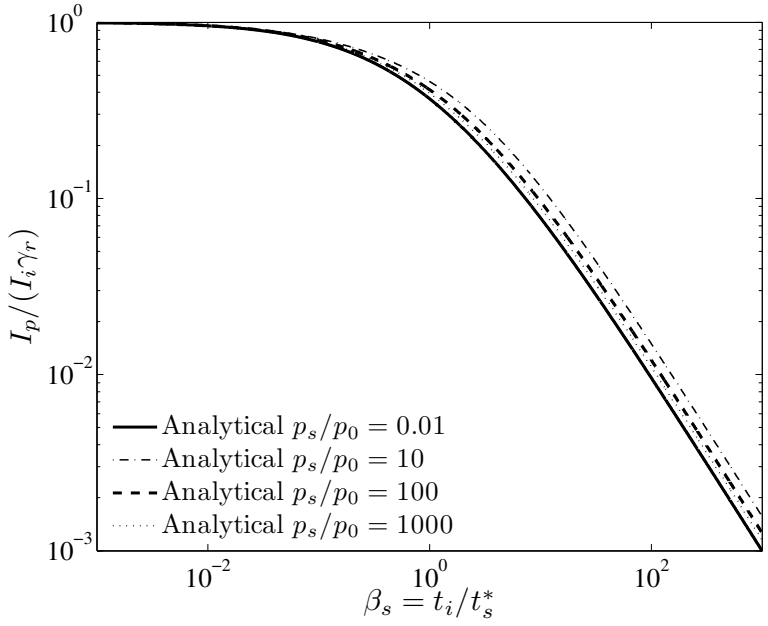

Figure 4-6: Transmitted impulse normalized with that one obtained neglecting fluid-structure interaction effects versus compressible fluid-structure interaction non-dimensional parameter β_s for different blast intensities

Numerical results for blast intensities 0.02, 3.29 and 10.85 and the corresponding curves using equation (4.24) have been added to the figure for the purpose of comparison and verification of the proposed approximate formula. It can be observed that the approximate formula (4.24) accurately matches the numerical results not only in the asymptotic limits but also in the intermediate fluid-structure interaction range where an analytical approximation is not available. These results provide an additional indication that β_s is more relevant than β_0 as a non-dimensional parameter describing fluid-structure interaction in the non-linear range.

Additional insights into the implications of the fluid-structure interaction formula (4.24) may be obtained by normalizing each curve in Figure 4-5 with γ_R, as shown in Figures 4-6 and 4-7. These plots represent the reductions in transmitted impulse relative to the values obtained if fluid-structure interaction effects are neglected. As expected from this study, the reductions are strongly dependent on—and an increasing function of—the blast intensity. It is important to emphasize that impulse reduction for stronger blast waves is achieved not only because the corresponding curve in

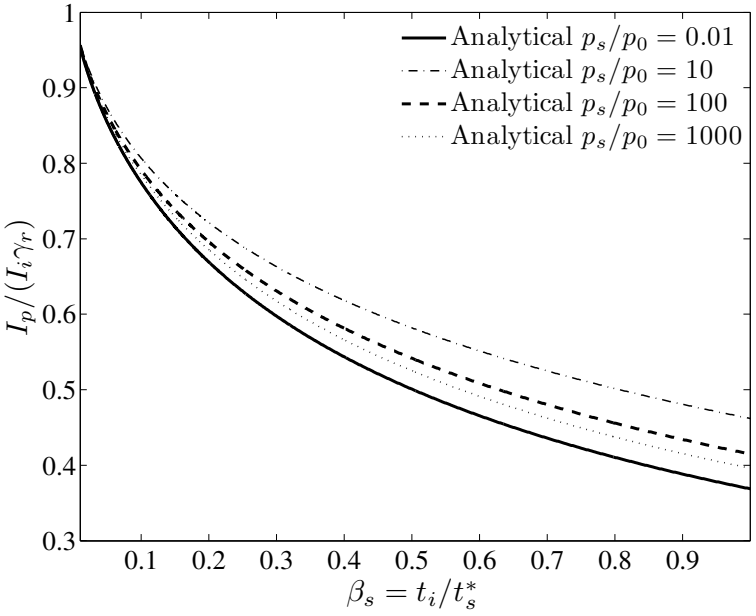

Figure 4-7: Detail of normalized transmitted impulse versus compressible fluid-structure interaction non-dimensional parameter β_s for different blast intensities and small values of β_s

Figure 4-6 will shift to the left, but also because the value of β_s (4.14) will increase. In particular, even in the limit of very high intensities in which both C_R and γ_R tend to the value 8 and a limiting curve is obtained, a further increase of the blast intensity will lead to additional impulse reduction due to β_s which is a monotonically increasing function of the blast front velocity U_s and, thus, of the blast intensity. It may therefore be concluded that the beneficial effects of fluid-structure interaction in the acoustic regime, are exacerbated in the non-linear case.

In order to illustrate the importance of non-linear fluid-structure interaction effects in practical situations, numerical values of representative cases are given in Table 4.1. The examples correspond to 25.4 and 6.35 mm-thick steel plates ($\rho_p = 7800\,\mathrm{kg}\cdot\mathrm{m}^{-3}$) subject to three different peak blast intensities of $0.01, 100$ and $1000\,\mathrm{atm}$, respectively. The decay time t_i is taken equal to 1ms. This value is in accordance with values obtained from experiments [16]. For example, 100 kg of TNT generate an overpressure peak of about 10 atm at a distance of 4.2 m from the source, while the positive overpressure duration is about 1.9 ms. Since the ratio between the decay time and

Table 4.1: Comparison of momentum transmitted by blast waves of different intensities to plates with two different thicknesses according to the proposed fluid-structure interaction formula (4.24) .

Thickness [mm]	p_s/p_1	I_p/I_i	$I_p/\gamma_R I_i$	I_p [Pa·s]
25.4	0.01	1.98	0.99	2
6.35	0.01	1.92	0.96	1.95
25.4	100	5.33	0.78	54051
6.35	100	3.86	0.56	39088
25.4	1000	4.53	0.58	459128
6.35	1000	2.55	0.33	258313

the positive duration is between 1 and 10 [107], one can conclude that a typical decay time is in the range [1ms; 100ms]. The table reports values of I_p/I_i, $I_p/\left(\gamma_R I_i\right)$ and also I_p which give an idea of the absolute magnitude of the transmitted impulse. The low-intensity blast results are shown for the purpose of discouraging an acoustic treatment of fluid-structure interaction effects for intense blasts in air, which predicts unrealistically marginal benefits. In particular, the first two lines of the table show that the reductions for the thick and thin plates are only 1% and 4%, respectively. For a blast intensity of 100 atm, the impulse reduction is 22% for the thick plate and 46% for the thin one. For even stronger intensities of 1000 atm, the reduction is 42% for the thick plate and 67% for the thin one. This suggests that sandwich plate constructions with thin front face sheets may also provide opportunities for blast mitigation in the case of strong air blasts, which somehow clarifies previous understanding [33, 37, 46].

4.2.3 Transmission of "Total" Momentum

In the previous sections it was assumed that the incident wave is characterized by its incident impulse I_i equal to the integral of the wave overpressure. This is a standard assumption which has found a wide spread acceptance amongst the research community [6, 8, 19, 54] because the pressure profile can be easily measured. However, I_i is not the total momentum crossing a fixed location in space because there is additional momentum flux due to the mass flux through that point. For a uniform

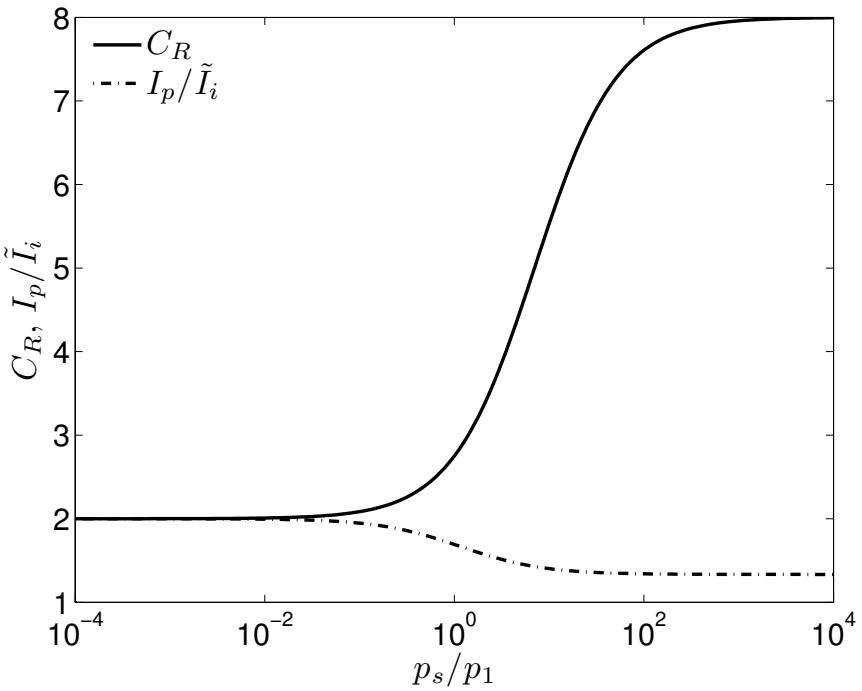

Figure 4-8: Comparison between the reflection coefficient C_R and the momentum transmission for flat profiles. Values given are computed for air with $\gamma = 1.4$.

shock wave, the total momentum crossing a fixed location in space is

$$\tilde{I}_i = (p_s + \rho_s u_s^2) t_i. \tag{4.25}$$

The $\rho_s u_s^2$ term is due to the mass flux $\rho_s u_s$ which carries u_s units of momentum per unit mass (compare to the integral form of the momentum conservation equation (2.10)).

The relationship between the dynamic pressure and the static overpressure is

$$\frac{\rho_s u_s^2}{p_s} = \frac{2\frac{p_s}{p_1}}{(\gamma-1)\frac{p_s}{p_1} + 2\gamma}, \tag{4.26}$$

giving the impulse I_p transmitted to a fixed rigid wall

$$\frac{I_p}{\tilde{I}_i} = \frac{(3\gamma-1)\frac{p_s}{p_1} + 4\gamma}{(\gamma+1)\frac{p_s}{p_1} + 2\gamma} < C_R \tag{4.27}$$

relative to $\tilde{I}_i$ smaller than the pressure reflection coefficient C_R, equation (2.62). The

asymptotic limits for $I_p/\tilde{I}_i$ are 2 for acoustic waves and $\frac{3\gamma-1}{\gamma+1}$ for very strong waves (4/3 for air with $\gamma = 1.4$). A comparison between equation (4.27) and C_R is shown in Figure 4-8.

Expression (4.27) can be interpreted as follows. The speed of the reflected shock wave U_r satisfies

$$\frac{U_r}{u_s} = \frac{(\gamma-1)\frac{p_s}{p_1}+\gamma}{\frac{p_s}{p_1}}. \tag{4.28}$$

The following relationship can be obtained from equations (2.38), (2.39) and (4.28):

$$\frac{U_r+U_s}{U_s} = \frac{(3\gamma-1)\frac{p_s}{p_1}+4\gamma}{(\gamma+1)\frac{p_s}{p_1}+2\gamma} = \frac{I_p}{\tilde{I}_i}. \tag{4.29}$$

For a uniform shock the speed of momentum propagation is shock velocity U_s, therefore the momentum flux across a given location in space is $U_s\hat{I} = U_s\rho_s u_s = p_s + \rho_s u_s^2$. The volume between the reflected shock and the plate is increasing with time, but the total momentum in it remains equal to zero at all times. The momentum flux in this volume is $(U_s + U_r)\hat{I}$ where the term containing U_r must be added because the boundary of the volume is advancing against the incoming momentum flux with speed U_r. Given that the total momentum in the volume is zero at all times, all the incoming momentum has to be transmitted to the right boundary of the volume and therefore equals to the momentum transmitted to the plate I_p.

If the expression for the impulse in (4.24) is non-dimensionalized with $\tilde{I}_i$ instead of I_i, a somewhat simpler expression for the correction factor f_R can be obtained. Using the alternative expression for the instantaneous plate velocity in the light plate limit

$$u_p = \frac{C_R p_s}{\rho_s U_s}\sqrt{\frac{(\gamma+1)\frac{p_s}{p_1}+2\gamma}{(\gamma-1)\frac{p_r}{p_1}+2\gamma}}\sqrt{\frac{(\gamma+1)\frac{p_s}{p_1}+2\gamma}{(\gamma-1)\frac{p_s}{p_1}+2\gamma}}\sqrt{\frac{(\gamma-1)\frac{p_s}{p_1}+\gamma}{\gamma\frac{p_s}{p_1}+\gamma}}, \tag{4.30}$$

the impulse transmitted to the plate becomes

$$\frac{I_p}{\tilde{I}_i} = \frac{m_p}{\rho_s U_s t_i}C_R\sqrt{\frac{(\gamma-1)\frac{p_s}{p_1}+2\gamma}{(\gamma-1)\frac{p_r}{p_1}+2\gamma}}\sqrt{\frac{(\gamma-1)\frac{p_s}{p_1}+\gamma}{\gamma\frac{p_s}{p_1}+\gamma}}, \tag{4.31}$$

which can be rewritten as

$$\frac{I_p}{\tilde{I}_i} = \underbrace{\frac{m_p}{\sqrt{\rho_s \rho_r} U_s t_i}}_{\text{new } \beta_s} C_R \underbrace{\sqrt{\frac{(\gamma-1)\frac{p_s}{p_1} + 2\gamma}{(\gamma-1)\frac{p_r}{p_1} + 2\gamma}}}_{\text{new } f_R}. \tag{4.32}$$

Equations (4.18) and (4.24) can be renormalized with respect to the "total" impulse $\tilde{I}_i$. The renormalization can be accomplished either by following the approach of Sections 4.2.1 and 4.2.2, or by establishing the relationship between I_i and $\tilde{I}_i$. In what follows the latter approach will be utilized.

For the uniform shock, it can be shown by combining equations (4.25) and (4.26) that

$$\frac{\tilde{I}_i}{I_i} = \frac{(\gamma+1)\frac{p_s}{p_1} + 2\gamma}{(\gamma-1)\frac{p_s}{p_1} + 2\gamma}, \tag{4.33}$$

which is enough to obtain a formula for $I_p/\tilde{I}_i$ in the uniform shock case from (4.18).

For the exponential wave profile equation (4.33) can be rewritten as

$$\tilde{I}_i = \frac{(\gamma+1)\frac{p_s}{p_1} + 2\gamma}{(\gamma-1)\frac{p_s}{p_1} + 2\gamma} p_s t_i, \tag{4.34}$$

which upon taking differentials in time becomes

$$d\tilde{I} = \frac{(\gamma+1)\frac{p}{p_1} + 2\gamma}{(\gamma-1)\frac{p}{p_1} + 2\gamma} p dt. \tag{4.35}$$

For an exponential pressure profile $p(t) = p_s e^{-\frac{t}{t_i}}$, the relationship above can be integrated

$$\frac{\tilde{I}_i}{I_i} = \frac{\gamma+1}{\gamma-1} - \frac{1}{p_s/p_1} \frac{4\gamma}{(\gamma-1)^2} \ln\left(\frac{\gamma-1}{2\gamma}\frac{p_s}{p_1} + 1\right) \tag{4.36}$$

under the assumption that each overpressure contributes to the impulse according to the Rankine-Hugoniot relations (compare to the heavy plate limit in Section 4.2.2). For air with $\gamma = 1.4$, this equation simplifies to

$$\frac{\tilde{I}_i}{I_i} = 6 - \frac{35}{p_s/p_1} \ln\left(\frac{1}{7}\frac{p_s}{p_1} + 1\right). \tag{4.37}$$

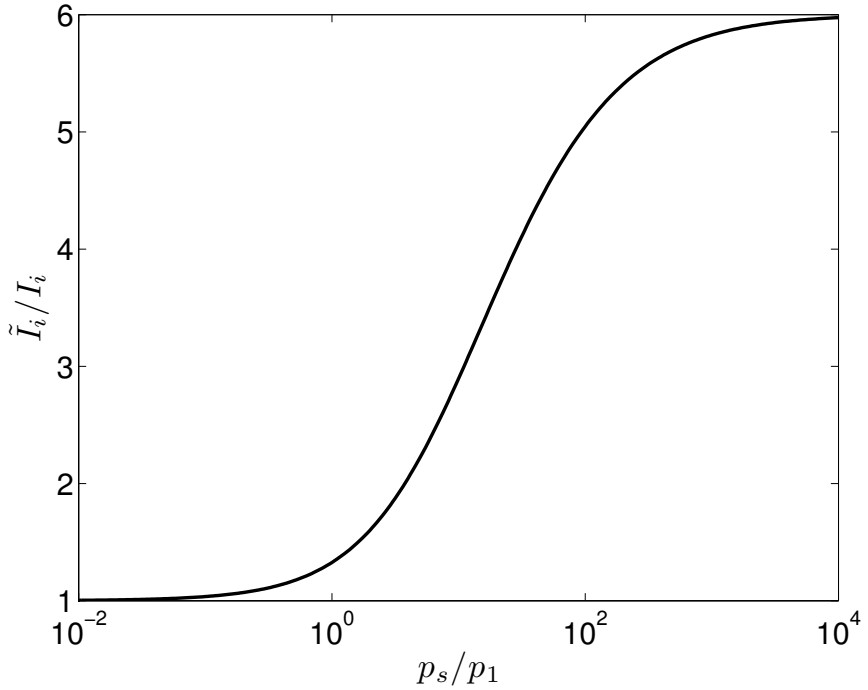

Figure 4-9: The dependence of $\tilde{I}_i/I_i$ on the peak overpressure ratio p_s/p_1 for exponentially decaying pressure profiles.

The dependence of $\tilde{I}_i/I_i$ on the overpressure p_s/p_1, equation (4.37), is shown in Figure 4-9, with the very small and very high overpressure limits being 1 and 6, respectively. The very high overpressure limit indicates that the dynamic momentum contribution $\rho_s u_s^2$ can be up to five times larger than the static overpressure pressure p_s.

Utilizing equation (4.37) the figures from Section 4.2.2 can be replotted for impulses non-dimensionalized relative to $\tilde{I}_i$. The dependence of $I_p/\tilde{I}_i$ on β_s is shown in Figure 4-10. The shape of the curves does not change, but they become closer to each other. Nevertheless they do not collapse onto a single line indicating that improvements in the estimation of $\tilde{I}_i$ for exponential profiles might be desirable and possible.

4.3 Active Protection from Air Blasts

The results from Section 3.4.1 on active protection without detection can be extended to the compressible range by utilizing the results of the previous section.

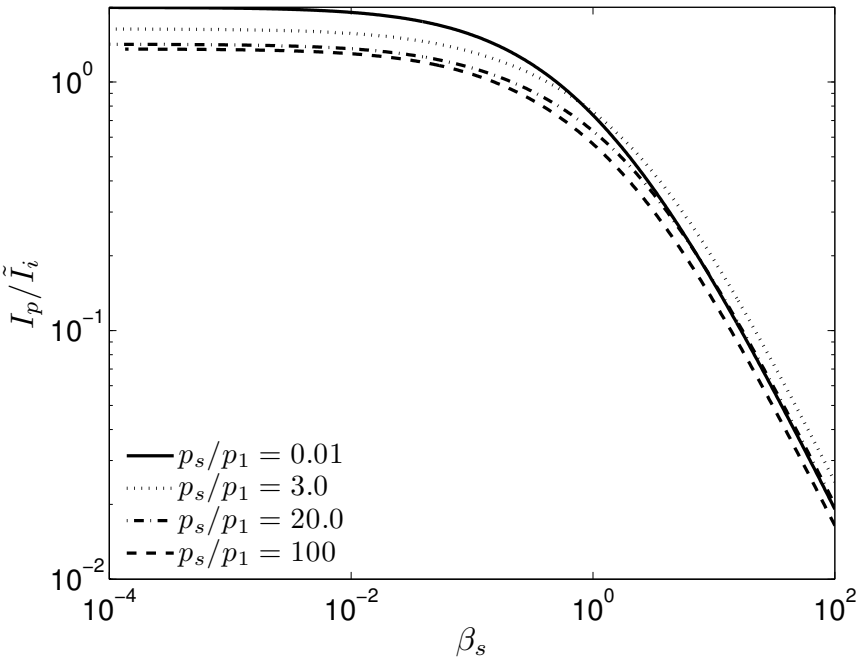

Figure 4-10: $I_p/\tilde{I}_i$ as a function of β_s for exponentially decaying pressure profiles.

The acoustic formula (3.94)

$$\frac{I_p}{I_i} = \underbrace{2\beta_0^{\frac{\beta_0}{1-\beta_0}}}_{\text{Taylor's Solution}} \underbrace{\left(1 - \delta\frac{1-\beta_0}{2\beta_0}\right)^{\frac{1}{1-\beta_0}}}_{\text{Correction Factor}} \tag{4.38}$$

consists of two parts: Taylor's solution and a correction factor due to the imparted initial velocity. A heuristic extension of this acoustic formula to the compressible range can be obtained by simply replacing the basic Taylor solution with the corresponding empirical formula (4.24) proposed in Section 4.2.2

$$\frac{I_p}{I_i} = \underbrace{\gamma_R \left(\frac{C_R f_R}{\gamma_R}\right)^{\frac{\beta_s}{1+\beta_s}} \beta_s^{\frac{\beta_s}{1-\beta_s}}}_{\text{Compressible Solution}} \underbrace{\left(1 - \eta\frac{1-\beta_0}{2}\right)^{\frac{1}{1-\beta_0}}}_{\text{Correction Factor}}, \tag{4.39}$$

where the active correction factor has been rewritten in terms of the non-dimensional impulse η for later convenience. It is also reasonable to replace the remaining acoustic quantities with their compressible counterparts. This implies replacing β_0

with β_s leading to

$$\frac{I_p}{I_i} = \underbrace{\gamma_R \left(\frac{C_R f_R}{\gamma_R}\right)^{\frac{\beta_s}{1+\beta_s}} \beta_s^{\frac{\beta_s}{1-\beta_s}}}_{\text{Compressible Solution}} \underbrace{\left(1 - \eta \frac{1-\beta_s}{2}\right)^{\frac{1}{1-\beta_s}}}_{\text{Correction Factor}}. \tag{4.40}$$

However, it can be shown that the limit of this expression for $\beta_s \to 0$

$$\lim_{\beta_s \longrightarrow 0} \frac{I_p}{I_i} = \gamma_R - \eta \frac{\gamma_R}{2} \tag{4.41}$$

is incorrect. The correct limit is obtained by considering that in the heavy plate limit the plate acts as a rigid wall with negligible motion. Therefore the transmitted impulse is still $\gamma_R I_i$, but the total impulse of the plate is $(\gamma_R - \eta) I_i$ due to the initial momentum $-\eta I_i$ carried by the plate. This suggest that the 2 in the equations above should be replaced by γ_R giving the final formula:

$$\frac{I_p}{I_i} = \underbrace{\gamma_R \left(\frac{C_R f_R}{\gamma_R}\right)^{\frac{\beta_s}{1+\beta_s}} \beta_s^{\frac{\beta_s}{1-\beta_s}}}_{\text{Compressible Solution}} \underbrace{\left(1 - \eta \frac{1-\beta_s}{\gamma_R}\right)^{\frac{1}{1-\beta_s}}}_{\text{Correction Factor}}. \tag{4.42}$$

This formula not only has the correct heavy plate limit of $\gamma_R - \eta$, but also the correct light plate asymptote:

$$\lim_{\beta_s \longrightarrow \infty} \frac{I_p}{I_i} \beta_s = \underbrace{(C_R f_R)}_{\text{Compressible Solution}} \times \underbrace{1}_{\text{Correction Factor}} = C_R f_R. \tag{4.43}$$

The formula (4.42) also degenerates to the acoustic expression (3.94) for small amplitude waves because in this case the compressible solution becomes Taylor's solution, the compressible fluid-structure interaction parameter β_s becomes the acoustic fluid-structure interaction parameter β_0 and the heavy plate transmission coefficient γ_R becomes 2. Therefore the proposed compressible formula for impulse transmission to actively deployable plates satisfies the expected limiting behavior for heavy and light plates and arbitrary blast intensity as well as arbitrary plate mass for acoustic waves.

In order to verify this formula, a series of numerical simulations has been con-

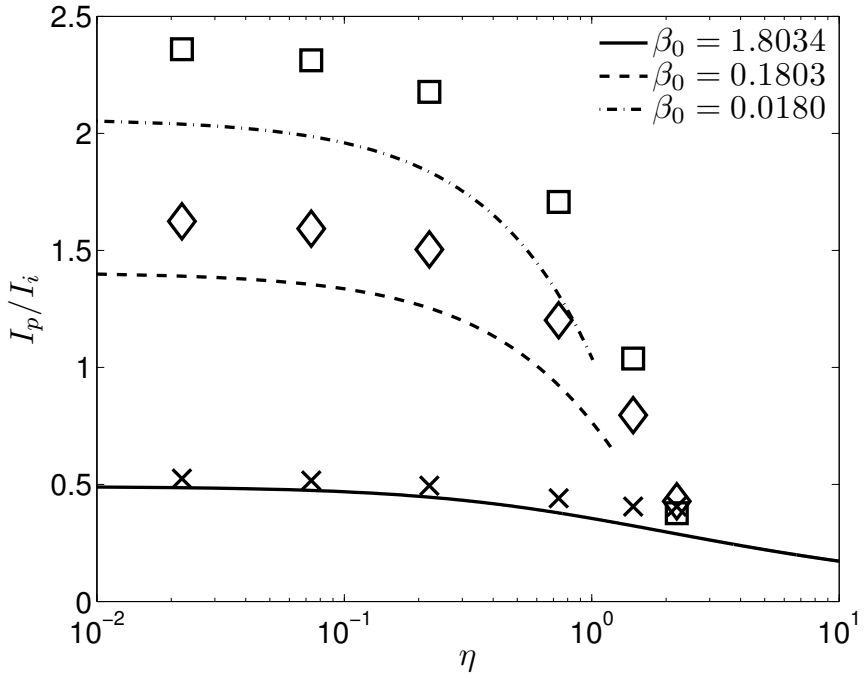

Figure 4-11: Maximum transmitted impulse I_p/I_i versus initially applied impulse η for $p_s/p_0 = 0.77$. The symbols and lines are obtained from numerical simulation and equation (4.42), respectively, with the following correspondence: $\times$ to the solid line, $\Diamond$ to the dashed line and $\Box$ to the dashed-dotted line.

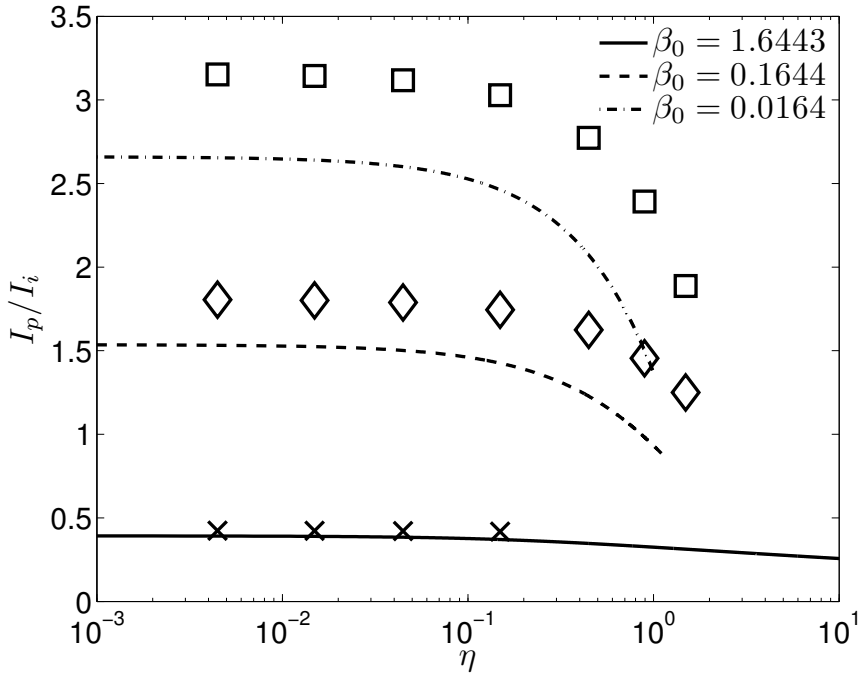

Figure 4-12: Maximum transmitted impulse I_p/I_i versus initially applied impulse η for $p_s/p_0 = 4.16$. The symbols and lines are obtained from numerical simulation and equation (4.42), respectively, with the following correspondence: $\times$ to the solid line, $\Diamond$ to the dashed line and $\square$ to the dashed-dotted line.

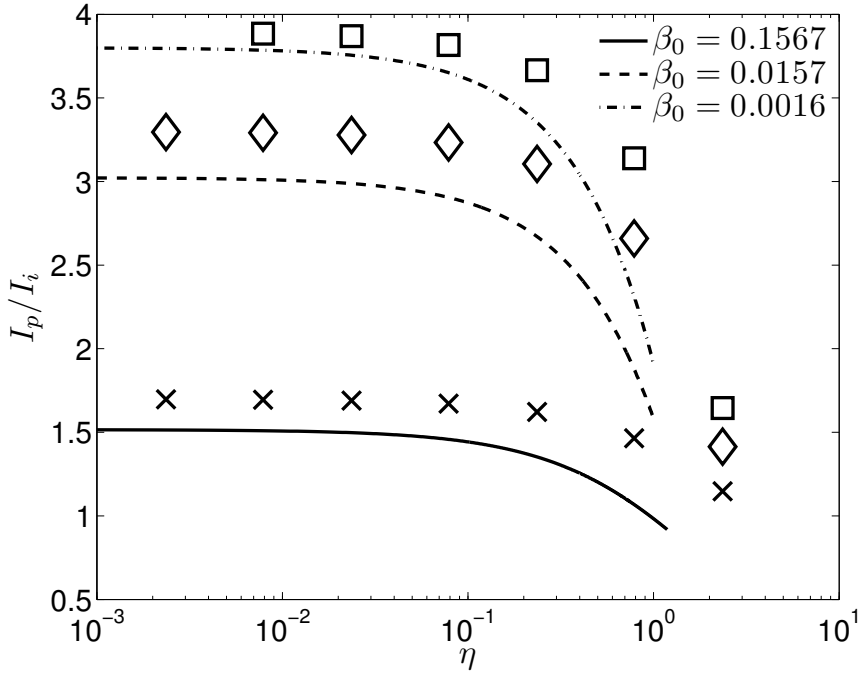

Figure 4-13: Maximum transmitted impulse I_p/I_i versus initially applied impulse η for $p_s/p_0 = 8.29$. The symbols and lines are obtained from numerical simulation and equation (4.42), respectively, with the following correspondence: $\times$ to the solid line, $\Diamond$ to the dashed line and $\Box$ to the dashed-dotted line.

ducted using the algorithm described in Appendix B. The simulations consisted of blast waves of various amplitudes traveling towards stationary plates of different weights similarly to the simulations presented in Section 4.2.2, but in addition the initial deployment conditions were accounted for by simply imparting an initial velocity V to the plate towards the incoming blast. The results of the numerical simulations are shown in Figures 4-11, 4-12 and 4-13 which display the dependence of the transmitted impulse I_p/I_i on η for three different overpressures[1]. The proposed formula (4.42) captures the qualitative behavior with η and β_0: the higher η is, the lower the transmitted impulse I_p/I_i is and the lower β_0 is, the higher the transmitted impulse I_p/I_i is. The lack of precise quantitative agreement is due mostly to the error inherited from the compressible formula (4.24) and the approximation for the heavy plate limit incorporated in it through γ_R.

4.4 Reflection of Von Neumann Profiles

The developments of the previous sections completely ignore the source of the blast wave – the blast wave shape and magnitude are assumed. Even though the blast wave shape and magnitude can be determined from empirical relationships [8] or numerical simulations [15] a more natural description of the problem of the blast-structure interaction is based on the released explosive energy and the distance between the explosion and the structure. This latter approach was taken by Taylor [117, 118] and von Neumann [126] who considered the propagation of blast waves from strong explosions in air. Based on purely dimensional considerations, Taylor derived the scaling laws relating the pressure at the blast front with the distance from the explosion and the elapsed time. He also found numerically the shape of the resulting wave. Von Neumann was able to obtain the exact similarity solution explicitly. A generalized version of von Neumann's solution valid for spherical, cylindrical and planar explosions is given in Appendix A.

In this section we describe the interaction of planar explosions with free-standing

[1]The lines in the figures are labeled with β_0 rather than β_s for convenience.

plates. Following von Neumann [126], the explosion can be described by its energy release per unit area E_0, the ambient density ρ_0 and pressure p_0. The unsupported structure is described by its mass per unit area m_p and its distance from the explosion center L. The output quantity of interest is the impulse I_p imparted to the structure.

The dimensional analysis that follows applies to the maximum impulse acquired by the structure as well as to any other characteristic impulse that can be defined independently of time. In one dimension, the dimensions of these parameters are as follows:

$$[E_0] = kg \cdot s^{-2}, \tag{4.44}$$

$$[\rho_0] = kg \cdot m^{-3}, \tag{4.45}$$

$$[p_0] = kg \cdot m^{-1} \cdot s^{-2}, \tag{4.46}$$

$$[m_p] = kg \cdot m^{-2}, \tag{4.47}$$

$$[L] = m, \tag{4.48}$$

$$[I_p] = kg \cdot m^{-1} \cdot s^{-1}. \tag{4.49}$$

The governing non-dimensional groups are

$$\Pi_1 = \frac{E_0 \rho_0}{p_0 m_p}, \tag{4.50}$$

$$\Pi_2 = \frac{\rho_0 L}{m_p}, \tag{4.51}$$

and the non-dimensional impulse of interest is

$$\frac{I_p}{\sqrt{\rho_0 E_0 L}}. \tag{4.52}$$

This implies that the functional dependence of the impulse is

$$\frac{I_p}{\sqrt{\rho_0 E_0 L}} = \mathcal{F}\left(\frac{E_0 \rho_0}{p_0 m_p}, \frac{\rho_0 L}{m_p}, \gamma\right), \tag{4.53}$$

where γ is a property of the fluid medium. The relationship (4.53) is inconvenient to

work with because the energy, the distance and the structure mass appear on both sides of the equation. However it can be rewritten as

$$v_p\sqrt{\frac{\rho_0}{p_0}}\sqrt{\frac{p_0 m_p}{E_0\rho_0}}\sqrt{\frac{m_p}{\rho_0 L}} = \mathcal{F}\left(\frac{E_0\rho_0}{p_0 m_p}, \frac{\rho_0 L}{m_p}, \gamma\right), \tag{4.54}$$

where v_p is the velocity of the structure. Introducing the speed of sound $a_0 = \sqrt{\gamma\frac{p_0}{\rho_0}}$, the last equation can be rewritten as

$$\frac{v_p}{a_0} = \mathcal{G}\left(\frac{E_0}{a_0^2 m_p}, \frac{\rho_0 L}{m_p}, \gamma\right), \tag{4.55}$$

for some other function $\mathcal{G}$. From this equation it can be concluded that the velocity of the structure is not modified if the explosion energy E_0, the distance to the explosion L and the mass of the structure m_p are all scaled up or down by the same constant.

Equation (4.55) deserves additional physical interpretation. The term $\rho_0 L/m_p$ is the ratio of the mass of air between the explosion and the structure to the mass of the structure. The term $E_0/a_0^2 m_p$ is the ratio of the energy released in the explosion to the energy of the structure were it to be moving at the speed of sound a_0. The term on the left hand side can be rewritten as $v_p/a_0 = I_p/a_0 m_p$ and represents the ratio of two impulses, the first one being the impulse of the plate I_p and the second one being the impulse of the plate were it moving at the speed of sound a_0. Equation (4.55) states that the impulse transmitted to the structure is dependent on the energy released by the explosion and the mass of fluid between the explosion and the structure.

It is interesting to revisit the analysis of impulse transmission in the previous sections in the context of the dimensional arguments presented in this section. To

Table 4.2: Correspondence between the exponential wave fluid-structure interaction theory of Section 4.2.2 and the planar wave interaction theory of this section.

Equation (4.24)	Equation (4.56)
$I_i = p_s t_i$	$I_i = \sqrt{\rho_0 E_0 L}$
$\beta_s = U_s t_i \rho_0 / m_p$	$\Pi_1 = (E_0/p_0)\rho_0/m_p$
$\frac{I_p}{I_i} = \mathcal{E}(\beta_s, \frac{p_s}{p_0})$	$\frac{I_p}{I_i} = \mathcal{H}(\Pi_1, \frac{p_s}{p_0})$

this end (1.2)[2] can be substituted in (4.55) to obtain

$$\frac{I_p}{\sqrt{\rho_0 E_0 L}} = \mathcal{H}\left(\frac{E_0\rho_0}{p_0 m_p}, \frac{p_s}{p_0}, \gamma\right). \tag{4.56}$$

with the second non-dimensional parameter

$$\Pi_2 = \frac{p_s}{p_0} \tag{4.57}$$

involving the maximum overpressure p_s at the time the wave reaches the structure. Equation (4.56) states that the impulse I_p transmitted to the structure is a function of a parameter governing the fluid-structure interaction $E_0\rho_0/p_0 m_p$ and the strength of the explosion p_s/p_0. There is significant similarity (see Table 4.2) between the functional dependence (4.56) and the formula for the transmitted impulse derived in Section 4.2.2, equation (4.24).

Figure 4-14 shows the dependence of the impulse[3] I_p on the non-dimensional parameter $\Pi_1 = E_0\rho_0/p_0 m_p$. The functional dependence $\mathcal{H}$ is similar to the functional dependence $\mathcal{E}$ shown in Figure 4-5.

[2]Equations (1.1) and (1.2) can be written in the form

$$L = C_L(\gamma)\left(\frac{E_0 t^2}{\rho_0}\right)^{\frac{1}{\nu+2}}$$
$$p_s = C_p(\gamma)\left(\frac{E_0^2\rho_0^\nu}{t^{2\nu}}\right)^{\frac{1}{\nu+2}} = \tilde{C}_p(\gamma)\frac{E_0}{L^\nu},$$

which for $\nu = 1, 2$ and 3 gives the proper scaling for planar, cylindrical and spherical explosions, respectively.

[3]This is the impulse transmitted to the plate up to the arrival at the plate of the secondary wave. The secondary reflected wave is caused by the singularity at the explosion center which causes the primary reflected wave to reflect back towards the plate. The secondary wave is a purely one-dimensional effect.

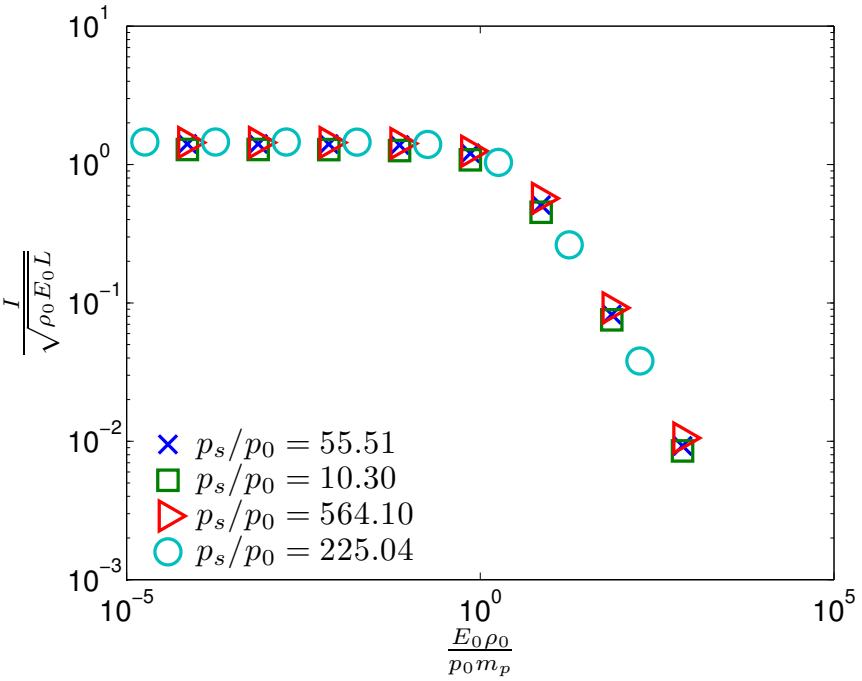

Figure 4-14: A set of simulation results describing the general behavior of the function $\mathcal{H}$ from equation (4.56).

A major difference between the results for the exponentially decaying profiles and the ones presented in Figure 4-14 is the very weak dependence on the second non-dimensional parameter p_s/p_0. This can be explained by the way the impulse I_p is non-dimensionalized. The ratio $I_p/\sqrt{\rho_0 E_0 L}$ varies with the energy E_0 and the distance L in a manner that scales the impulse correctly for all values of p_s/p_0. Indeed, this suggests that a better non-dimensionalization for I_p in equation (4.24) for the exponentially decaying profiles may exist. This was shown to be the case for uniform profiles where it was found that β_s/f_R was a single non-dimensional parameter describing the problem.

Chapter 5

Conclusions

In this thesis a number of extensions to a classic solution of blast-structure interaction by G. I. Taylor [119] has been proposed. Full solutions are obtained in the acoustic limit for a variety of blast and structure conditions including uniform and exponential wave profiles, structures with viscoelastic or wave transmitting supports and actively deployed plates. These solutions complement the previously existing solutions for unsupported plates and plates on perfectly plastic supports. Despite the limitations of the acoustic approximation the solutions provide insights and improved fundamental understanding of blast-structure interaction.

Regardless of the wave form and the support type, it is found that light plates over-perform heavy plates by a large margin. Light plates acquire significantly less momentum and energy while interacting with blast waves. However, active deployment provides significant benefits only to heavy plates and adds no further advantages to light plates. Explicit formulas for the energy transmitted to the plates are given. The energy dissipating requirements on the structures behind the plate can be determined from these formulas.

A significant part of this thesis is devoted to the analysis of the influence of fluid compressibility on the fluid-structure interaction response as compressibility is relevant in air blasts. Taylor's fundamental result for exponentially decaying pressure waves is extended to non-linear compressible media such as air. A generalized fluid-structure interaction parameter is proposed and a practical empirical formula for the

transmitted impulse is developed. The formula for exponentially decaying profiles can be used in the design of blast resistant structures. A similar compressible formula for uniform shock waves is also proposed. It is useful for the design and interpretation of shock tube experiments.

A new relevant measure of the incident impulse, the "total" impulse, is proposed. The "total" impulse properly takes into account the dynamic pressure allowing the almost complete collapse of the impulse transmission coefficient curves onto a single line.

The thesis concludes with an extension of the non-dimensional analysis of Taylor for strong point source explosions. The non-dimensional parameters relevant for the interaction of a point source explosion with a free-standing plate are given. The analogy between these parameters and the parameters governing the fluid-structure interaction for exponentially decaying pressure waves is discussed and the connections to the parameters of the explosion are given. The collapse of the numerical results for planar explosions onto a single line indicates that it might be possible to find a similarity solution to this problem.

The non-linear fluid-structure interaction theory developed in this work represents an improvement in the understanding of the interaction of blast waves with structures and can be utilized in designs of sandwich plates for protection against air blasts.

The author envisions continuation and extension of the work on impulse and energy transmission presented in this thesis in the following directions:

- Extension of the plastic support theory to the compressible range,
- Extension of the actively deployed theory for the applied pressure case to the compressible range,
- Extension of the viscoelastic supports theory to more complex support conditions,
- Exploration of the viability of wave decouplers consisting of layers of very soft and very stiff materials,

- Investigation of the possibility of finding a renormalization for the impulse transmission formula for the exponential profiles based on the "total" incident impulse and expressed in terms of a single non-dimensional parameter,
- Improvement of the heavy plate asymptotic limit for exponentially decaying profiles,
- Finding the optimal resistance force function to minimize structural deflection while keeping the reaction forces on the support below a design threshold,
- Investigate the possibility of deriving a similarity solution for the interaction of planar explosions with plates.

The future design challenges in the area of blast protection are to:

- Design of advanced (possibly nano-engineered) materials with very high energy dissipating capabilities over very small thicknesses,
- Design of practical sandwich panels to be used for retrofitting buildings and vehicles determined to be in danger of terrorist attacks,
- Incorporate blast mitigation considerations in the design of personal armor.

Appendix A

The Point Source Solution of Von Neumann

A.1 Exact Solution for a Point, Line and Plane Sources

A.1.1 Derivation of the Analytical Solution

This section shall follow closely the derivation presented by von Neumann in [126]. The important physical parameters in this problem are the energy E_0 released by the source, the ambient density ρ_0 and the ambient pressure p_0. The other variables which are part of the solution are the pressure p, the density ρ, the distance r from the source and the time t elapsed since the energy release. We shall attempt a general derivation for all three cases, the point, the line and the plane sources, and for that reason we introduce ν as the number of dimensions of the problem under consideration with $\nu = 3$, $\nu = 2$, or $\nu = 1$, respectively. The dimensions of the parameters are:

$$[E_0] = kg \cdot m^{\nu-1} \cdot s^{-2}, \tag{A.1}$$

$$[\rho_0] = kg \cdot m^{-3}, \tag{A.2}$$

$$[p_0] = kg \cdot m^{-1} \cdot s^{-2}, \tag{A.3}$$

and therefore there are two independent non-dimensional parameters

$$\Pi = \frac{E_0 t^2}{\rho_0 r^{\nu+2}}, \tag{A.4}$$

$$\Pi_2 = \frac{E_0}{p_0 r^{\nu}}. \tag{A.5}$$

Similarity solutions cannot be obtained in the presence of two significant non-dimensional parameters, but for strong explosions (such as nuclear ones) the second parameter Π_2 can be ignored as the pressure p_0 is much smaller than the pressures developed in the blast wave. In this case the only important non-dimensinal parameter is Π implying the following proportionality for all distances:

$$\text{lenght} \propto t^{\frac{2}{2+\nu}}. \tag{A.6}$$

A strong blast wave generates a strong discontinuous shock which separates the "fire-ball" from the undisturbed air at p_0. Let the location of this shock is L, x and X stand for the Eulerian and Lagrangian coordinates of any particle, respectively. Therefore we have

$$L = K_1 t^{\frac{2}{2+\nu}} \tag{A.7}$$

$$\frac{x}{t^{\frac{2}{2+\nu}}} = f\left(\frac{X}{t^{\frac{2}{2+\nu}}}\right). \tag{A.8}$$

In the interest of computational convenience we shall modify the last relation to

$$\frac{x}{K_1 t^{\frac{2}{2+\nu}}} = f\left(\frac{X}{K_1 t^{\frac{2}{2+\nu}}}\right). \tag{A.9}$$

The density ρ, particle velocity u and shock velocity U are given by

$$\rho = \rho_0 \left.\frac{\partial(X^\nu)}{\partial(x^\nu)}\right|_t = \rho_0 \frac{X^{\nu-1}}{x^{\nu-1}} \frac{\partial X}{\partial x} = \rho_0 \frac{z^{\nu-1}}{f^{\nu-1}(z)} \frac{1}{f'(z)} \tag{A.10}$$

$$u = \left.\frac{\partial x}{\partial t}\right|_X = K_1 \frac{2}{2+\nu} t^{-\frac{\nu}{2+\nu}} (f(z) - z f'(z)) \tag{A.11}$$

$$U = \frac{\partial L}{\partial t} = K_1 \frac{2}{2+\nu} t^{-\frac{\nu}{2+\nu}}, \tag{A.12}$$

where $z = \frac{X}{K_1 t^{2/(2+\nu)}}$. The relations for the discontinuous jumps of the flow variables at a shock can be found in any standard aerodynamics textbook (for example, [2]). The ones of interest here are:

$$\frac{\rho_s}{\rho_0} = \frac{(\gamma+1)p_s + (\gamma-1)p_0}{(\gamma-1)p_s + (\gamma+1)p_0} \tag{A.13}$$

$$u_s = \frac{(\gamma+1)^2 p_s - (\gamma^2+1)p_0}{2(\gamma+1)(p_s - p_0)} U \tag{A.14}$$

and can be derived from the equations in section 2.1.3. The subscript s is used to denote the conditions immediately behind the shock front. As discussed earlier setting strong explosions are equivalent to setting $p_0 = 0$ and hence the shock conditions simplify to

$$\frac{\rho_s}{\rho_0} = \frac{\gamma+1}{\gamma-1} \tag{A.15}$$

$$\frac{u_s}{U} = \frac{\gamma+1}{2}. \tag{A.16}$$

Displacements are continuous even at the shock, therefore $x = X$ and from the definition (A.9) it follows that:

$$f(1) = 1 \quad @ \quad z = 1. \tag{A.17}$$

Symmetry considerations imply

$$f(0) = 0 \quad @ \quad z = 0. \tag{A.18}$$

Equations (A.15) and (A.16) *both* imply the same condition on f

$$f'(1) = \frac{\gamma-1}{\gamma+1} \quad @ \quad z = 1. \tag{A.19}$$

There are no other restrictions imposed on f by the discontinuous jumps of the flow variables at the shock.

The change of entropy of an ideal gas going from state A to state B is given by

[110]

$$\Delta s = C_v \ln(\frac{p_B}{p_A}) + C_p \ln(\frac{v_B}{v_A}), \tag{A.20}$$

or after some manipulation taking into account that $\gamma = C_p/C_v$ for an ideal gas

$$e^{\frac{\Delta s}{C_v}} = \frac{p_B \rho_B^{-\gamma}}{p_A \rho_A^{-\gamma}}. \tag{A.21}$$

After the shock passage the process is adiabatic and therefore entropy is conserved following the fluid particles ($\Delta s = 0$):

$$p = p_s \left(\frac{\rho}{\rho_s}\right)^{\gamma}. \tag{A.22}$$

Sedov [104] refers to this equation as the adiabatic integral. With the appropriate extensions this adiabatic integral remains true in other cases of interest, such as flame propagation, detonation, implosions and others. Once again using the equations from section 2.1.3. The pressure behind the shock p_s can be expressed as

$$p_s = \frac{2}{\gamma+1}\rho_0 U_1^2 + \frac{\gamma-1}{\gamma+1}p_0, \tag{A.23}$$

or when $p_0 = 0$

$$p_s = \frac{2}{\gamma+1}\rho_0 U_1^2. \tag{A.24}$$

The Lagrangian position of a particle is given by $X = K_1 t^{2/(2+\nu)} z$. It $\tilde{t}$ is the time when the shock crosses a particle of interest then its Lagrangian position is also given by $K_1 \tilde{t}^{2/(2+\nu)}$ (because at that instant $z = 1$) and therefore $\tilde{t} = t\ z^{(2+\nu)/2}$. Eliminating the shock values p_s and ρ_s from (A.22) we obtain

$$p = \rho^{\gamma} 2 \frac{(\gamma-1)^{\gamma}}{(\gamma+1)^{\gamma+1}} \rho_0^{1-\gamma} U^2. \tag{A.25}$$

Eliminating ρ, U and $\tilde{t}$ leads to

$$p = \frac{8}{(\nu+2)^2} \frac{(\gamma-1)^{\gamma}}{(\gamma+1)^{\gamma+1}} \rho_0 K_1^2 t^{-\frac{2\nu}{2+\nu}} \frac{z^{(\nu-1)\gamma-\nu}}{f^{(\nu-1)\gamma}(z)} \frac{1}{f'^{\gamma}(z)}. \tag{A.26}$$

The total energy e of the gas is given by

$$e = \frac{1}{\gamma - 1}\frac{p}{\rho} + \frac{1}{2}u^2. \tag{A.27}$$

The total energy in a sphere with Lagrangian radius X is given by

$$E = \int_0^X \sigma \rho_0 e X^{\nu-1} dX, \tag{A.28}$$

where $\sigma = 2(\nu-1)\pi + \frac{1}{2}(\nu-2)(\nu-3)$. Substituting the expressions for the density ρ, pressure p and the velocity u and simplifying we obtain:

$$\begin{aligned} E = \sigma\rho_0 \int_0^z \Bigg[& \frac{8}{(\nu+2)^2}\frac{(\gamma-1)^{\gamma-1}}{(\gamma+1)^{\gamma+1}} K_1^2 t^{-\frac{2\nu}{2+\nu}} \frac{z^{(\nu-1)\gamma-2\nu+1}}{f^{(\nu-1)(\gamma-1)}(z) f'^{\gamma-1}(z)} \\ & + \frac{1}{2}K_1^2 \frac{4}{(\nu+2)^2} t^{-\frac{2\nu}{2+\nu}} \left(f(z) - z f'(z)\right)^2 \Bigg] K_1^\nu t^{\frac{2\nu}{2+\nu}} z^{\nu-1} dz \end{aligned} \tag{A.29}$$

$$\begin{aligned} = \sigma \frac{2}{(\nu+2)^2}\rho_0 K_1^{2+\nu} \int_0^z \Bigg[& 4\frac{(\gamma-1)^{(\gamma-1)}}{(\gamma+1)^{(\gamma+1)}} \frac{z^{(\nu-1)\gamma-2\nu+1}}{f^{(\nu-1)(\gamma-1)}(z) f'^{\gamma-1}(z)} \\ & + \left(f(z) - z f'(z)\right)^2 \Big] z^{\nu-1} dz. \end{aligned} \tag{A.30}$$

The expression above is true for any z, but in particular for the upper limit $z = 1$ and therefore equal to the initial energy release E_0. The constant K_1 can be found from that particular equality. As von Neumann pointed out ([126]), the fact that the expression is true for any z has important consequences, in particular, it allows for the explicit integration of the equations of motion (or their equivalent from the energy conservation which happens to be easier to work with). Stated in words the equation above states that the amount of energy flowing into the z sphere is exactly balanced by the amount of work done by the z sphere on the surroundings. Note that a constant z implies neither constant Lagrangian coordinate X, nor constant Eulerian coordinate x. Mathematically this statement can be expressed as follows:

$$\sigma \rho_0 X^{\nu-1} \left(dX\right)_t e = \sigma p x^{\nu-1} u dt, \tag{A.31}$$

where the left hand side equals to the energy of the material entering the z sphere

in in time dt and the right hand side equals to the work done by the same sphere on the surroundings (power equals force times velocity). Substitution in equation (A.31) leads to

$$\begin{aligned}
&\sigma\rho_0\left(\frac{8}{(\nu+2)^2}\frac{(\gamma-1)^{\gamma-1}}{(\gamma+1)^{\gamma+1}}K_1^2 t^{-\frac{2\nu}{\nu+2}}\frac{z^{(\nu-1)\gamma-2\gamma+1}}{f^{(\nu-1)(\gamma-1)(z)}f'^{\gamma-1}(z)}\right.\\
&\left.+\frac{1}{2}K_1^2\frac{4}{(\nu+2)^2}t^{-\frac{2\nu}{\nu+2}}(f(z)-zf'(z))^2\right)K_1^\nu z^\nu t^{\frac{\nu-2}{\nu+2}}dt\\
&=\sigma\frac{8}{(\nu+2)^2}\frac{(\gamma-1)^\gamma}{(\gamma+1)^{\gamma+1}}\rho_0 K_1^2 t^{-\frac{2\nu}{\nu+2}}\frac{z^{(\nu-1)\gamma-\nu}}{f^{(\nu-1)\gamma}(z)f'^{\gamma}(z)}K_1\\
&\times\frac{2}{2+\nu}t^{-\frac{\nu}{\nu+2}}(f(z)-zf'(z))K_1^{\nu-1}t^{\frac{2(\nu-1)}{\nu+2}}f^{\nu-1}(z),
\end{aligned}\tag{A.32}$$

which simplifies to

$$\begin{aligned}
&4\frac{(\gamma-1)^{\gamma-1}}{(\gamma+1)^{\gamma+1}}\frac{z^{(\nu-1)\gamma-\nu+1}}{f^{(\nu-1)(\gamma-1)}(z)f'^{\gamma-1}(z)}+z^\nu(f(z)-zf(z))^2\\
&=4\frac{(\gamma-1)^\gamma}{(\gamma+1)^{\gamma+1}}\frac{z^{(\nu-1)\gamma-\nu}}{f^{(\nu-1)(\gamma-1)}(z)f'^{\gamma}(z)}(f(z)-zf'(z)).
\end{aligned}\tag{A.33}$$

Let's temporary introduce

$$D=\frac{\gamma-1}{\gamma+1}.\tag{A.34}$$

One can easily check that

$$1-D=\frac{2}{\gamma+1}\tag{A.35}$$

and

$$\begin{aligned}
&(1-D)^2D^{\gamma-1}\frac{z^{(\nu-1)\gamma-\nu+1}}{f^{(\nu-1)(\gamma-1)}(z)f'^{\gamma-1}(z)}+z^\nu(f(z)-zf(z))^2\\
&=2(1-D)D^\gamma\frac{z^{(\nu-1)\gamma-\nu}}{f^{(\nu-1)(\gamma-1)}(z)f'^{\gamma}(z)}(f(z)-zf'(z)).
\end{aligned}\tag{A.36}$$

To solve this equation explicitly we introduce

$$z=e^w\tag{A.37}$$

$$f(z)=e^{\alpha w}\phi(w),\tag{A.38}$$

where α is to be determined later. The derivative $f'(z)$ is given by

$$f'(z) = e^{(\alpha-1)w}(\phi'(w) + \alpha\phi(w)). \tag{A.39}$$

Making the substitution in equation (A.36)

$$\begin{aligned}
&(1-D)^2 D^{\gamma-1} \frac{e^{w((\nu-1)\gamma-\nu+1)-\alpha w(\nu-1)(\gamma-1)-(\alpha-1)w(\gamma-1)}}{\phi^{(\nu-1)(\gamma-1)}(w)(\phi'(w)+\alpha\phi(w))'^{\gamma-1}} \\
&+ e^{\nu w+2\alpha w}(\phi(w) - \phi'(w) - \alpha\phi(w))^2 \\
&= 2(1-D)D^{\gamma} \frac{e^{w((\nu-1)\gamma-\nu)-\alpha w(\nu-1)(\gamma-1)-(\alpha-1)w\gamma+\alpha w}}{\phi^{(\nu-1)(\gamma-1)}(w)(\phi(w)+\alpha\phi(w))^{\gamma}} \\
&\times (\phi(w) - \phi'(w) - \alpha\phi(w)),
\end{aligned} \tag{A.40}$$

the explicit occurrence of w can be eliminated if all exponentials are the same, i.e. if

$$\alpha = \frac{\nu(\gamma-2)}{\nu\gamma - \nu + 2} \tag{A.41}$$

with the equation becoming

$$\begin{aligned}
&\frac{(1-D)^2 D^{\gamma-1}}{\phi^{(\nu-1)(\gamma-1)}(w)(\phi'(w)+\alpha\phi(w))'^{\gamma-1}} + (\phi(w) - \phi'(w) - \alpha\phi(w))^2 \\
&= \frac{2(1-D)D^{\gamma}}{\phi^{(\nu-1)(\gamma-1)}(w)(\phi(w)+\alpha\phi(w))^{\gamma}}(\phi(w) - \phi'(w) - \alpha\phi(w)).
\end{aligned} \tag{A.42}$$

Setting $\Psi = \phi'(w) + \alpha\phi$ we perform the following algebraic manipulations:

$$\begin{aligned}
&\frac{(1-D)^2 D^{\gamma-1}}{\phi^{(\nu-1)(\gamma-1)}(w)\Psi^{\gamma-1}(w)} + \left(\frac{\phi(w)}{\Psi(w)} - 1\right)^2 \\
&+ 2(1-D)D^{\gamma}\frac{1-\phi(w)/\Psi(w)}{\phi^{(\nu-1)(\gamma-1)}(w)\Psi^{\gamma+1}(w)} = 0,
\end{aligned} \tag{A.43}$$

$$\begin{aligned}
&\left(\frac{\phi/\Psi - 1}{1/D - 1}\right)^2 - 2\left(\frac{\phi/\Psi - 1}{1/D-1}\right)\frac{1}{\phi^{(\nu-1)(\gamma-1)}(\Psi/D)^{\gamma+1}} \\
&+ \frac{1}{\phi^{(\nu-1)(\gamma-1)}(\Psi/D)^{\gamma+1}} = 0.
\end{aligned} \tag{A.44}$$

To help clarify the solution process we introduce

$$\xi = \frac{\phi/\Psi - 1}{1/D - 1} \tag{A.45}$$

$$\eta = \phi^{(\nu-1)(\gamma-1)} \left(\frac{\Psi}{D}\right)^{\gamma+1}. \tag{A.46}$$

Equation (A.44) simply states that

$$\eta = \frac{2\xi - 1}{\xi^2}. \tag{A.47}$$

Defining yet another quantity θ such that

$$\xi = \frac{1+\theta}{2} \tag{A.48}$$

gives η as

$$\eta = \frac{4\theta}{(1+\theta)^2}. \tag{A.49}$$

Solving simultaneously the definitions of ξ and η gives

$$\phi = \eta^{\frac{1}{(\nu-1)(\gamma-1)+\gamma+1}} ((1-D)\xi + D)^{\frac{\gamma+1}{(\nu-1)(\gamma-1)+\gamma+1}} \tag{A.50}$$

$$\Psi = D\eta^{\frac{1}{(\nu-1)(\gamma-1)+\gamma+1}} ((1-D)\xi + D)^{-\frac{(\nu-1)(\gamma-1)}{(\nu-1)(\gamma-1)+\gamma+1}} \tag{A.51}$$

or upon substitution with θ

$$\phi = \theta^{\frac{1}{(\nu-1)(\gamma-1)+\gamma+1}} \left(\frac{1+\theta}{2}\right)^{-\frac{2}{(\nu-1)(\gamma-1)+\gamma+1}} \left(\frac{\gamma+\theta}{\gamma+1}\right)^{\frac{\gamma+1}{(\nu-1)(\gamma-1)+\gamma+1}} \tag{A.52}$$

$$\Psi = \frac{\gamma-1}{\gamma+1}\theta^{\frac{1}{(\nu-1)(\gamma-1)+\gamma+1}} \left(\frac{1+\theta}{2}\right)^{-\frac{2}{(\nu-1)(\gamma-1)+\gamma+1}} \left(\frac{\gamma+\theta}{\gamma+1}\right)^{-\frac{(\nu-1)(\gamma-1)}{(\nu-1)(\gamma-1)+\gamma+1}}. \tag{A.53}$$

Note that $\theta > 0$ because the positivity of η follows from the positivity of ϕ and Ψ which is a direct consequence of the positivity of f and f' (expression (A.10) for the density). We now proceed to find w in terms of θ:

$$\frac{d\phi}{dw} = \Psi - \alpha\phi \tag{A.54}$$

$$w = \int \frac{d\phi/\phi}{\Psi/\phi - \alpha} + c_1, \tag{A.55}$$

where c_1 is an integration constant to be determined later from the boundary conditions. One can easily verify that

$$d\phi/\phi = \frac{1}{\nu\gamma - \nu + 2}\frac{d\theta}{\theta} - \frac{2}{\nu\gamma - \nu + 2}\frac{d\theta}{1+\theta} + \frac{\gamma+1}{\nu\gamma - \nu + 2}\frac{d\theta}{\gamma+\theta} \tag{A.56}$$

$$\Psi/\phi = \frac{\gamma - 1}{\gamma + \theta}. \tag{A.57}$$

The integral to be evaluated becomes

$$\int \left(\frac{\gamma+\theta}{\theta(\nu + 2\gamma - 2 - \nu(\gamma-2)\theta)} - \frac{2(\gamma+\theta)}{(1+\theta)(\nu+2\gamma-2-\nu(\gamma-2)\theta)} + \frac{\gamma+1}{\nu+2\gamma-2-\nu(\gamma-2)\theta} \right) d\theta \tag{A.58}$$

with the final result for w being

$$w = c_1 + \frac{\gamma}{\nu+2\gamma-2}\ln\theta - \frac{2}{\nu+2}\ln(\theta+1) + \frac{(\nu^2+4)\gamma^2 + (8\nu - 3\nu^2 - 4)\gamma + 4\nu^2 - 8\nu}{\nu(\nu+2)(2-\gamma)(2\gamma+\nu-2)}\ln(\theta + \frac{\nu+2\gamma-2}{\nu(2-\gamma)}). \tag{A.59}$$

In terms of the newly introduced variables and notation the boundary conditions are found to be $\phi(0) = 1$ and $\Psi(0) = \frac{\gamma-1}{\gamma+1}$. Noting that the expressions for ϕ and Ψ in terms of θ imply that $\theta = 1$ whenever $w = 0$, the final result for w becomes

$$w = \frac{\gamma}{\nu+2\gamma-2}\ln\theta - \frac{2}{\nu+2}\ln\frac{\theta+1}{2} + \frac{(\nu^2+4)\gamma^2 + (8\nu - 3\nu^2 - 4)\gamma + 4\nu^2 - 8\nu}{\nu(\nu+2)(2-\gamma)(2\gamma+\nu-2)}\ln\frac{\nu(2-\gamma)\theta + \nu + 2\gamma - 2}{3\nu - \nu\gamma + 2\gamma - 2}. \tag{A.60}$$

The original variable z equals

$$z = \theta^{\frac{\gamma}{\nu+2\gamma-2}} \left(\frac{\theta+1}{2}\right)^{-\frac{2}{\nu+2}}$$

$$\times \left(\frac{\nu(2-\gamma)\theta+\nu+2\gamma-2}{3\nu-\nu\gamma+2\gamma-2}\right)^{\frac{(\nu^2+4)\gamma^2+(8\nu-3\nu^2-4)\gamma+4\nu^2-8\nu}{\nu(\nu+2)(2-\gamma)(2\gamma+\nu-2)}}. \tag{A.61}$$

The expressions for f and f' are found to be

$$f(z)=\theta^{\frac{\gamma-1}{\nu+2\gamma-2}}\left(\frac{\theta+1}{2}\right)^{-\frac{2}{\nu+2}}\left(\frac{\gamma+\theta}{\gamma+1}\right)^{\frac{\gamma+1}{\nu\gamma-\nu+2}} \times\left(\frac{\nu(2-\gamma)\theta+\nu+2\gamma-2}{3\nu-\nu\gamma+2\gamma-2}\right)^{-\frac{(\nu^2+4)\gamma^2+(8\nu-3\nu^2-4)\gamma+4\nu^2-8\nu}{(\nu+2)(2\gamma+\nu-2)(\nu\gamma-\nu+2)}}, \tag{A.62}$$

$$f'(z)=\frac{\gamma-1}{\gamma+1}\theta^{-\frac{1}{\nu+2\gamma-2}}\left(\frac{\gamma+\theta}{\gamma+1}\right)^{-\frac{(\nu-1)(\gamma-1)}{\nu\gamma-\nu+2}} \times\left(\frac{\nu(2-\gamma)\theta+\nu+2\gamma-2}{3\nu-\nu\gamma+2\gamma-2}\right)^{-\frac{(\nu^2+4)\gamma^2+(8\nu-3\nu^2-4)\gamma+4\nu^2-8\nu}{\nu(2-\gamma)(2\gamma+\nu-2)(\nu\gamma-\nu+2)}}, \tag{A.63}$$

respectively. To find an expression for $f(z)-zf'(z)$ we note that

$$\frac{f(z)}{zf'(z)}=\frac{\phi}{\Psi}=\frac{\gamma+\theta}{\gamma-1}, \tag{A.64}$$

and therefore

$$f(z)-zf'(z)=\frac{2}{\gamma-1}\frac{\theta+1}{2}zf'(z)=\frac{2}{\gamma+1}\theta^{\frac{\gamma-1}{\nu+2\gamma-2}}\left(\frac{\theta+1}{2}\right)^{\frac{\nu}{\nu+2}}\times \left(\frac{\gamma+\theta}{\gamma+1}\right)^{-\frac{(\nu-1)(\gamma-1)}{\nu\gamma-\nu+2}}\left(\frac{\nu(2-\gamma)\theta+\nu+2\gamma-2}{3\nu-\nu\gamma+2\gamma-2}\right)^{-\frac{(\nu^2+4)\gamma^2+(8\nu-3\nu^2-4)\gamma+4\nu^2-8\nu}{(\nu+2)(2\gamma+\nu-2)(\nu\gamma-\nu+2)}}. \tag{A.65}$$

With the help of the previous expressions the fundamental quantities in the problem can be written in terms of θ:

$$X=K_1 t^{\frac{2}{2+\nu}}\theta^{\frac{\gamma}{\nu+2\gamma-2}}\left(\frac{\theta+1}{2}\right)^{-\frac{2}{\nu+2}} \times\left(\frac{\nu(2-\gamma)\theta+\nu+2\gamma-2}{3\nu-\nu\gamma+2\gamma-2}\right)^{\frac{(\nu^2+4)\gamma^2+(8\nu-3\nu^2-4)\gamma+4\nu^2-8\nu}{\nu(\nu+2)(2-\gamma)(2\gamma+\nu-2)}}, \tag{A.66}$$

$$x=K_1 t^{\frac{2}{2+\nu}}\theta^{\frac{\gamma-1}{\nu+2\gamma-2}}\left(\frac{\theta+1}{2}\right)^{-\frac{2}{\nu+2}}\left(\frac{\gamma+\theta}{\gamma+1}\right)^{\frac{\gamma+1}{\nu\gamma-\nu+2}} \times\left(\frac{\nu(2-\gamma)\theta+\nu+2\gamma-2}{3\nu-\nu\gamma+2\gamma-2}\right)^{-\frac{(\nu^2+4)\gamma^2+(8\nu-3\nu^2-4)\gamma+4\nu^2-8\nu}{(\nu+2)(2\gamma+\nu-2)(\nu\gamma-\nu+2)}}, \tag{A.67}$$

$$\rho = \frac{\gamma+1}{\gamma-1}\rho_0\theta^{\frac{\nu}{\nu+2\gamma-2}}\left(\frac{\gamma+\theta}{\gamma+1}\right)^{-\frac{2(\nu-1)}{\nu\gamma-\nu+2}} \times \left(\frac{\nu(2-\gamma)\theta+\nu+2\gamma-2}{3\nu-\nu\gamma+2\gamma-2}\right)^{\frac{(\nu^2+4)\gamma^2+(8\nu-3\nu^2-4)\gamma+4\nu^2-8\nu}{(2-\gamma)(2\gamma+\nu-2)(\nu\gamma-\nu+2)}}, \tag{A.68}$$

$$u = \frac{4}{(2+\nu)(\gamma+1)}K_1 t^{-\frac{\nu}{\nu+2}}\theta^{\frac{\gamma-1}{\nu+2\gamma-2}}\left(\frac{\theta+1}{2}\right)^{\frac{\nu}{\nu+2}}\left(\frac{\gamma+\theta}{\gamma+1}\right)^{-\frac{(\nu-1)(\gamma-1)}{\nu\gamma-\nu+2}} \times \left(\frac{\nu(2-\gamma)\theta+\nu+2\gamma-2}{3\nu-\nu\gamma+2\gamma-2}\right)^{-\frac{(\nu^2+4)\gamma^2+(8\nu-3\nu^2-4)\gamma+4\nu^2-8\nu}{(\nu+2)(2\gamma+\nu-2)(\nu\gamma-\nu+2)}}, \tag{A.69}$$

$$p = \frac{8}{(\nu+2)^2(\gamma+1)}\rho_0 K_1^2 t^{-\frac{2\nu}{\nu+2}}\left(\frac{\theta+1}{2}\right)^{\frac{2\nu}{\nu+2}}\left(\frac{\gamma+\theta}{\gamma+1}\right)^{-\frac{2(\nu-1)\gamma}{\nu\gamma-\gamma+2}} \times \left(\frac{\nu(2-\gamma)\theta+\nu+2\gamma-2}{3\nu-\nu\gamma+2\gamma-2}\right)^{\frac{(\nu^2+4)\gamma^2+(8\nu-3\nu^2-4)\gamma+4\nu^2-8\nu}{(\nu+2)(2-\gamma)(\nu\gamma-\nu+2)}}. \tag{A.70}$$

An useful physical interpretation of the parameter θ can be obtained if the internal and kinetic energy per unit mass are compared:

$$e_{int} = \frac{1}{\gamma-1}\frac{p}{\rho} = \frac{8}{(2+\nu)^2(\gamma+1)^2}K_1^2 t^{-\frac{2\nu}{\nu+2}}\theta^{-\frac{\nu}{\nu+2\gamma-2}}\left(\frac{\theta+1}{2}\right)^{\frac{2\nu}{\nu+2}}\left(\frac{\gamma+\theta}{\gamma+1}\right)^{-\frac{2(\nu-1)(\gamma-1)}{\nu\gamma-\nu+2}} \times \left(\frac{\nu(2-\gamma)\theta+\nu+2\gamma-2}{3\nu-\nu\gamma+2\gamma-2}\right)^{-\frac{2((\nu^2+4)\gamma^2+(8\nu-3\nu^2-4)\gamma+4\nu^2-8\nu)}{(\nu+2)(2\gamma+\nu-2)(\nu\gamma-\nu+2)}}, \tag{A.71}$$

$$e_{kin} = \frac{1}{2}u^2 = \frac{8}{(2+\nu)^2(\gamma+1)^2}K_1^2 t^{-\frac{2\nu}{\nu+2}}\theta^{\frac{2(\gamma-1)}{\nu+2\gamma-2}}\left(\frac{\theta+1}{2}\right)^{\frac{2\nu}{\nu+2}}\left(\frac{\gamma+\theta}{\gamma+1}\right)^{-\frac{2(\nu-1)(\gamma-1)}{\nu\gamma-\nu+2}} \times \left(\frac{\nu(2-\gamma)\theta+\nu+2\gamma-2}{3\nu-\nu\gamma+2\gamma-2}\right)^{-\frac{2((\nu^2+4)\gamma^2+(8\nu-3\nu^2-4)\gamma+4\nu^2-8\nu)}{(\nu+2)(2\gamma+\nu-2)(\nu\gamma-\nu+2)}}, \tag{A.72}$$

hence

$$\frac{e_{kin}}{e_{int}} = \theta. \tag{A.73}$$

Equation (A.73) remains true if we consider the energies per unit volume $\tilde{e}_{kin}$ and $\tilde{e}_{int}$:

$$\frac{\tilde{e}_{kin}}{\tilde{e}_{int}} = \theta. \tag{A.74}$$

Noting that $\tilde{e}_{int} = e_{int}\rho = p/(\gamma-1)$ the constant K_1 can be obtained from the energy

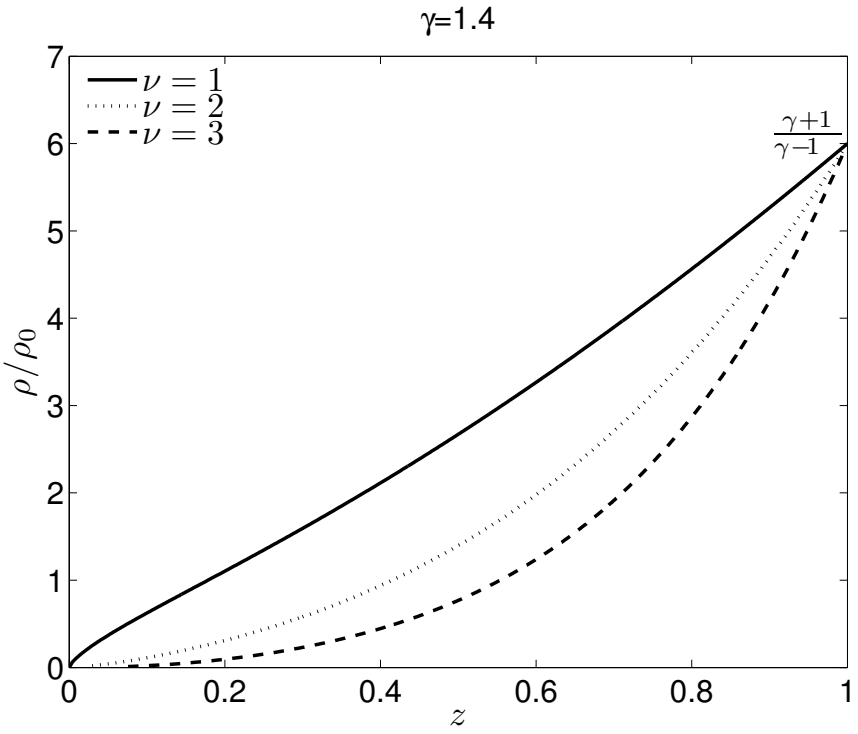

Figure A-1: Density distribution within the blast sphere

integral:

$$E_0 = \int_0^L (\tilde{e}_{int} + \tilde{e}_{kin})\sigma x^{\nu-1} dx = 2\sigma L^\nu \int_0^1 \left(\frac{\theta+1}{2}\right) \tilde{e}_{int} f^{\nu-1} df$$
$$= \frac{2\sigma}{\nu(\gamma-1)} K_1^\nu t^{\frac{2\nu}{2+\nu}} \int_0^1 \frac{\theta+1}{2} p d(f^\nu) = \rho_0 C_2 K_1^{\nu+2}, \tag{A.75}$$

where

$$C_2 = \frac{16\sigma}{\nu(\nu+2)^2(\gamma^2-1)} \int_0^1 \left(\frac{\theta+1}{2}\right)^{\frac{3\nu+2}{\nu+2}} \left(\frac{\gamma+\theta}{\gamma+1}\right)^{-\frac{2(\nu-1)\gamma}{\nu\gamma-\nu+2}}$$
$$\times \left(\frac{\nu(2-\gamma)\theta+\nu+2\gamma-2}{3\nu-\nu\gamma+2\gamma-2}\right)^{\frac{(\nu^2+4)\gamma^2+(8\nu-3\nu^2-4)\gamma+4\nu^2-8\nu}{(\nu+2)(2-\gamma)(\nu\gamma-\nu+2)}} d(f^\nu). \tag{A.76}$$

Von Neumann gives $C_2 = 0.8510$ for $\gamma = 1.4$ and $\nu = 3$ [126]. Simpler formulae which approximates the exact solution presented above can be found in [117]. Discussion about the effects of different values of γ is available in [104]. Noting that for $0 \leq z \leq 1$ one needs $0 \leq \theta \leq 1$ we can plot the dependence of the density, velocity

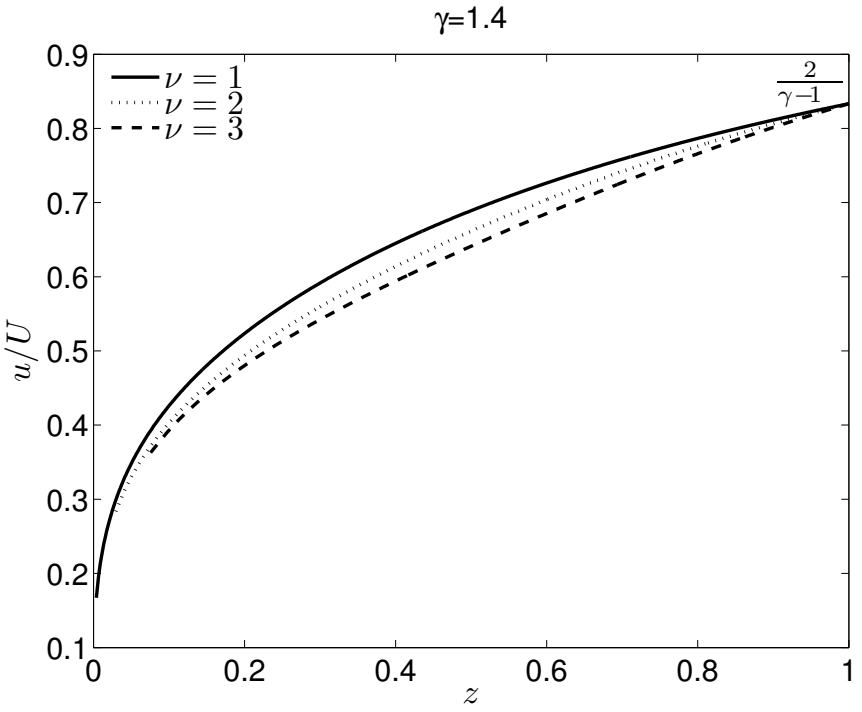

Figure A-2: Velocity distribution within the blast sphere

and pressure on z (see Figures A-1,A-2 and A-3).

A.1.2 Jump Conditions at the Blast Front

At the blast front ($\theta = 1$) the following relationships hold:

$$L = K_1 t^{\frac{2}{2+\nu}}, \tag{A.77}$$

$$\rho = \frac{\gamma+1}{\gamma-1}\rho_0, \tag{A.78}$$

$$u = \frac{4}{(2+\nu)(\gamma+1)} K_1 t^{-\frac{\nu}{\nu+2}}, \tag{A.79}$$

$$p = \frac{8}{(\nu+2)^2(\gamma+1)}\rho_0 K_1^2 t^{-\frac{2\nu}{\nu+2}}. \tag{A.80}$$

The second equation is direct result of $p/p_0 = +\infty$. The shock jump conditions (2.38) and (2.39) can be rewritten as:

$$U = \sqrt{\frac{\gamma+1}{2}\frac{p}{\rho_0}}, \tag{A.81}$$

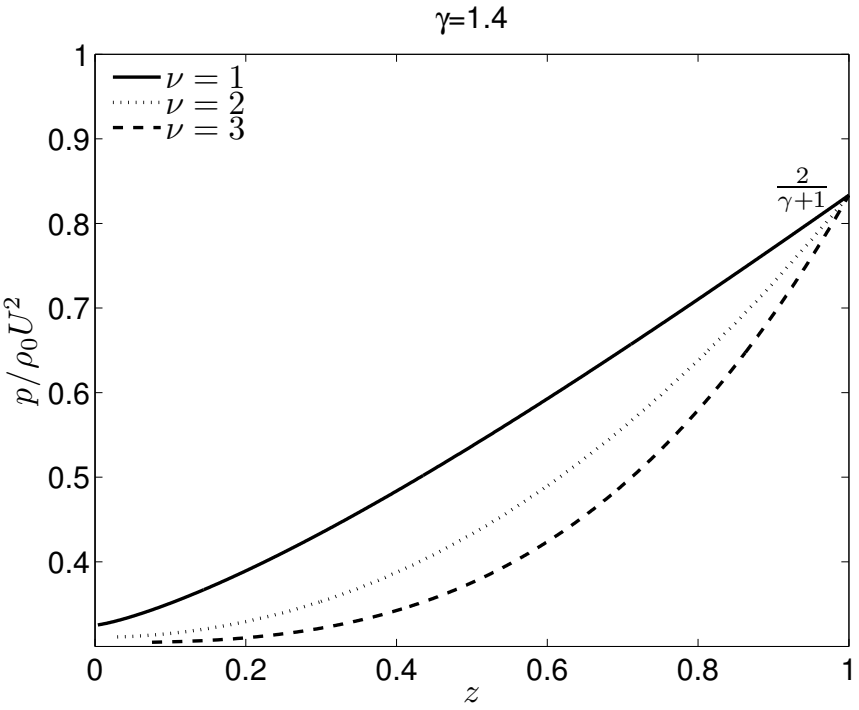

Figure A-3: Pressure distribution within the blast sphere

$$u_s = \sqrt{\frac{2}{\gamma+1}\frac{p}{\rho_0}}. \tag{A.82}$$

because $p_0 = 0$ assumption for the similarity solution. For verification of (A.81), one needs to take into account that $\frac{\partial L}{\partial t} = U$, while the second one verifies directly.

A.1.3 Numerical Results

To test the implementation of the numerical code, the exact solution of von Neumann was implemented. The resulting spatial pressure profiles at different instances of time are shown in Figure A-4. It should be noted that due to the singularity at the explosion center the numerical solution may deviate significantly from the exact solution in vicinity of the origin. Specifically, the element in the explosion center is initially disproportionally larger than the other elements and this disproportionality grows with time. In principle there is the possibility of the whole numerical solution deteriorating very quickly in the center, but such deterioration was not observed outside of a small neighborhood of the center.

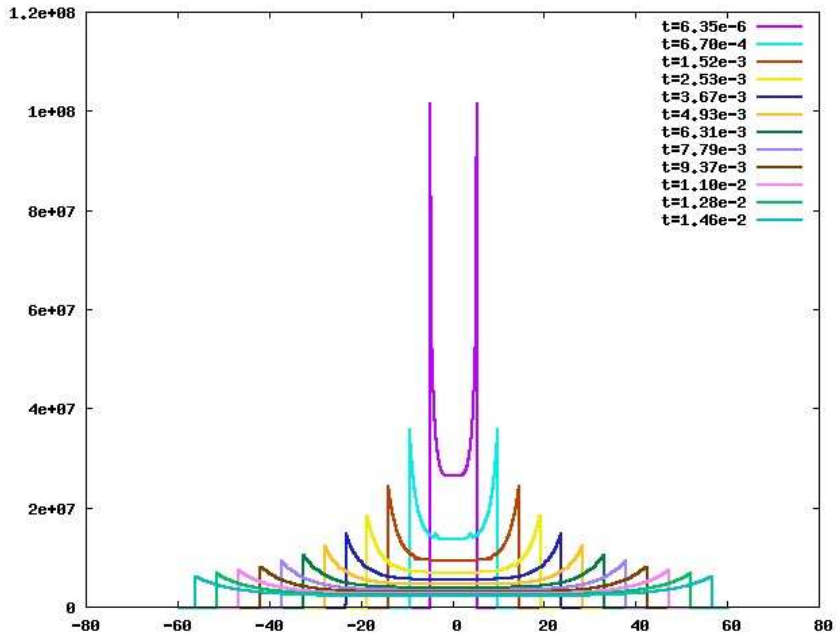

Figure A-4: Evolution of the spatial pressure profiles with time for planar source explosion (1-D)

In the numerical simulations the energy released was $E_0 = 5 \times 10^8$ J/m^2, with the initial radius being $L = 5$ m. Figures A-5 and A-6 show a comparison of the profile obtained by the numerical simulation at explosion radius $L \approx 43.0$ m and the analytical solution at the same radius. The agreement between both is quite good, with the large central element introducing some differences and slight deviations in the peak overpressure and the density ratio. This deviation is caused by the finite ratio of the peak overpressure to the ambient pressure which was assumed to be infinite in the analytical solution and is not indicative of the quality of the numerical approximation.

It should be emphasized that the one dimensional explosion does not cause negative overpressures typical of real three dimensional explosions. This is demonstrated in Figure A-7. The energy released in the explosion is $E_0 = 4 \times 10^7$ J/m^2 and the snapshot shown is at time $t = 2.061$ s. The peak overpressure has decayed to under 1 atm, but still there is no location in the domain where the overpressure is negative. This is a peculiar property of the one dimensional explosions and is in a direct contrast with the three dimensional experimental data.

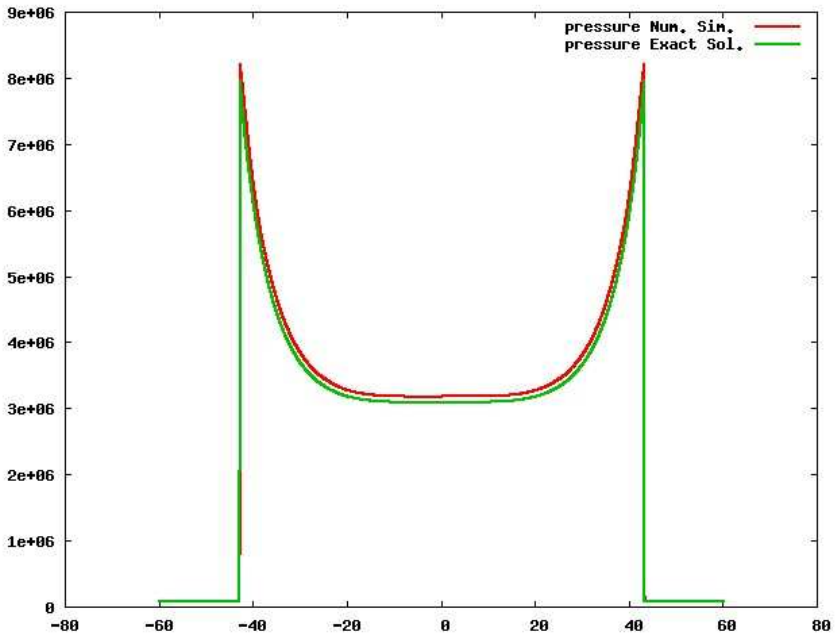

(a) Comparison of pressure profiles

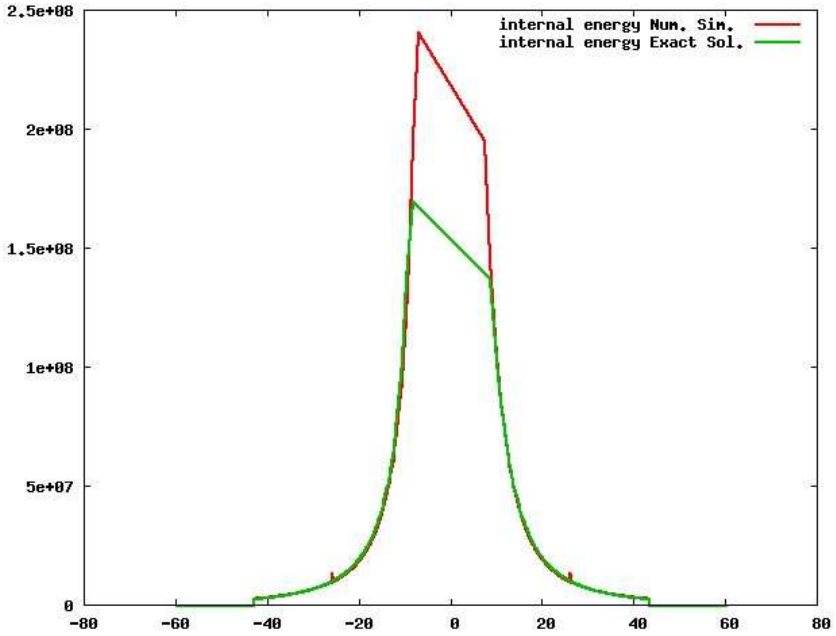

(b) Comparison of internal energy profiles

Figure A-5: Comparisons of pressure and internal energy profiles obtained from the exact solution and the numerical simulation.

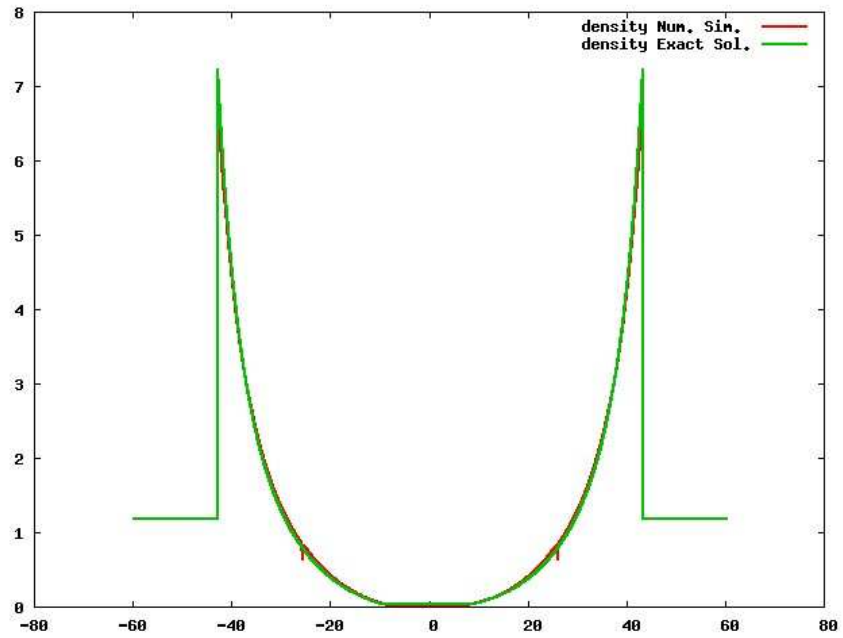

(a) Comparison of density profiles

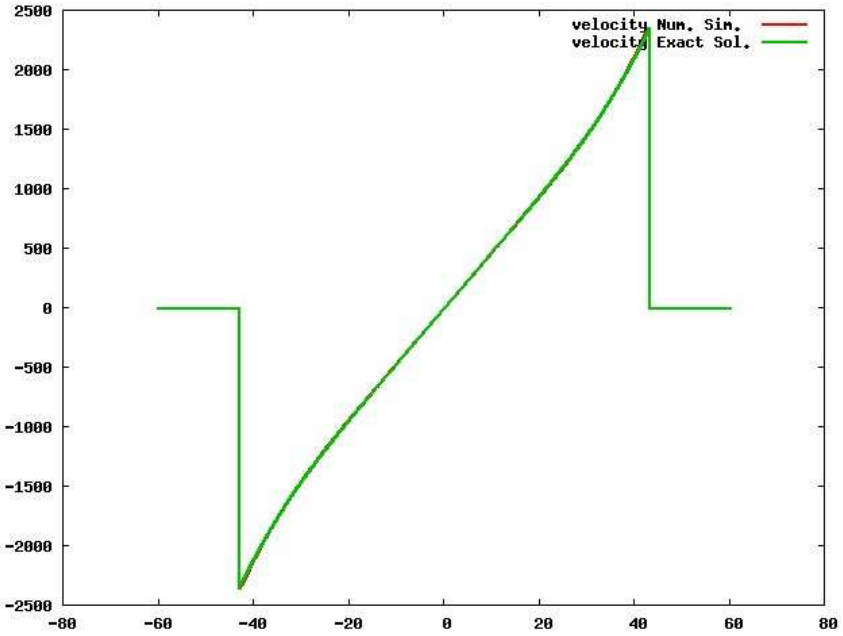

(b) Comparison of velocity profiles

Figure A-6: Comparisons of density and velocity profiles obtained from the exact solution and the numerical simulation.

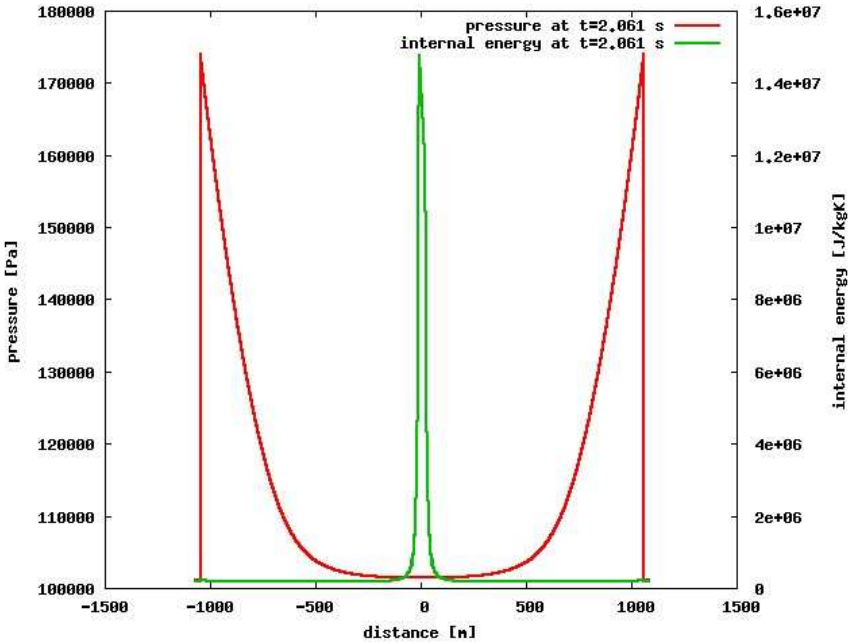

(a) Pressure and internal energy profiles at $t = 2.061$ s

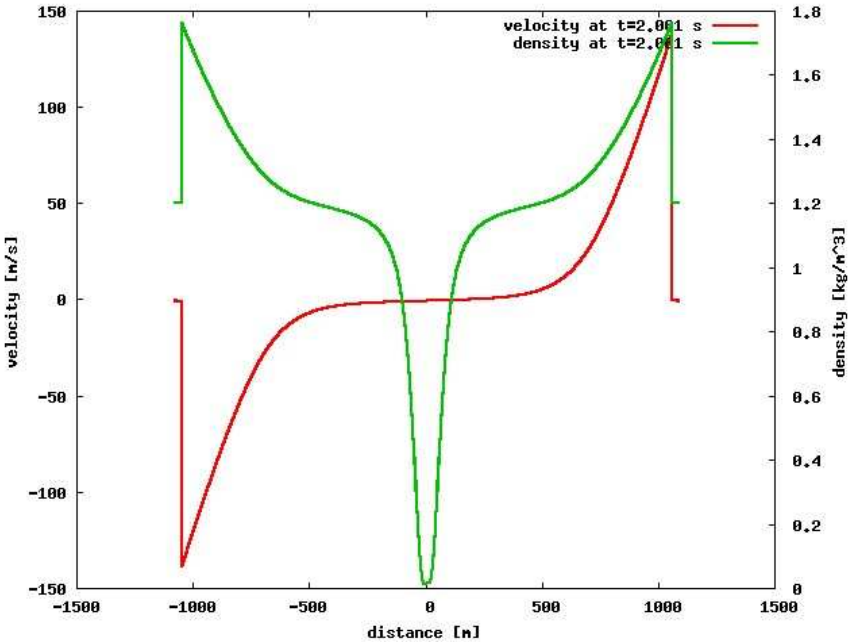

(b) Velocity and density profiles at $t = 2.061$ s

Figure A-7: Profiles very long time after a planar explosion.

Appendix B

The Finite Difference Numerical Method

B.1 Coupled Problem Statement

The problem of interest consists of a non-linear wave traveling in a compressible inviscid fluid interacting with a plate at the end of the domain under consideration. The equations governing the motion of the fluid are expressed in the Lagrangian framework and consist of:

- Kinematic relations for the material velocity and acceleration

$$\begin{aligned} V &= \frac{\partial x}{\partial t}, \\ A &= \frac{\partial V}{\partial t}, \end{aligned}$$

  where x is the spatial coordinate of each fluid particle X which is tracked throughout the flow, V and A are the particle velocity and acceleration, respectively, and t is the time.

- Momentum conservation

$$\rho_i A = -\frac{\partial p}{\partial X}, \tag{B.1}$$

where ρ_i is the initial density of the particle with Lagrangian coordinate X and p is its pressure.

- Equation of state

$$p = \rho RT - Q = (\gamma - 1)\rho_i \frac{e}{F} - Q, \tag{B.2}$$

where R is the ideal gas constant, T is the temperature, $\gamma = \frac{c_p}{c_v}$ is the ratio of the specific heats of the gas, $e = c_v T$ is the internal energy, c_p and c_v are the specific heats at constant pressure and volume respectively, $F = \frac{\partial x}{\partial X}$ is the deformation gradient and Q is an artificial viscous dissipation term required to stabilize the numerical solution. This term Q consists of two contributions: a quadratic term in the deformation rate $D = \frac{1}{F}\frac{\partial F}{\partial t}$, as originally proposed by von Neumann and Richtmyer [127], and a linear term in D proposed by Kuropatenko [56]. The quadratic term damps the oscillations close to the discontinuities, while the linear term stabilizes unstable weak sound waves. The resulting expression for the artificial viscosity is:

$$Q = \begin{cases} -\rho_i (K_1 D\,\Delta)^2 - \rho_i K_2 a |D|\,\Delta, & D < 0 \\ 0, & D \geq 0 \end{cases}, \tag{B.3}$$

where K_1 and K_2 are the artificial viscosity coefficients, Δ is the width of the smeared shock which needs to be of the order of the grid spacing to avoid numerical instabilities and $a = \sqrt{\gamma RT} = \sqrt{\gamma(\gamma - 1)e}$ is the local speed of sound.

- Energy conservation

$$\frac{\partial e}{\partial t} = \left[(1 - \gamma)e + \frac{Q}{\rho}\right] D, \tag{B.4}$$

where ρ is the current density of the particle.

The choice of the Lagrangian framework leads to a natural description of the dynamics of the plate as the positions of the material fluid points, including the material fluid-plate interface become the primary unknowns of the problem. Following Taylor, we focus on the dynamic response of the plate as a rigid body and ignore the effects

of deformation and stress-wave propagation inside it on the grounds that the time scales involved in the elastic vibrations are typically at least three orders of magnitude smaller than in the coupled fluid-structure dynamics and that the amplitudes are small and do not affect the flow. Thus, the equation of motion of the plate is given by Newton's second law

$$A_p = \frac{p_p}{\rho_p h_p}, \tag{B.5}$$

where A_p is the acceleration of the plate. The acceleration is defined in terms of the overpressure, so that the plate is in equilibrium under atmospheric conditions. This equation constitutes the boundary condition on the right end of the fluid domain. The boundary condition on the left end depends on the particular problem. The initial conditions are also problem dependent but in all cases include the condition that material and spatial coordinates coincide at $t = 0$: $x(X, t = 0) = X$.

The numerical formulation corresponds to the original method proposed by von Neumann-Richtmyer method [127] based on a finite difference discretization of the governing equations. The implementation follows closely the guidelines described in [34] with appropriate extensions to account for the coupling with the dynamics of the plate.. The computer implementation of the algorithm was verified by computing the normal reflection of shocks at a rigid boundary and by comparing the pressure reflection coefficients with the exact values. As a second test of the correctness of the numerical method, simulations of very low-intensity blast waves interacting with plates of different mass are conducted in order to verify that Taylor's acoustic solution is reproduced by the numerical results, see also Section 4.2.2.

B.2 Numerical Formulation

A finite difference spatial discretization of the governing equations in section B.1 is adopted. The domain of interest is discretized into a uniform grid of $N + 1$ points equally spaced in the undeformed configuration. The coordinates of the grid points are $x_0^{(n)} = X^{(n)} = n\Delta X$ where $n = 0, 1, ..., N$ is the point number and ΔX is the grid spacing. The time interval of interest is discretized in variable time steps $\Delta t_j, \quad j =$

$1, 2, ...$, such that the solution is sampled at discrete times $t_0, \cdots, t_{j-1}, t_j = t_{j-1} + \Delta t_j, \cdots$. The temporal discretization is based on the finite difference approximation for the velocity

$$V_{j+\frac{1}{2}}^{(n)} = \frac{x_{j+1}^{(n)} - x_j^{(n)}}{\Delta t_{j+1}},$$

leading to

$$x_{j+1}^{(n)} = x_j^{(n)} + \Delta t_{j+1} V_{j+\frac{1}{2}}^{(n)}. \tag{B.6}$$

From the finite difference approximation of the acceleration one obtains

$$V_{j+\frac{1}{2}}^{(n)} = V_{j-\frac{1}{2}}^{(n)} + \frac{1}{2}(\Delta t_{j+1} + \Delta t_j) A_j^{(n)}, \tag{B.7}$$

where the time step is averaged over the current and previous time step and the velocity is defined only in the middle of the time steps. The acceleration is be determined from the momentum conservation equation (B.1)

$$A_j^{(n)} = -\frac{1}{\rho_0^{(n)}} \frac{p_j^{(n+\frac{1}{2})} - p_j^{(n-\frac{1}{2})}}{\Delta X}. \tag{B.8}$$

The discretized equations are as follows:

$$p_{j+1}^{(n+\frac{1}{2})} = (\gamma - 1)\rho_i \frac{e_{j+1}^{(n+\frac{1}{2})}}{F_{j+1}^{(n+\frac{1}{2})}} - Q_{j+\frac{1}{2}}^{(n+\frac{1}{2})}, \tag{B.9}$$

$$\begin{aligned} Q_{j+\frac{1}{2}}^{(n+\frac{1}{2})} &= -\rho_i \left(K_1 \Delta x_{j+\frac{1}{2}}^{(n+\frac{1}{2})} D_{j+\frac{1}{2}}^{(n+\frac{1}{2})} \right)^2 \\ &\quad - \rho_i K_2 a_j^{(n+\frac{1}{2})} \Delta x_{j+\frac{1}{2}}^{(n+\frac{1}{2})} |D_{j+\frac{1}{2}}^{(n+\frac{1}{2})}|, \end{aligned} \tag{B.10}$$

$$a_j^{(n+\frac{1}{2})} = \sqrt{\gamma(\gamma - 1) e_j^{(n+\frac{1}{2})}} \tag{B.11}$$

$$D_{j+\frac{1}{2}}^{(n+\frac{1}{2})} = \frac{2}{\Delta t_{j+1}} \frac{F_{j+1}^{(n+\frac{1}{2})} - F_j^{(n+\frac{1}{2})}}{F_{j+1}^{(n+\frac{1}{2})} + F_j^{(n+\frac{1}{2})}}, \tag{B.12}$$

$$\Delta x_{j+\frac{1}{2}}^{(n+\frac{1}{2})} = \frac{1}{2} \left(x_{j+1}^{(n+1)} - x_{j+1}^{(n)} + x_j^{(n+1)} - x_j^{(n)} \right), \tag{B.13}$$

$$e_{j+1}^{(n+\frac{1}{2})} = \frac{e_j^{(n+\frac{1}{2})} + \left(\frac{1-\gamma}{2} e_j^{(n+\frac{1}{2})} + \frac{Q_{j+\frac{1}{2}}^{(n+\frac{1}{2})}}{\rho_{j+\frac{1}{2}}^{(n+\frac{1}{2})}} \right) \Delta t_{j+1} D_{j+\frac{1}{2}}^{(n+\frac{1}{2})}}{1 + \frac{\gamma-1}{2} \Delta t_{j+1} D_{j+\frac{1}{2}}^{(n+\frac{1}{2})}}, \tag{B.14}$$

$$\rho_{j+\frac{1}{2}}^{(n+\frac{1}{2})} = \frac{\rho_i^{(n+\frac{1}{2})}}{2} \left(\frac{1}{F_{j+1}^{(n+\frac{1}{2})}} + \frac{1}{F_j^{(n+\frac{1}{2})}} \right), \tag{B.15}$$

$$\rho_i^{(n+\frac{1}{2})} = \frac{\rho_i^{(n+1)} + \rho_i^{(n)}}{2}, \tag{B.16}$$

where the deformation gradient F is given by

$$F_j^{(n+\frac{1}{2})} = \frac{x_j^{(n+1)} - x_j^{(n)}}{\Delta X}. \tag{B.17}$$

A typical step forward of the algorithm for an interior point proceeds first by computing the time step $\Delta t_j = \alpha \min \left(\frac{x_{j-1}^{(n)} - x_{j-1}^{(n-1)}}{a_{j-1}^{(n-1)}} \right)$ where the minimum is taken over all possible values of n and α is a time factor. The deformation gradient $F_j^{(n+\frac{1}{2})}$ can be computed from (B.17) followed by evaluation of $D_{j+\frac{1}{2}}^{(n+\frac{1}{2})}$ and $\Delta x_{j+\frac{1}{2}}^{(n+\frac{1}{2})}$. Immediately afterwards $Q_{j+\frac{1}{2}}^{(n+\frac{1}{2})}$ and $e_{j+1}^{(n+\frac{1}{2})}$ can be obtained from (B.10) and (B.14). Now, equation (B.9) gives the pressure which can be substituted in (B.8) to obtain the acceleration $A_j^{(n)}$. Next, (B.7) and (B.6) lead to $x_{j+1}^{(n)}$ closing the loop as now the next deformation gradient can be computed. In the first step, the previous values of the Eulerian coordinates $x_{-1}^{(n)}$ are unknown and therefore assumed to be equal to the Eulerian coordinates $x_0^{(n)}$ at time $t = 0$. The overpressure p_p required for the computation of the acceleration of the plate is obtained from the pressure of the neighboring interior point.

Bibliography

[1] John D. Anderson. *Hypersonic and High Temperature Gas Dynamics*. McGraw-Hill, New York, New York, 1989.

[2] John D. Anderson. *Fundamentals of Aerodynamics*. McGraw-Hill, New York, New York, third edition, 2001.

[3] Michael F. Ashby, Anthony Evans, Norman A. Fleck, Lorna J. Gibson, John W. Hutchinson, and Haydn N. G. Wadley. *Metal Foams*. Butterworth Heinemann, 2000.

[4] G. G. Bach and J. H. S. Lee. Higher-order perturbation solutions for blast waves. *AIAA Journal*, 7:742–744, 1969.

[5] G. G. Bach and J. H. S. Lee. An analytical solution for blast waves. *AIAA Journal*, 8:271–275, 1970.

[6] W. E. Baker, P. A. Cox, P. S. Westine, J. J. Kulesz, and R. A. Strehlow. *Explosion Hazards and Evaluation*. Elsevier Scientific Publishing Company, New York, New York, 1983.

[7] W. E. Baker, P. S. Westine, and F. T. Dodge. *Similarity Methods in Engineering Dynamics: Theory and Practice of Scaled Modeling*. Elsevier Scientific Publishing Company, Amsterdam, The Netherlands, 1991.

[8] Wilfred E. Baker. *Explosions in Air*. University of Texas Press, Austin, Texas, 1973.

[9] Wilfred E. Baker and Ming Jun Tang. *Gas, Dust and Hybrid Explosions*. Elsevier, Amsterdam, The Netherlands, 1991.

[10] M. Y. H. Bangash. *Impact and Explosion*. CRC Press, Boca Raton, Florida, 2000.

[11] G. I. Barenblatt. *Scaling, Self-similarity, and intermediate asymptotics*. Cambridge University Press, Cambridge, United Kingdom, 2002.

[12] G. I. Barenblatt. *Scaling*. Cambridge University Press, Cambridge, United Kingdom, 2003.

[13] James T. Baylot, Billy Bullock, Thomas R. Slawson, and Stanley C. Woodson. Blast response of lightly attached concrete masonry unit walls. *Journal of Structural Engineering*, 131(8):1186–1193, 2005.

[14] H. A. Bethe, editor. *Blast Wave*. Los Alamos Scientific Laboratory, 1967.

[15] H. L. Brode. Numerical solution of spherical blast waves. *Journal of Applied Physics*, 26(6):766–775, 1955.

[16] P. Bulson. *Explosive Loading of Engineering Structures*. E & FN Spon, 1997.

[17] T. J. Cloete, G. N. Nurick, and R. N. Palmer. The deformation and shear failure of peripherally clamped centrally supported blast loaded circular plates. *International Journal of Impact Engineering*, 32:92–117, 2005.

[18] The Visual Site Interactive Analysis Code. The Alfred E. Murrah federal building. http://visac.ornl.gov/HelpFiles/nse2004/okcity3.jpg, 2007. Oak Ridge National Laboratory.

[19] Robert H. Cole. *Underwater Explosions*. Dover Publications, Inc., New York, New York, 1948.

[20] G. J. Cooper. Protection of the lung from blast overpressure by thoracic stress wave decouplers. *Journal of Trauma: Injury, Infection and Clinical Care*, 40(3):105–110, 1996.

[21] G. J. Cooper, B. P. Pearce, A. J. Sedman, I. S. Bush, and C. W. Oakley. Experimental evaluation of a rig to simulate the response of the thorax to blast loading. *Journal of Trauma: Injury, Infection and Clinical Care*, 40(3):38–41, 1996.

[22] G. J. Cooper, D. J. Townend, S. R. Carter, and B. P. Pearce. The role of stress waves in thoracic visceral injury from blast loading: Modification of stress transmission by foams and high-density materials. *Journal of Biomechanics*, 24(5):273–285, 1991.

[23] Paul W. Cooper. *Explosives Engineering*. Wiley-VCH, New York, New York, 1970.

[24] National Research Council. *The Embassy of the Future*. National Academy Press, 1986.

[25] National Research Council. *Protecting Buildings from Bomb Damage*. National Academy Press, 1995.

[26] Alan Cowell. Subway and bus blasts in London kill at least 37. *The New York Times*, July 08:1, 2005.

[27] R. Cox and L. Crabtree. *Elements of Hypersonic Aerodynamics*. English Universities Press, 1965.

[28] William C. Davis. Shock waves; Rarefaction waves; Equations of state. In Jonas A. Zukas and William P. Walters, editors, *Explosive Effects and Applications*, High-Pressure Shock Compression of Condensed Matter, chapter 3, pages 47–113. Springer-Verlag, New York, New York, 1997.

[29] V. S. Deshpande and N. A. Fleck. One-dimensional response of sandwich plates to underwater shock loading. *Journal of Mechanics and Physics of Solids*, 53:2347–2383, 2005.

[30] V. S. Deshpande, A. Heaver, and N. A. Fleck. An underwater shock simulator. *Proceedings of the Royal Society A*, 462:1021–1041, 2006.

[31] John Dewey. Gallery of fluid mechanics. http://www.fluidmech.net/gallery/shocks/ab.htm, 2005. Cambridge University Press.

[32] John M. Dewey. The air velocity in blast waves from tnt explosions. *Proceedings of the Royal Society A*, pages 366–385, 1964.

[33] K. P. Dharmasena, H. N. G. Wadley, and J. W. Hutchinson. Mechanical response of metallic honeycomb sandwich panel structures to high intensity dynamic loading. *to be published*, 2006.

[34] D. S. Drumheller. *Introduction to Wave Propagation in Nonlinear Fluids and Solids*. Cambridge University Press, Cambridge, United Kingdom, 1998.

[35] George Emanuel. *Analytical Fluid Dynamics*. CRC Press, Boca Raton, Florida, 2001.

[36] James A. Fay. *Introduction to Fluid Mechanics*. MIT Press, Cambridge, Massachusetts, 1994.

[37] N. A. Fleck and V. S. Deshpande. The resistance of clamped sandwich beams to shock loading. *Journal of Applied Mechanics*, 71:386–401, May 2004.

[38] N. A. Fleck and V. S. Deshpande. Closure to "Discussion of 'The resistance of clamped sandwich beams to shock loading' " (2005, ASME J. Appl. Mech., 72, pp. 978-979). *Journal of Applied Mechanics*, 72:980, November 2005.

[39] David L. Frost and Fan Zhang. Non-ideal blast waves from heterogenous explosives. *Explosion, Shock Wave and Hypervelocity Phenomena in Materials*, pages 421–426, 2004.

[40] Ronald Glasser. A shock wave of brain injuries. *The Washington Post*, April 08:B01, 2007.

[41] S. Glasstone and P. Dolan. *The Effects of Nuclear Weapons*. DOE & DOD, 1977.

[42] Joseph S. Gondusky and Michael P. Reiter. Protecting military convoys in Iraq: An examination of battle injuries sustained by mechanized battalion during operation Iraqi Freedom II. *Military Medicine*, 170(6):546–549, 2005.

[43] J. Henrych. *The Dynamics of Explosion and Its Use*. Elsevier, Amsterdam, The Netherlands, 1979.

[44] H. Huang. Transient bending of a large elastic plate by an incident spherical pressure wave. *Journal of Applied Mechanics*, pages 772–776, September 1974.

[45] H. Huang and Y. F. Wang. Transient interactions of spherical acoustic waves and cylindrical elastic shells. *Journal of the Acoustical Society of America*, 48:228–235, 1970.

[46] John W. Hutchinson and Zhenyu Xue. Metal sandwich plates optimized for pressure impulses. *International Journal of Mechanical Sciences*, 47:545–569, 2005.

[47] N. Jacob, S. C. K. Yuen, G. N. Nurick, D. Bonorchis, S. A. Desai, and D. Tait. Scaling aspects of quadrangular plates subjected to localized blast loads – experiments and predictions. *International Journal of Impact Engineering*, 30:1179–1208, 2004.

[48] N. Jones. *Structural Impact*. Cambridge University Press, Cambridge, United Kingdom, 1997.

[49] N. Kambouchev, L. Noels, and R. Radovitzky. Nonlinear compressibility effects in fluid-structure interaction and their implications on the air-blast loading of structures. *Journal of Applied Physics*, 2006.

[50] N. Kambouchev, L. Noels, and R. Radovitzky. Fluid-structure interaction effects in the dynamic response of free-standing plates to uniform shock loading. *Journal of Applied Mechanics*, 2007.

[51] N. Kambouchev, L. Noels, and R. Radovitzky. Numerical simulation of the fluid-structure interaction between air blast waves and free-standing plates. *Computers & Structures*, 2007.

[52] M. M. Kamel, A. F. Ghoniem, M. I. Rashed, and A. K. O. K. Oppenheim. Blast waves in real gases. *Acta Astronautica*, 4:439–458, 1977.

[53] V. K. Kedrinskii. *Hydrodynamics of Explosion*. Springer-Verlag, Berlin, Germany, 2005.

[54] G. F. Kinney. *Explosive Shocks in Air*. MacMillan, New York, New York, 1962.

[55] Gergory W. Kooistra, Vikram S. Deshpande, and H. N. G. Wadley. Compressive behavior of age hardenable tetrahedral structures made from aluminum. *Acta Materialia*, 52:4229–4237, 2004.

[56] V. Kuropatenko. On difference methods for the equations of hydrodynamics. In N. N. Janenko, editor, *Difference Methods for Solutions of Problems of Mathematical Physics*, volume 1 of *High-Pressure Shock Compression of Condensed Matter*, pages 287–303. American Mathematical Society, 1967.

[57] C. W. Lampson. The blast and radiation from an atomic bomb. In *Proceedings of the Conference on Building in the Atomic Age*. Department of Civil and Sanitary Engineering, MIT, 1952.

[58] G. S. Langdon and G. K. Schleyer. Scale testing of profiled stainless steel blast walls. In N. Jones and C. A. Brebbia, editors, *Structures under Shock and Impact VIII*, pages 111–120. WIT Press, Southampton, The United Kingdom, 2004.

[59] G. S. Langdon and G. K. Schleyer. Inelastic deformation and failure of profiled stainless steel blast wall panels. Part I: Experimental investigation. *International Journal of Impact Engineering*, 31:341–369, 2005.

[60] G. S. Langdon and G. K. Schleyer. Inelastic deformation and failure of profiled stainless steel blast wall panels. Part II: Analytical modeling considerations. *International Journal of Impact Engineering*, 31:371–399, 2005.

[61] G. S. Langdon and G. K. Schleyer. Inelastic deformation and failure of profiled stainless steel blast wall panels. Part III: Finite element simulations and overall summary. *International Journal of Impact Engineering*, 31:988–1012, 2005.

[62] G. S. Langdon, S. C. K. Yuen, and G. N. Nurick. Experimental and numerical studies of the response of quadrilateral stiffened plates. Part II: Localized blast loading. *International Journal of Impact Engineering*, 31:85–111, 2005.

[63] Cho-Chung Liang and Yuh-Shiou Tai. Shock responses of a surface ship subjected to noncontact underwater explosions. *Ocean Engineering*, 33:748–772, 2006.

[64] Y. Liang, A. V. Spuskanyuk, S. E. Flores, D. R. Hayhurst, J. W. Hutchinson, R. M. McMeeking, and A. G. Evans. The response of metallic sandwich panels to water blast. *Journal of Applied Mechanics*, 74:81–99, January 2007.

[65] L. A. Louca, J. W. Boh, and Y. S. Choo. Response of profiled barriers subject to hydrocarbon explosions. *Proceedings of the Institution of Civil Engineers, Structures & Buildings*, 157(5):319–331, 2004.

[66] B. M. Luccioni, R. D. Ambrosini, and R. F. Danesi. Assessment of blast loads on structures. In M. Alves and H. Jones, editors, *Impact Loading of Lightweight Structures*, pages 347–358. WIT Press, Southampton, The United Kingdom, 2005.

[67] K. Marchand, E. B. Williamson, and D. G. Winget. Analysis of blast loads on bridge substructures. In N. Jones and C. A. Brebbia, editors, *Structures under Shock and Impact VIII*, pages 151–160. WIT Press, Southampton, The United Kingdom, 2004.

[68] Maria A. Mayorga. The pathology of primary blast overpressure injury. *Toxicology*, 121:17–28, 1997.

[69] G. C. Mays. Design of elements in reinforced concrete and structural steel. In G. C. Mays and P. D. Smith, editors, *Blast Effects on Buildings*. Thomas Telford, London, United Kingdom, 1995.

[70] R. M. McMeeking, A. V. Spuskanyuk, M. Y. He, V. S. Deshpande, N. A. Fleck, and A. G. Evans. An analytic model for the response to water blast of unsupported metallic sandwich panels. *To be published*, 2007.

[71] G. J. McShane, D. D. Radford, V. S. Deshpande, and N. A. Fleck. The response of clamped sandwich plates with lattice cores subjected to shock loading. *European Journal of Mechanics*, 25:215–229, 2006.

[72] T. Mukai, H. Kanahashi, T. Miyoshi, M. Mabuchi, T. G. Nieh, and K. Higashi. Experimental study of energy absorption in a close-celled aluminum foam under dynamic loading. *Scripta Materialia*, 40(8):921–927, 1999.

[73] Souichi Murata. New exact solution of the blast wave problem in gas dynamics. *Chaos, Solitons & Fractals*, 28:327–330, 2005.

[74] AirForce News. Khobar Tower. http://www.au.af.mil/au/awc/awcgate/khobar/khobar.htm, 2007. Maxwell-Gunter AFB.

[75] L. Noels, K. Dharmasena, H. Wadley, and R. Radovitzky. Experimental validation of coupled blast-structure interaction simulations. *International Journal of Impact Engineering*, 2007.

[76] G. N. Nurick and J. B. Martin. Deformation of thin plates subjected to impulse loading – a review. Part I: Theoretical considerations. *International Journal of Impact Engineering*, 8(2):159–170, 1989.

[77] G. N. Nurick and J. B. Martin. Deformation of thin plates subjected to impulse loading – a review. Part II: Experimental studies. *International Journal of Impact Engineering*, 8(2):171–186, 1989.

[78] Lockport NY. USS Cole. http://www.lockport-ny.com/Pictures/atlarge2.htm, 2007. Lockport NY.

[79] American Society of Civil Engineers. *Design of Structures to Resist Nuclear Weapons Effects*. American Society of Civil Engineers, 1961.

[80] American Society of Civil Engineers. *Design of Structures to Resist Nuclear Weapons Effects*. American Society of Civil Engineers, New York, 1985.

[81] American Society of Civil Engineers. The Pentagon building performance report, 2003.

[82] A. K. Oppenheim. *Introduction to Gasdynamics of Explosions*. Springer-Verlag, 1970.

[83] K. Oshima. Blast wave produced by exploding wires. In W. G. Chace and H. K. Moore, editors, *Exploding Wires*, volume 2. Plenum Press, New York, New York, 1962.

[84] M. N. Plooser. Shock waves from line sources. numerical solutions and experimental measurements. *Physics of Fluids*, 13:2665–2675, 1970.

[85] J. Proakis and M. Salehi. *Communication Systems Engineering*. Prentice Hall, Upper Saddle River, New Jersey, 2002.

[86] Douglas T. Queheillalt and H. N. G. Wadley. Cellular metal lattices with hollow trusses. *Acta Materialia*, 53:303–313, 2005.

[87] Douglas T. Queheillalt and H. N. G. Wadley. Pyramidal lattice truss structures with hollow trusses. *Material Sciences and Engineering A*, 397:132–137, 2005.

[88] X. Qui, V. S. Deshpande, and N. A. Fleck. Finite element analysis of the dynamic response of clamped sandwich beams subject to shock loading. *European Journal of Mechanics*, 22:801–814, 2003.

[89] X. Qui, V. S. Deshpande, and N. A. Fleck. Dynamic response of a clamped circular sandwich plate subject to shock loading. *Journal of Applied Mechanics*, 71:637–645, September 2004.

[90] X. Qui, V. S. Deshpande, and N. A. Fleck. Impulsive loading of clamped monolithic and sandwich beams over a central patch. *Journal of Mechanics and Physics of Solids*, 53:1015–1046, 2005.

[91] T. Rabczuk, J. Y. Kim, E. Samaniego, and T. Belytschko. Homogenization of sandwich structures. *International Journal for Numerical Methods in Engineering*, 61:1009–1027, 2004.

[92] Timon Rabczuk, Esteban Samaniego, and Ted Belytschko. Simplified model for predicting impulsive loads on submerged structures to account for fluid-structure interaction. *International Journal of Impact Engineering*, 34:163–177, 2007.

[93] D. D. Radford, V. S. Deshpande, and N. A. Fleck. The use of metal foam projectiles to simulate shock loading on a structure. *International Journal of Impact Engineering*, 31:1152–1171, 2005.

[94] D. D. Radford, N. A. Fleck, and V. S. Deshpande. The response of clamped sandwich beams subjected to shock loading. *International Journal of Impact Engineering*, 32:968–987, 2006.

[95] D. D. Radford, G. J. McShane, V. S. Deshpande, and N. A. Fleck. The response of clamped sandwich plates with metallic foam cores to simulated blast loading. *International Journal of Solids and Structures*, 43:2243–2259, 2006.

[96] H. J. Rathbun, D. D. Radford, Z. Xue, M. Y. He, J. Yang, V. Deshpande, N. A. Fleck, J. W. Hutchinson, F. W. Zok, and A. G. Evans. Performance of metallic honeycomb-core sandwich beams under shock loading. *International Journal of Solids and Structures*, 43:1746–1763, 2006.

[97] Alex M. Remennikov and Timothy A. Rose. Modeling blast loads on buildings in complex city geometries. *Computers & Structures*, 83:2197–2205, 2005.

[98] T. A. Rose and P. D. Smith. Influence of the principal geometrical parameters of straight city streets on positive and negative phase blast wave impulses. *International Journal of Impact Engineering*, 27:359–376, 2002.

[99] O. Sadot, I. Anteby, S. Harush, O. Levintant, E. Nizri, B. Ostraich, A. Schenker, E. Gal, Y. Kivity, and G. Ben-Dor. Experimental investigation of dynamic properties of aluminum foams. *Journal of Structural Engineering*, 131(8):1226–1232, 2005.

[100] A. Sakurai. Blast wave theory. In M. Holt, editor, *Basic Developments in Fluid Dynamics*, volume 1. Academic Press, 1965.

[101] H. Salim, R. Dinan, and P. T. Townsend. Analysis and experimental evaluation of in-fill steel-stud wall systems under blast loading. *Journal of Structural Engineering*, 131(8):1212–1225, 2005.

[102] A. Schenker, I. Anteby, E. Nizri, B. Ostraich, Y. Kivity, O. Sadot, O. Hanam, R. Michaelis, E. Gai, and G. Ben-Dor. Foam protected reinforced concrete structures under impact: Experimental and numerical studies. *Journal of Structural Engineering*, 131(8):1233–1242, 2005.

[103] Elaine Sciolino. 10 bombs shatter trains in Madrid, killing 192. *The New York Times*, March 12:1, 2004.

[104] L. I. Sedov. *Similarity and Dimensional Methods in Mechanics*. CRC Press, Boca Raton, Florida, 10th edition, 1993.

[105] L.I. Sedov, editor. *Proceedings of the Steklov Institute of Mathematics*. American Mathematical Society, 1967.

[106] P. Smith and J. Hetherington. *Blast and Ballistic Loading of Structures*. Butterworth Heinemann, 1994.

[107] P. D. Smith. Blast loading. In G. C. Mays and P. D. Smith, editors, *Blast Effects on Buildings*, pages 24–45. Thomas Telford, London, United Kingdom, 1995.

[108] Peter D. Smith and Timothy A. Rose. Blast wave propagation in city streets – an overview. *Progress In Structural Engineering and Materials*, 8(1):16–28, 2006.

[109] S. B. Smith. General reaction of buildings to atomic blast. In *Proceedings of the Conference on Building in the Atomic Age*. Department of Civil and Sanitary Engineering, MIT, 1952.

[110] Richard E. Sonntag, Claus Borgnakke, and Gordon J. Van Wylen. *Fundamentals of Thermodynamics*. John Wiley & Sons, Inc., New York, New York, fifth edition, 1998.

[111] H. Steiner and W. Gletler. The propagation of spherical and cylindrical shock waves in real gases. *Physics of Fluids*, 6:2154–2164, 1994.

[112] H. Steiner, W. Gletler, and T. Hirshler. Numerical solution for spherical laser-driven shock waves. *Shock Waves*, 8:139–147, 1998.

[113] James H. Stuhmiller. Biological response to blast overpressure: A summary of modeling. *Toxicology*, 121:91–103, 1997.

[114] James H. Stuhmiller, Kevin H.-H. Ho, Michael J. Vander Vorst, Kenneth T. Dodd, Thomas Fitzpatrick, and Maria Mayorga. A model of blast overpressure injury to the lung. *Journal of Biomechanics*, 29(2):227–234, 1996.

[115] Katherine H. Taber, Deborah L. Warden, and Robin A. Hurley. Blast related traumatic brain injury: What is known? *Journal of Neuropsychiatry and Clinical Neuro-science*, 18(2):17–28, 2006.

[116] P.J. Tan, S. R. Reid, and J.J. Harrigan. Discussion: "The resistance of clamped sandwich beams to shock loading" (Fleck, N. A., and Deshpande, V. S., 2004,

ASME J. Appl. Mech., 71, pp. 386-401). *Journal of Applied Mechanics*, 72:978–979, November 2005.

[117] G. I. Taylor. The formation of a blast wave by a very intensive explosion. I. Theoretical discussion. *Proceedings of the Royal Society A*, 201(1065):159–174, 1950.

[118] G. I. Taylor. The formation of a blast wave by a very intensive explosion. II. The atomic explosion of 1945. *Proceedings of the Royal Society A*, 201(1065):175–186, 1950.

[119] G. I. Taylor. The pressure and impulse of submarine explosion waves on plates. In G.K. Batchelor, editor, *The scientific papers of Sir Geoffrey Ingram Taylor*, volume III: Aerodynamics and the Mechanics of Projectiles and Explosions, pages 287–303. Cambridge University Press, 1963.

[120] M. D. Theobald and G. N. Nurick. Numerical investigation of the response of sandwich panels subject to blast loads. In M. Alves and N. Jones, editors, *Impact Loading of Lightweight Structures*, pages 521–534. WIT Press, Southampton, The United Kingdom, 2005.

[121] P. Thompson. *Compressible-Fluid Dynamics*. McGraw-Hill, New York, New York, 1972.

[122] M. T. Tilbrook, V. S. Deshpande, and N. A. Fleck. The impulsive response of sandwich beams: analytical and numerical investigation of regimes of behavior. *Journal of Mechanics and Physics of Solids*, 54:2242–2280, 2006.

[123] Defense Update. RG-31 Nyala mine protected vehicle. http://www.defense-update.com/products/r/RG-31.htm, 2007. Defense Update.

[124] A. Vaziri and J. W. Hutchinson. Metal sandwich plates subject to intense air shocks. *International Journal of Solids and Structures*, 44:2021–2035, 2007.

[125] A. Vaziri, Z. Xue, and J. W. Hutchinson. Metal sandwich plates with polymer foam-filled cores. *Journal of Mechanics of Materials and Structures*, 1:97–127, 2006.

[126] John von Neumann. The point source solution. In *Collected Works*, volume 6, pages 219–237. Pergamon, 1943.

[127] John von Neumann and R. Richtmyer. A method for the numerical computation of hydrodynamic shocks. *Journal of Applied Physics*, 21:232–237, 1950.

[128] H. N. G. Wadley, K. P. Dharmasena, M. He, R. McMeeking, A. Evans, N. Kambouchev, and R. Radovitzky. Cellular materials concepts for limiting injuries caused by air blasts. *In Preparation*, 0000.

[129] H. N. G. Wadley, A. G. Evans, and N. A. Fleck. Fabrication and structural performance of periodic cellular metal sandwich structures. *Composite Science and Technology*, 63:2331–2343, 2003.

[130] H. N. G. Wadley, Norman A. Fleck, and Anthony G. Evans. Fabrication and structural performance of periodic cellular metal sandwich structures. *Composites Science and Technology*, 63:2331–2342, 2003.

[131] Jun Wei, Mahesh S. Shetty, and Lokeswarappa R. Dharani. Stress characteristics of a laminated architectural glazing subjected to blast loading. *Computers & Structures*, 84:699–707, 2006.

[132] Z. Wei, K. P. Dharmasena, H. N. G. Wadley, and A. G. Evans. Analysis and interpretation of a test for characterizing the response of sandwich panels to water blast. *International Journal of Impact Engineering*, 2007.

[133] G. B. Whitham. *Linear and Nonlinear Waves*. John Wiley & Sons, Inc., New York, New York, 1999.

[134] David G. Winget, Kirk A. Marchand, and Eric B. Williamson. Analysis and design of critical bridges subjected to blast loads. *Journal of Structural Engineering*, 131(8):1243–1255, 2005.

[135] Zhenyu Xue and John W. Hutchinson. Preliminary assessment of sandwich plates subject to blast loads. *International Journal of Mechanical Sciences*, 45:687–705, 2003.

[136] Zhenyu Xue and John W. Hutchinson. A comparative study of impulse-resistant metal sandwich plates. *International Journal of Impact Engineering*, 30:1283–1305, 2004.

[137] S. C. K. Yuen and G. N. Nurick. Experimental and numerical studies of the response of quadrilateral stiffened plates. Part I: Subjected to uniform blast load. *International Journal of Impact Engineering*, 31:55–83, 2005.